MASTER OF SCIENCE THESIS

Flow Separation Control over a Wing-Flap Model

Analysis of flap leading edge applications

J. El Haddar

August 2012

aerodynamics

TUDelft

Flow Separation Control over a Wing-Flap Model
Analysis of flap leading edge applications

MASTER OF SCIENCE THESIS

For obtaining the degree of Master of Science in Aerospace Engineering at
Delft University of Technology

J. El Haddar

August 2012

Faculty of Aerospace Engineering · Delft University of Technology

Delft University of Technology

Delft University Of Technology
Department Of
Aerodynamics

The undersigned hereby certify that they have read and recommend to the Faculty of Aerospace Engineering for acceptance a thesis entitled **"Flow Separation Control over a Wing-Flap Model"** by **J. El Haddar** in partial fulfillment of the requirements for the degree of **Master of Science**.

Dated: August 2012

Board of Examiners:

_____
Prof. dr. F. Scarano

_____
dr. ir. L.L.M. Veldhuis

_____
dr. ir. R. Vos

_____
dr. M. Kotsonis

Abstract

Nowadays, the development of multi-element airfoils show a progression towards a "circular arc" to attain a maximum lift force. The improvement of the high lift performance of specifically a wing-flap combination is an ongoing research at Delft University of Technology. Generally, a higher lift force can be created by deflecting the flap to higher angles. The higher this angle, the larger the curvature the flow has to follow. Consequently the flap becomes dominated by separated flow and a big part of the lift force will be lost. To overcome this lift loss due to flow separation additional flow control techniques become essential. Hence, within the scope of lift improvement, the effect of flap leading edge applications is investigated for a wing-flap model at critical flight conditions i.e. high flap deflection angle of 45° and $Re = 1.7 \cdot 10^6$ ($42m/s$).

The experimental part of this research consist of windtunnel testing in the Low-Speed Low-Turbulunce Windtunnel . Oil flow visualization showed that for the selected configuration the model deals with largely separated flow on the flap. The separation does not occur two-dimensional, but three-dimensional in the form of stall cells. These are independent stationary separated flow regions, in which the flow organizes around multiple counter rotating loci. In order to delay separation the effects of three different types of passive tripping are investigated: zigzag tape, carborundum grains and V-shaped turbulator. Results show that these applications deteriorate the total lift performance with approximately 30%. The total drag is even more than doubled. To take account for the effectiveness of active plasma actuation due to limitations of the driving generator and at the same time to ensure the two-dimensionality of the flow, the effect of the length of an applied roughness is analyzed. It is shown that for correct two-dimensional testing an actuator should span at least 80% of the total flap span. Several plasma actuator configurations are analyzed for both the AC DBD plasma actuator as the NS DBD plasma actuator. However, no significant effects could be achieved on flow separation control over the flap. It is hypothesized that the induced momentum or vortices, by the AC DBD and NS DBD plasma actuator respectively, is just of insufficient magnitude to overcome the strong three-dimensional separated flow.

With the limited effects of actuation, more insight is needed for the maximum possible lift for ideal flow control. This is done in the commercial CFD-software for multi-element airfoils, MSES. Maximum attainable lift is obtained with inviscid calculations. Compared with viscous calculations this gives the lift-loss-progress as function of the flap deflection angle. At low angles of attack, appropriate flow control applications become especially interesting at flap angles higher than 20°. Additionally, experiments for pressure distribution adaption for attached flow is carried out. It is shown that even though flow separation from the flap could be prevented, the airfoil now suffers from wake bursting. This phenomenon limits to a great extent the maximum possible lift performance.

I would like to thank my mother and my father for all the love and support

Contents

Contents

List of Figures

List of Tables

List of Symbols

Latin Symbols

A	Area	$[m^{-2}]$
C_d	Drag coefficient	[-]
C_f	Friction coefficient	[-]
C_l	Lift coefficient	[-]
C_m	Momentum coefficient	[-]
c_p	Heat capacity at constant pressure	$[Jg^{-1}K^{-1}]$
C_p	Pressure coefficient	[-]
D	Duty cycle	[%]
D	Drag force	$[N]$
f	Frequency	$[Hz]$
F^+	Reduced frequency	$[Hz]$
g	Horizontal gap width	$[mm]$
h_o	Total enthalpy	$[J]$
H	Shape factor	[-]
I	Current	$[A]$
l	Actuator electrode length, length	$[mm]$
L	Lift force	$[N]$
m	Mass	$[kg]$
M	Mach number	[-]
$\hat{n}$	Unit normal	[-]
p	Pressure	$[Pa]$
Pr	Prandtl number	[-]
q	Dynamic pressure	$[Pa]$

Q	Heat transfer	$[J]$
Re	Reynolds number	$[\text{-}]$
t	Thickness	$[mm]$
T	Temperature	$[K]$
u	X-component of the velocity	$[ms^{-1}]$
U	Free stream velocity	$[ms^{-1}]$
v	Y-component of the velocity	$[ms^{-1}]$
V	Voltage	$[V]$
w	Electrode width	$[mm]$
x	Streamwise length	$[mm]$

Greek Symbols

α	Geometric angle of attack	$[°]$
γ	Ratio of specific heats	$[\text{-}]$
δ_f	Flap deflection angle	$[°]$
Δ	Difference	$[\text{-}]$
θ	Momentum loss thickness	$[mm]$
μ	Dynamic viscosity	$[kgm^{-1}s^{-1}]$
ξ	Length coordinate	$[m]$
ρ	Density	$[kgm^{-3}]$
τ	Pulse duration	$[s]$

Subscripts

ac	AC voltage amplitude
b	Burst
d	Dielectric
l	Lower electrode
max	Maximum
n	Normal
o	Overall
p	Pulsed operation
pp	Peak to peak
sp	Separated region
tr	Transition
u	Upper electrode
∞	Freestream

Abbreviations

AC	Alternating Current
CFD	Computational Fluid Dynamics
CoR	Co-Rotating
CtR	Counter-Rotating
DBD	Dielectric-Barrier Discharge
HV	High Voltage
LE	Leading Edge
LER	Leading Edge Roughness
LTT	Low Turbulence Tunnel
MMM	Multi Mano Meter
NLF	Natural Laminar Flow
NS	Nano Second
PIV	Particle Image Velocimetry
TE	Trailing Edge
VG	Vortex Generator

Chapter 1

Introduction

1.1 Introduction

A greener future is the leading concept to ensure safe and healthy living for future generations of human kind. Technology is continuously progressing to achieve this goal, to live "smart" and to minimize the impact humans have on the global environment. Also in the field of aviation efforts are taken to investigate how aircraft can fly more efficiently. Within this scope, the grateful task has been assigned to engineers to seek for optimal high lift systems for our future aircraft.

The way to control the flow, as stated also by Gad-El-Hak, can be divided into Passive and Active flow control [13]. A Passive flow control device requires no auxiliary power and no control loop. In the past this resulted in the development of high lift systems which improves the lift performance by using slotted flaps. This enables an aircraft to fly steeper during take-off and landing which directly reduces the area encountering air-traffic noise and furthermore reducing the time spend during this fuel consuming flight condition. Also during other critical flight conditions e.g. maximum and sustained turn rate the benefits of such high lift systems are directly apparent.

However, to fly even more efficiently there is the need to create more effective high lift systems. The progression of multi-element airfoils nowadays have shown to develop towards a circular arc when the flaps and slats are maximum deflected [33]. More lift can be created this way, resolving part of the problem but still a big part of the potential lift goes lost as the air flow can hardy follow the strong curvature dictated by the slat and flap deflections; eventually the flow will separate at some point from the surface.

With the high lift systems pushed to their limits, the control methods to deal with flow separation are being explored even more. A growing interest in the past decade is in the field of Active flow control. This type of devices require a certain amount of energy and a control loop. The most promising active flow control device is the Dielectric-Barrier Discharge (DBD) plasma actuator. This actuator has become popular due to its following properties: low energy consumption, low weight, no moving parts, fast response, inexpensiveness and low parasite drag. The DBD plasma actuator acquires flow control by the injection of momentum in the near-wall region. The extent to which a free airflow can be manipulated is determined by examining three main fields of flow control [24]:

- Flow separation

- Laminar to turbulent flow transition

- Turbulence

The DBD plasma actuator has been successfully applied in these fields of flow control applications, such as: exciting boundary layer instabilities on a sharp cone at Mach 3.5, lift augmentation on an airfoil section, low-pressure turbine blade separation control, unsteady vortex generation, and airfoil leading-edge separation control [26]. However, the limited momentum injection of the conventional plasma actuator limited its use. Recently an alternative manner of plasma discharge is proposed: the nanosecond-pulse driven plasma actuator. Flow control authority by this discharge mechanism lies in the impact of the energy transfer to the near-surface gas and the fast heating of the layer [34]. This property makes the nanosecond-pulsed plasma actuator more effective at higher velocities with respect to the conventional actuator.

So in order to achieve our goal a high lift system needs additional flow control devices to get a step closer towards the potential lift limits. An analysis of control applications is necessary to map the opportunities and to see what is feasible within the resources available. This all could lead to a better understanding and a step towards our "smarter" future.

1.2 Research objectives

In this work, the aim is to analyze the potential of a high lift system to enhance its lift performance. The focus will be on separation control from the flap of a two element airfoil, thus a relatively large flap deflection angle will be selected for improvement. An experimental study of flap leading edge applications will be carried out, investigating passive and active applications. For the active applications both the conventional as the nanosecond-pulse driven plasma actuator will be implemented. Up to now, these actuators were mainly exposed to fundamental researches otherwise flow control on relatively small and basic models. With this work, the in literature widely appointed as very promising plasma actuator is brought a step closer towards real life cases by subjection to more critical flight conditions. Additionally, the selected high lift system will be further analyzed using CFD-software allowing more elaborated configuration settings. Before this, the software is validated by comparison with experimental data for a single element airfoil. The final goal is to present an analysis of to which extent a high lift system can be modified such that optimal flow control authority is obtained over its deflectable flap.

So this research work will contain the following objectives:

1. Identification of characteristics of the chosen high lift model

2. Analysis of passive flap leading edge applications

3. Analysis of active flap leading edge applications

4. Validation of simulation software

5. Maximum lift prediction of the model for ideal flow control

Chapter 2

High lift systems

2.1 Introduction

High lift systems play an important role in the performance of modern aircraft. Each type of aircraft is designed and optimized for its own flight regime e.g. a high-speed military aircraft requires a different wing design with respect to the ones designed for low-speed commercial aircraft. However, the basic aerodynamic principles for generating lift remain the same. In this chapter, aspects related to hight lift systems are discussed together with flow separation related topics.

2.2 Lift enhancement devices

The typical lift-coefficient variation with angle of attack for a single element airfoil is shown in Figure 2.1. The value of C_l varies linearly with α for low-to-moderate angles of attack. This part is characterized by a smooth and mostly attached flow over the airfoil. As α is increased, the flow tends to separate from the top surface of the airfoil, creating large wakes downstream. Consequently, when reaching a certain angle this leads to an abrupt decrease in lift and a large increase in drag, referred to as the *stalled* condition of the airfoil. Just prior to stall the maximum value of C_l, i.e. $C_{l,max}$, is reached which is one of the most important aspects of airfoil's performance. Related to $C_{l,max}$ is the stalling speed: the higher $C_{l,max}$ the lower the stalling speed. Nowadays, a great deal of modern airfoil research is focused towards the improvement of $C_{l,max}$ [2].

To improve the lift performance of an airfoil, flaps are generally applied lift enhancement devices in the aerospace industry. These category of devices are mounted on the trailing edge of an airfoil. In the past, many different flap configurations have been developed such as plain flap, slotted flap and fowler flap although they all serve for the same purpose. Figure 2.2 illustrates some main types of trailing edge flaps with their approximations of $C_{l,max}$-increase and stall angle.

Continuing, the idea behind the use of a flap is to increase the camber and/or surface area of an airfoil with the aim of improving the lift characteristics, see Figure 2.3. Deflection of a flap results in an increased lift and drag force at a given angle of attack and increases $C_{l,max}$ w.r.t. a clean airfoil (no flap deflection). Translated into the lift curve, a downwards deflection of the flap causes the curve to shift upwards and to the left of the lift values. Generally, wings with deflected flaps
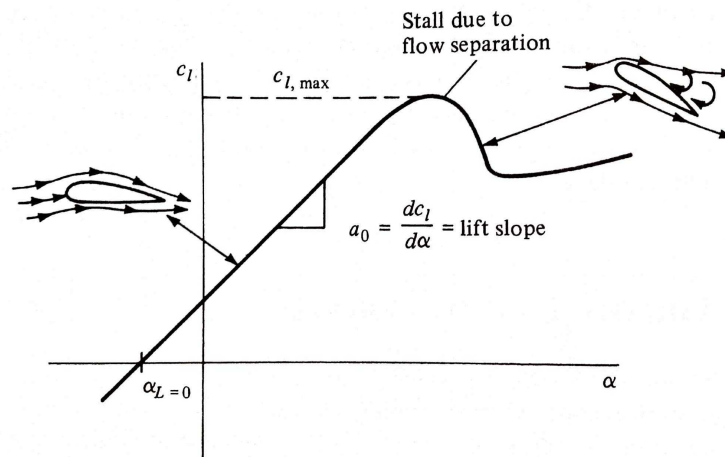
Figure 2.1: Schematic of lift coefficient variation with angle of attack for an airfoil [2].
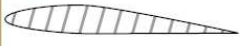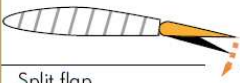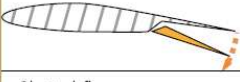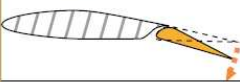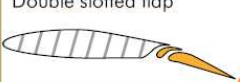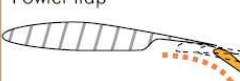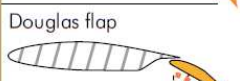
High-lift devices	Incr. of $C_{L\ max}$	a stall
Basic airfoil	-	15°
Plain or camber flap	50%	12°
Split flap	30-40%	14°
Slotted flap	65%	16°
Double slotted flap	70	18°
Fowler flap	90%	15°
Double-slotted Fowler flap	100%	20°
Douglas flap	-	-
Blown flap	80%	16°

Figure 2.2: Types of trailing edge flaps [1].
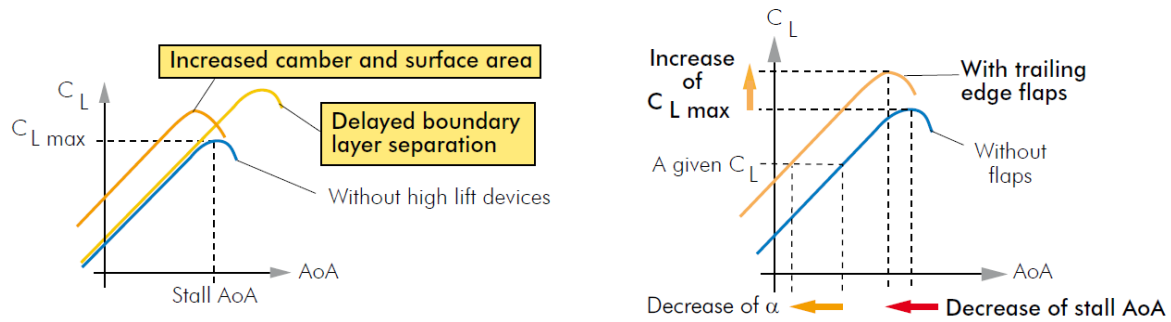
Figure 2.3: Effects of high lift devices (l) and trailing edge flaps (r) on C_l/α [1].

stall at a lower angle of attack than wings without any flaps. This is due to the fact that the pressure gradients at $C_{l,max}$ for both cases are roughly equal (Figure 2.4). It should be noted that flaps increase the downwash and the circulation relative to the airfoil. It also moves the center of pressure (CP) rearwards creating a nose-down moment [1].
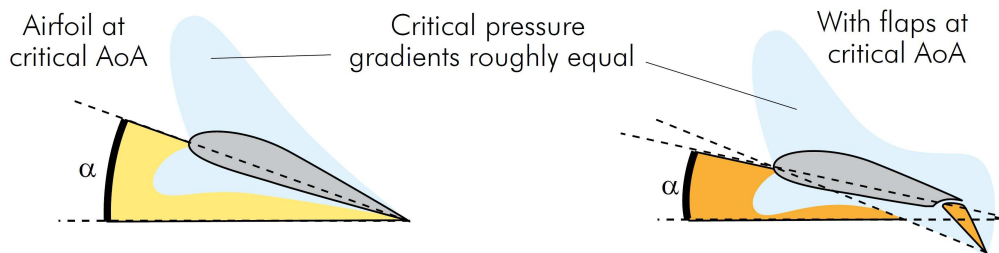
Figure 2.4: Trailing edge flaps at α_{stall} [1].

2.3 The effects of gaps in multi-element airfoils

The consequence of splitting up an airfoil in multiple elements is the formation of gaps, or more convenient "properly designed aerodynamic slots". In the past there was a great deal of ignorance and confusion with respect to the function of these slots. It was suggested that a slot supplies a blowing type of boundary-layer control by permitting the passage of high-energy air from the lower surface and re-energize the boundary layer on the upper surface. This however was not true, because the flow outside of the boundary layers and wakes has the same total pressure everywhere. A. M. O. Smith [33] stated that slots introduce other important phenomena. These can be categorized in five primary effects:

- *Slat effect*: The circulation on a forward element (e.g. a slat) induces velocities on the downstream element which reduce negative pressure peaks (high velocities) on its nose.

- *Circulation effect*: In turn, the circulation on the downstream element induces velocities on the upstream element which increases its circulation. The effect is similar to deflecting a small plain flap; higher velocities on the upper surface - in particular near the trailing edge - and lower velocities on the lower surface.

- *Dumping effect*: The increased velocity at the trailing edge of the forward element relieves the upper surface pressure recovery impressed on the boundary layer, alleviating separation problems and permitting increased lift.

- *Off the surface pressure recovery*: The boundary layer from forward element is dumped at velocities appreciable higher than free stream, and becomes a wake (a viscous phenomena). The final deceleration to free stream velocity is done in an efficient way; without this effect the boundary layer would be unable to overcome the entire pressure rise. The deceleration of the wakes occur out of contact with the wall; this is usually more effective than the best possible deceleration in contact with the wall.

- *Fresh-boundary-layer effect*: Each new element starts out with a fresh boundary layer at its leading edge. Thin boundary layers can withstand stronger adverse pressure gradients than thick boundary layers. Hence, breaking up a boundary layer into several thinner boundary layers is favorable to the delay of separation.

So slots do not act like a source of high-energy air as in blowing boundary layer control. Instead, the main effects at multi-element airfoils are that the upstream element reduces peak velocities on the nose of the downstream element and inversely the downstream element increases the lift and velocities at the trailing edge of the upstream element. These observations of A.M.O. Smith supported the statement that an airfoil consisting of multiple elements is better than a single element airfoil.

2.4   Potential lift limits

With the perspective of lift improvement of a specific airfoil, it useful to know what the theoretical lift limits are. This knowledge gives us insight on where we are now and what may be attainable without compromise the maximum possible lift. Let us consider inviscid, circulatory flow about a circle, where separation will not occur and looking at the limits of C_l [33]. Two possible scenarios of circulation are shown in Figure 2.5; the most interesting is the scenario in Figure 2.5b where the circulation is so strong that the front and rear stagnation points coincide. For the reference chord taken as the diameter of the circle, scenario b represents a lift coefficient of

$$C_l = 4\pi \tag{2.1}$$

which is the maximum attainable lift for the ideal flow case. The next step is to consider three circular-arc mean lines A, B and C (Figure 2.6), because they are easily obtained from Joukowski's transformation for flow about a circle. The limiting case of these mean lines is a straight line. Regardless the degree of camber, the lift prediction of the circular-arc mean lines according to Joukowski's airfoil theory is defined by,

$$L = \pi \rho V_\infty^2 c \left[sin(\alpha + \beta) \right] / cos\beta \tag{2.2}$$

with c the length between the arc ends, α the angle of attack and β a measure for the camber. Figure 2.6 shows that as $\beta \to 90°$, $c \to 0$. Clearly, the definition of c is not the longest dimension if $\beta > 45°$. However, having the lift coefficient defined by the longest dimension one gets two definitions; one valid for $0° \leq \beta \leq 45°$

$$C_l = 2\pi \left[sin(\alpha + \beta) \right] / cos\beta \tag{2.3}$$

and one for $45° \leq \beta \leq 90°$

$$C_l = 4\pi sin\beta sin(\alpha + \beta) \tag{2.4}$$

To prove that 4π is indeed the maximum possible lift, we will discuss some cases shortly:

- if $\beta = 0°$, which indicates a flat-plate airfoil, the maximum lift coefficient according to Equation 2.3 is 2π at $\alpha = 90°$.

- if $\beta = 45°$, whose mean line is a half circle, C_{lmax} according to Equation 2.3 and 2.4 is $4\pi/2^{1/2}$ at $\alpha = 45°$.

- if $\beta = 90°$, what corresponds to a circle, C_{lmax} according to Equation 2.4 is 4π at $\alpha = 0°$.

Hence, the limiting mean line of any airfoil is a complete circle with $C_{lmax} = 4\pi$. Of course this is a very extreme mean line which just states the theoretical limit. A half circle however is not that extreme. In fact, modern multielement flap systems at full flap deflection approach the half circle mean line, see example in Figure 2.7. With $C_{lmax} = 4\pi/2^{1/2} \approx 8.8$ this is still at the high end, but perhaps it will ever be approached with appropriate flow control techniques.
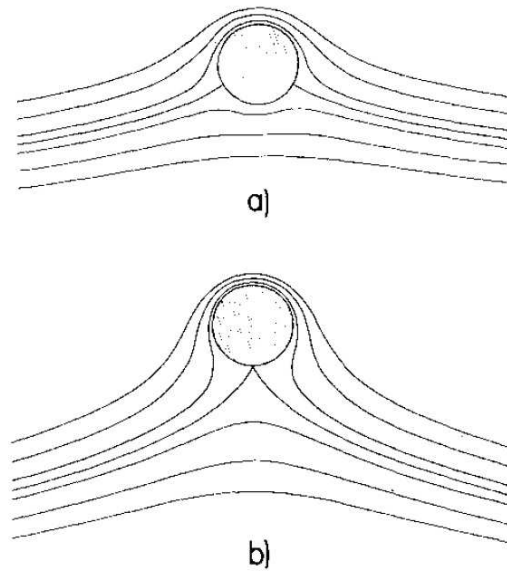
Figure 2.5: Flow about a circle for a) moderate circulation, and b) circulation so strong that the two stagnation points coincide [33].

2.5 The problem of flow separation

The phenomenon of flow separation is generally accepted to be the breakaway or detachment of fluid from a solid surface [14]. In the case of flow separation in high lift configurations, caused by
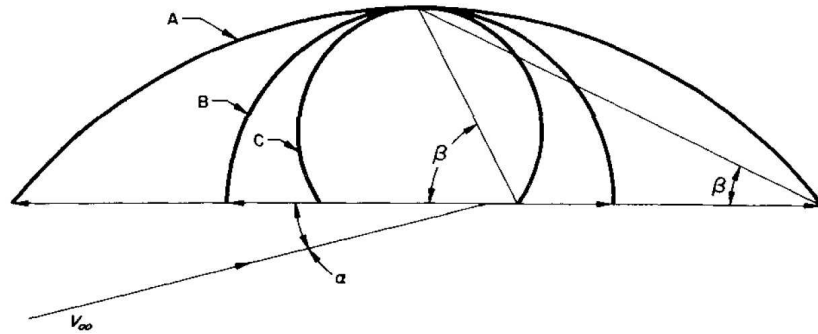
Figure 2.6: Three circular-arc mean lines A, B and C [33].
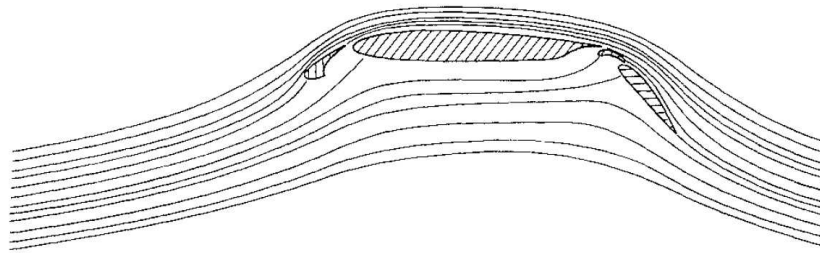
Figure 2.7: Streamline flow field for an airfoil with leading edge slat and double slotted flap [33].

a severe adverse pressure gradient or by any other means, this is accompanied with a significant thickening of the rotational flow region adjacent to the surface. The velocity component normal to the surface is by this significantly increased, disturbing the ideal flow case and losses of some kind can be observed: loss of lift, drag increase, etc. Engineers have tried for decades to alter the separation location or even avoiding it entirely. Before we discuss the classification of methods to tackle this problem, let us focus on how the problem of flow separation arises.

The flow of a fluid over a solid surface causes friction between the two due to the viscosity of the fluid. This frictional force results in a shear stress along the surface and tends to decelerate the flow near the surface. Right at the body surface the velocity is at rest ($V = 0$), called the no-slip condition. The region in which the flow velocity is lower than the free stream velocity is known as the boundary layer. The thickness of this layer is defined by the length from the solid surface to the point where the flow velocity has become (almost) equal to the free stream velocity; this is called the boundary layer thickness. The velocity profile within the boundary layer is a function of the distance from the surface, which will be explained hereafter.

Besides friction, the flow over a solid surface is also determined by the pressure field. When the pressure distribution over the surface increases in flow direction (better known as adverse pressure gradient), it becomes harder for a fluid element to follow the surface and flow against an increasing pressure. Figure 2.8 illustrates how the pressure gradient changes the boundary layer velocity profile. At station s_1 of the surface a fluid element starts with enough energy to follow the surface. The derivative of the fluid velocity perpendicular to the surface $\frac{\partial V}{\partial n}$ is > 0 at this point. As the fluid element continues to move downstream to station s_2, the friction and the adverse pressure gradient have slowed down the element that much that it can not follow its motion anymore. At this point $\frac{\partial V}{\partial n} = 0$ at the surface which is also the starting point of flow separation from the surface. Beyond this point, at station s_3, the fluid element is now pushed back by the adverse pressure gradient causing reversed flow ($\frac{\partial V}{\partial n} < 0$). This reversed flow stimulates the separated flow from the surface,

and a wake of recirculation will occur.
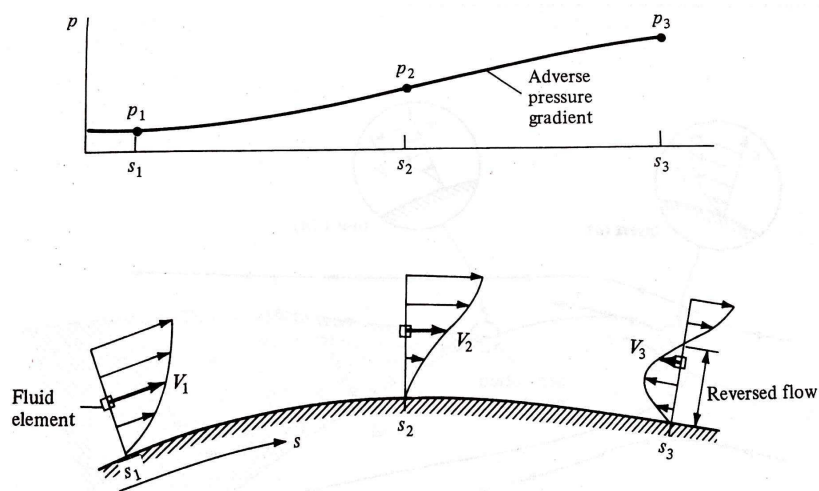
Figure 2.8: As the pressure increases over the surface flow separation occurs between the points s_2 and s_3 [2].

Translated to the case of an airfoil the pressure distribution develops in much the same manner. Due to the adverse pressure gradient on the upper surface and dependent on the exact configuration, separation of the flow can occur which leads to reversed flow in the wake.

The position of separation in the aerodynamic field and the interactions with other flow phenomena is clearly illustrated by considering the schematic in Figure 2.9, by Gad-El-Hak [13]. Starting e.g. with the scenario of a turbulent boundary layer, this layer is more resistant to separation which means that the angle of attack could be increased to enhance the lift performance. Unfortunately a turbulent boundary layer increases the skin friction drag significantly compared to a laminar one. By delaying the transition point the skin friction could be lowered as the laminar boundary layer is maintained over a larger area. The laminar boundary layer however can only withstand a very small adverse pressure gradient without separation, as mentioned before. Once the laminar boundary layer separates, a free-shear layer forms which for moderate Reynolds numbers results in transition to turbulence. A possible reattachment of the separated flow results in the formation of a laminar separation bubble (Figure 2.10), which for higher incidence increases the drag and reducing the lift performance.

The problem of separation and the potential conflicts to achieve a particular control goal are well discussed with these examples. Therefore, the task of nowadays engineer is to make a trade-off between several effects of actuation to finally improve the airfoil's performance in terms of lift-to-drag ratio.

2.6   Separation control

In response to the phenomenon of flow separation, engineers have developed several separation control techniques in the past decades. A general division into Passive or Active Control indicates how the technique deals with this phenomenon. The difference between the two categories is that the Passive Flow Control works continuously on the flow without the need of any additional energy; whether it is required or not the technique is always manipulating the flow field and can not be "turned off". Active Flow Control techniques however are capable of activation or deactivation of
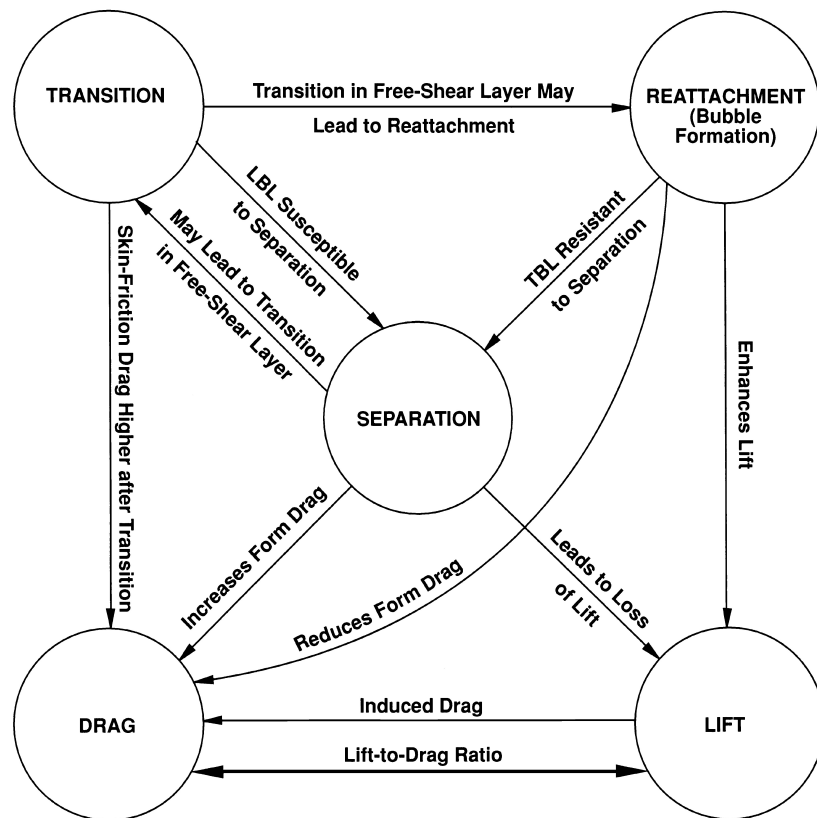
Figure 2.9: Relations between flow-control goals [13].
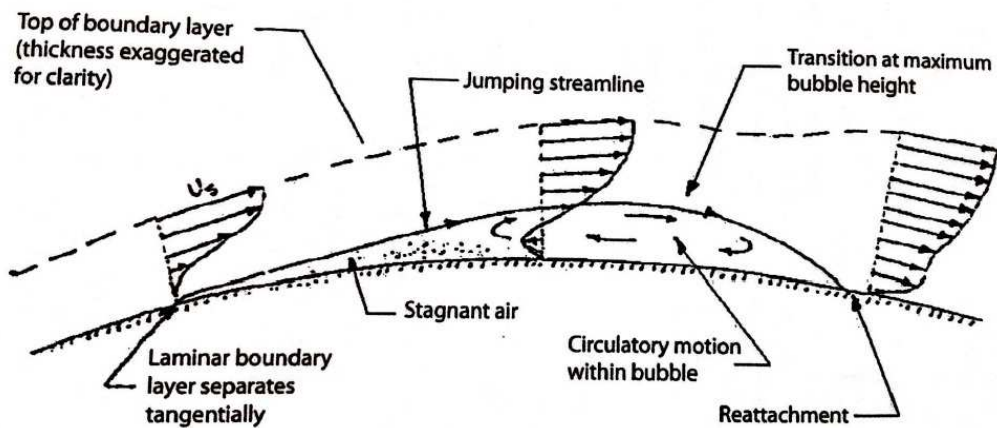
Figure 2.10: Sketch of a laminar separation bubble [25].

the control mechanism by an user, or by any feedback loop control, and essentially requires the addition of energy.

At the end all the techniques are based on the same principles to control the flow. If a fluid particle near the wall has insufficient momentum for continuing its motion the particle is brought to rest at its separation point. Thus the main concept for controlling is to keep the velocity along a surface "as full as possible". In mathematical language the second y-derivative of the velocity at wall position ($\frac{\partial^2 u}{\partial y^2}\big|_{y=0}$) should be kept as negative as possible. In conclusion, in order to prevent

or delay separation by means of some kind of boundary layer control, high momentum air must me guided towards the wall to re-energize and hence increasing the total energy in the near wall boundary layer.

The way how the velocity profile at the wall can be affected is clearly visible by considering one of the physical laws i.e. the streamwise component of the momentum equation at $y = 0$. In a steady case the expression reads:

$$\rho v_w \frac{\partial u}{\partial y}\bigg|_{y=0} + \frac{\partial p}{\partial x}\bigg|_{y=0} - \frac{\partial \mu}{\partial y}\bigg|_{y=0} \frac{\partial u}{\partial y}\bigg|_{y=0} = \mu \frac{\partial^2 \mu}{\partial y^2}\bigg|_{y=0} \tag{2.5}$$

which is valid for both laminar and turbulent flows. The equation shows that three source terms can affect the velocity profile: at the left side the first term is the suction/injection term (negative/positive v_w), secondly is the pressure related term and the last term refers to the thermal influence. Control techniques based on one of these parameters are summarized in Table 2.1. Besides the steady manner, control can also be achieved in an unsteady manner. Basically this is the same as for the steady case, with the addition of an extra time-related (unsteady) term to the momentum equation 2.5. Consequently, the techniques are adapted and now contain an extra operating frequency e.g. pulsed suction/blowing instead of steady.

Passive Control	Active Control
Vortex Generators	Suction/Blowing
Zigzag tape	Zero Mass Flux Blowing
Wall Shaping	Wall Heating/Cooling

Table 2.1: Categorization of some common separation control techniques.

Nowadays, Active Flow Control is one of the leading areas of research in fluid mechanics. In this field of flow control the Dielectric-Barrier Discharge (DBD) plasma actuator shows a promising perspective. This flow control device shows advantages over traditional devices due to: its reduced size, weight and geometric-complexity, the absence of moving parts, inexpensiveness, a low parasite drag, a very fast response time, and a low energy consumption. More on the physics and design of the DBD plasma actuator is discussed in Chapter 3.

2.7   Benefit of excitation

The benefit of excitation is discussed in this section by showing the experimental results of Petz and Nitsche [27]. Their work was focused on flow separation control by periodic excitation on the flap of a generic high-lift configuration. This is in line with part of this thesis research to investigate separation control on the flap by means of DBD plasma actuators. Hence the results from Petz and Nitsche are representative for the potential of plasma actuators, in terms of lift improvement of a wing-flap model.

For the experiments of Petz and Nitsche an actuator system was fitted inside the flap. To excite the surrounding flow a pulsed wall jet (pulsed blowing) emanates from the upper surface near the flap's leading edge through a small spanwise-oriented slot. The optimum choice for unsteady actuation is generally at or slightly upstream of the separation point. This ensures that the shear layer is excited by the control perturbations near its receptivity point. A successful introduction of such forcing creates large spanwise vortices that develop via the Kelvin-Helmholtz instability. Momentum

transport between the freestream and separated region is encouraged by these vortices and causes the flow to reattach [22].

The effect of periodic forcing on reattaching the separated flow can be seen in Figure 2.11. Two particle image velocimetry (PIV)-images are shown of the flowfield with and without excitation. In the case of *base flow*, a large separated region can be noticed on top of the flap. High vorticity appears within the separated shear layer of the leading edge and the separated flow from the trailing edge of the flap. When introducing the periodic blowing, mixing between the separated region and the shear layer is enhanced resulting in an attached flow; see *excited flow* in Figure 2.11. The vortices produced by the excitation now follow the curvature of the flap and are of smaller magnitude with respect to the separated case.
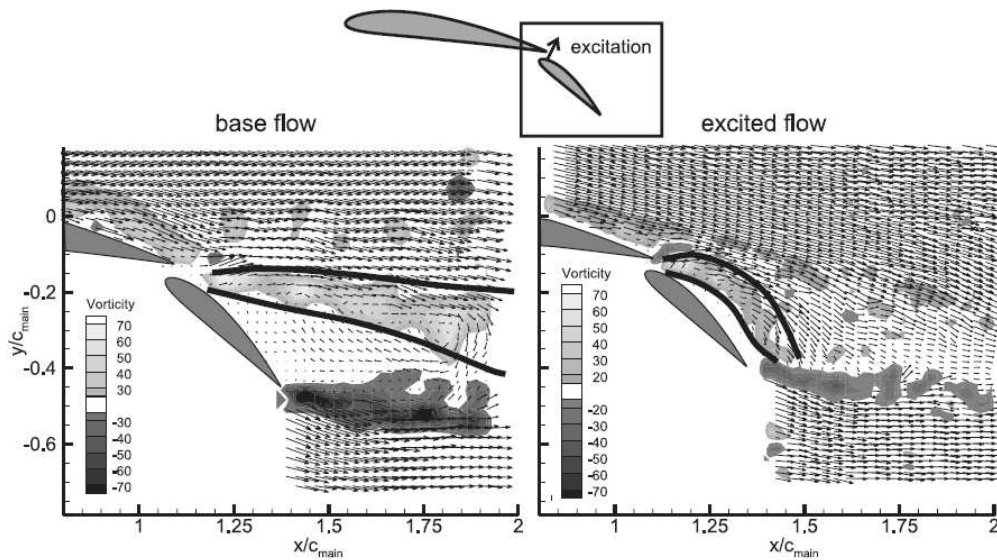
Figure 2.11: Flow visualization from PIV data for an unexcited (l) and excited (r) flow [27].

Concerning the non-dimensional excitation frequency (reduced frequency or Strouhal number), a commonly used definition can be found in literature. This definition takes the following form:

$$F^+ = \frac{f x_{sp}}{U_\infty} \qquad (2.6)$$

where f is the forcing frequency, x_{sp} is the length of the separated region and U_∞ is the freestream velocity. For separation control, the value of the periodic excitation is generally known to be on the order of unity. However, one should be careful when comparing this parameter from different literature. Even if the definition of x_{sp} is fixed, the origin from which this value is being measured may differ for different researches.

There are many other parameters which affect the benefit of unsteady excitation. Hence, the results shown in the following figures are collected by setting some parameters fixed in advance, such as flap gap, flap overlap, excitation location and excitation direction. The Reynolds number is set at $0.55 \cdot 10^6$. The effect of separation delay due to excitation while sweeping the flap deflection δ_f is displayed in Figure 2.12. The angle of attack α is kept constant at $7°$. Here the base flow shows an increase in lift until the flow separates from the flap at $\delta_f = 30°$. In comparison to this, excited flow shows an improvement in maximum deflection angle by $9°$, reaching $\delta_f = 39°$. In terms of drag, a large separation region is avoided which lowers the C_d value (see right-hand side Figure 2.12).
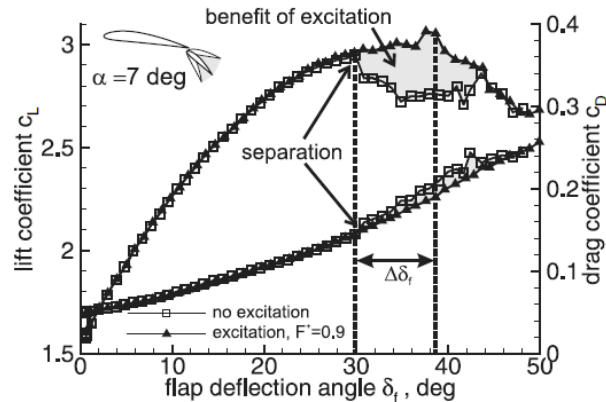
Figure 2.12: Effect of separation delay on C_l and C_d due to excitation [27].

This leads to two fundamental conclusions:

1. Periodic excitation can prevent separation at large deflection angles.

2. Periodic excitation does not cause additional drag as long as the flow is attached in the first case.

To mimic the landing or takeoff configuration of a wing, the flap deflection is now kept constant (at $\delta_f = 32°$) and the angle of attack is set as a varying parameter. The lift and drag development for this case, for the excited and unexcited flow, is displayed in Figure 2.13. While for the unexcited case flow separation occurs at the flap at $\alpha = 2°$ followed by flow separation from the main wing later on at $\alpha = 7°$, the excited case shows in this region a significant improvement and keeps the flow fully attached to the flap. This results in a lift increase by up to 12% while at the same time drag decreases by up to 12%.
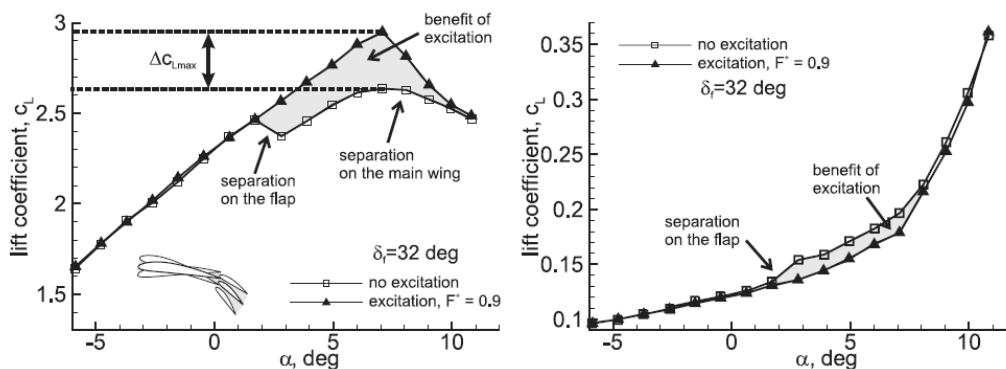
Figure 2.13: Lift and drag versus angle of attack with and without excitation [27].

As regards to the aerodynamic quantity, the lift-to-drag ratio, the benefit of periodic excitation is displayed even better. The already mentioned flap deflection of $\delta_f = 32°$, which is near the onset of separation, shows a gain by up to 20-25% over a wide range of angles of attack (see Figure 2.14(l)). Deflecting the flap to a higher angle i.e. $\delta_f = 38°$, means that the flow is fully detached from the flap even at small angles of attack. Despite this fact, periodic excitation shows suppression of flow separation. The lift-to-drag ratio in this case increases by 10-12% for a greater range of angle of attack (see Figure 2.14(r)).
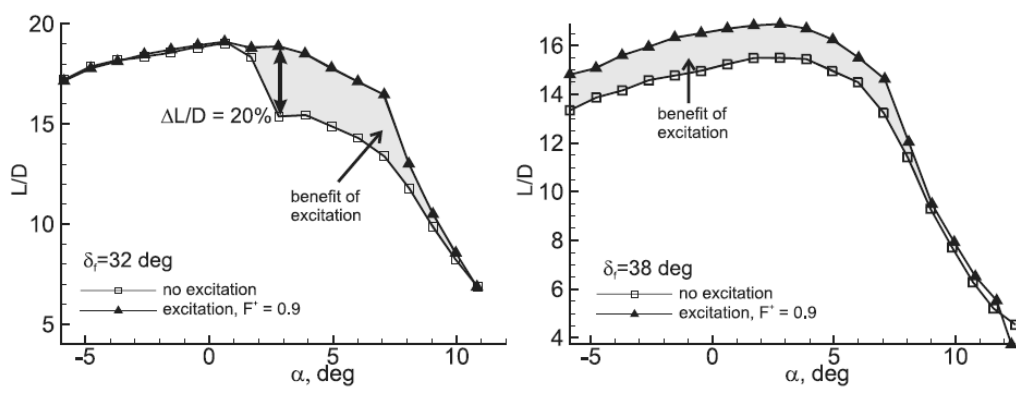
Figure 2.14: Lift-to-drag ratio for two flap deflection angles with and without excitation [27].

Chapter 3

Flow control applications

In previous chapter different passive and active flow control methods were mentioned. In this chapter these passive flow control methods are discussed in more detail, together with the introduction of active flow control by means of DBD plasma actuators.

3.1 Passive flow control

The first example of a passive flow control method is the use of turbulators. A turbulator is a small device which locally increases the surface roughness to trip a laminar boundary layer into turbulence. The turbulent boundary layer contains more energy and stays longer attached to the surface [3]; this effectively moves the separation point further aft on an airfoil and possibly eliminating separation completely. The consequence of a turbulent boundary layer is an increased skin friction relative to a laminar boundary layer, but this is very small compared to the increase in drag associated with separation. The artificial transition can be realized by the application of a zigzag tape, carborundum grains or any other form of roughness. Although this is a very straightforward manner, the effectiveness depends on several parameters, e.g. zigzag angle and roughness hight, which are best optimized by trail and error.
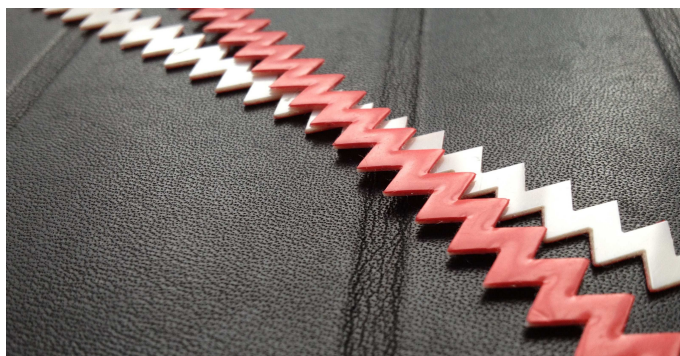
Figure 3.1: Example zigzag tape.

The next well known passive technique for separation delay is the use of vortex generators (VG's). These devices can take several shapes, but usually their height should be in the order of boundary

layer thickness. On aircraft vortex generators are installed on the front third part of the airfoil, positioned obliquely so that they have an angle of attack with respect to the local airflow (see Figure 3.2). As the flow passes through, tip vortices are created which "re-energize the boundary layer"; rapidly-moving air outside is mixed with the slow-moving flow inside the boundary layer. This way the aerodynamic characteristics of an airfoil are improved by postponing separation. Literature [20] has demonstrated that similarly vortex generators can also be applied on the flap of a wing-flap model.
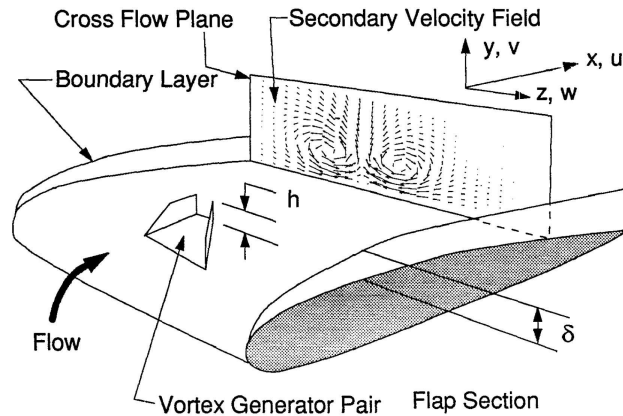
Figure 3.2: Vortex generators pair arranged at alternating incident angles to produce counter-rotating vortices [20].

Another group of passive flow controls are based on wall shaping and movable surfaces. A concrete example is the self-activated movable flap, which is based on the observation of bird flight [32]. For low angles of attack the flap stays down on the airfoil's surface. When due to an increased incidence separation and reversed flow occurs at the trailing edge of an airfoil, the flap pops up. This way the flap blocks the separated region and prevents to move further upstream. As a result flow separation is delayed and a higher lift coeficient is achieved. An example of this mechanism is shown in Figure 3.3.
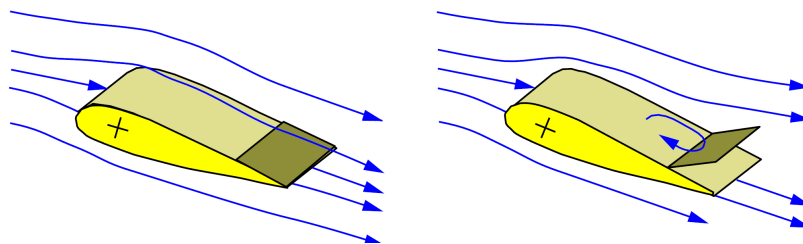
Figure 3.3: Concept of a movable flap: at low angles of attack the flap is closed (l) and pops up automatically at higher angles (r) [32].

3.2   Active flow control

The main active flow control application investigated in this research work is the asymmetric single DBD plasma actuator; this section discusses the physics and design for this type of actuator. Airflow control by means of plasma actuators made its real introduction in the year 2000. From then on

the amount of papers written on this subject has increased significantly [24]. The actuators consist basically of two electrodes, one exposed to the air while the other one is completely covered by a dielectric material. The two electrodes are connected to a power source. Figure 3.4 shows a schematic set up of the asymmetric DBD plasma actuator.
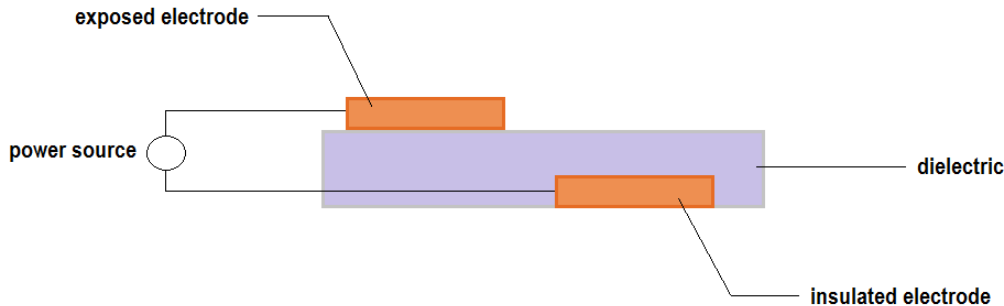
Figure 3.4: Schematic drawing of the asymmetric DBD plasma actuator.

Two major kinds of discharge can be distinguished for this actuator: the AC plasma discharge and the nanosecond (NS) plasma discharge [7]. The AC powered DBD plasma actuator, also referred to as the standard DBD plasma actuator, is the most common and widely used configuration. The nanosecond pulse driven DBD plasma actuator has only been applied since recently, but has become increasingly popular. Although they show great similarities in configuration, the working principle of both actuators differ significantly. This will be discussed in the next sections.

3.2.1   Physics of the AC DBD plasma actuator

In the case of a AC DBD plasma actuator, the electrodes are supplied with an AC voltage that at high enough levels (typically 5-20kV with frequencies ranging from 3-15kHz), causes the air over the covered electrode to ionize: a cold plasma discharge appears. The plasma, in the presence of the electric field produced by the electrode geometry, results in a body force vector that acts on the ambient air. The body force is the mechanism for active aerodynamic control. It pumps momentum into the boundary layer region and this way it can be used as a separation control mechanism [5]. Figure 3.5 shows an overview of this configuration.
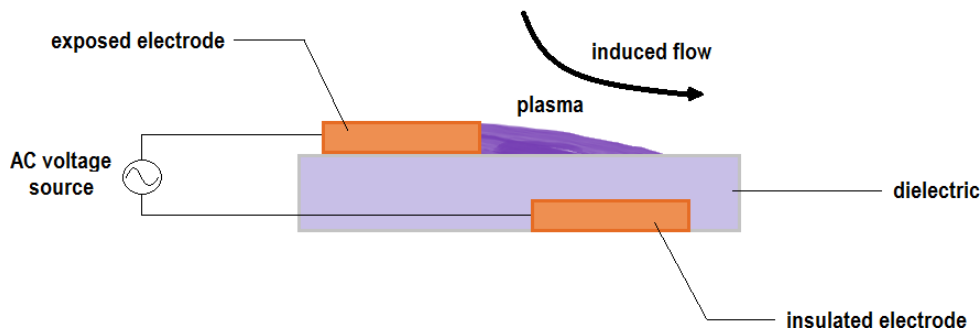
Figure 3.5: Schematic drawing of the AC DBD plasma actuator.

The ionization of the air is a dynamic process within the AC cycle. During one-half of the cycle, the exposed electrode acts like an anode where the encapsulated electrode acts like a cathode. In

the space between the two electrodes, electrons are extracted from neutral particles by ionization. Under the electric field, these electrons are accelerated towards the anode and ionize the gas by collisions with neutral molecules. The chemical reaction of the ionization process can be stated as follows:

$$A + e^- \rightarrow A^+ + 2e^- \tag{3.1}$$

where A is a neutral particle and A^+ a positive ion. This equation shows that one electron colliding with one neutral particle results in two electrons and one charged particle. Again these two electrons collide with two neutral particles to form four electrons and so forth. Consequently, an avalanche develops because the multiplication of electrons proceeds along their drift from the cathode to the anode. A discharge current is then created [24]. Through the collisions, momentum is transferred into the flow. It should be noted that the contribution of the electrons to the momentum transfer is small due to their low mass compared to the mass of the ions. The plasma is formed as the result of a series of discharges as electrons are transferred onto and off the dielectric surface.

The charge build-up of the electrons on the dielectric material causes the plasma actuator to be self-limiting at atmospheric pressures in the case the voltage is not continuously increasing. During the AC cycle, the electrons and ions move according to the electric potential, see Figure 3.6. During the first half-cycle, electrons move from the exposed electrode (serving as a cathode) to the encapsulated electrode (serving as an anode) and accumulate on the surface of the dielectric. In the next half-cycle the position of the cathode and anode exchange which causes the movement of the electrons to reverse. The plasma generation will eventually stop when the buildup of charge on the dielectric balances the AC potential. This self-limiting property (which appears as a glow discharge) avoids the creation of an unfavorable so-called arc discharge [28]. This electric arc can have detrimental effects on the electronic equipment and causes the plasma actuator to become unstable.

The basic mechanism of the actuator is that the plasma, in the presence of the electric field, results in a localized body force that is exerted on the external flow. The body force is proportional to the AC voltage amplitude and the volume of the plasma. Stated otherwise, the plasma actuator induces a pulsed velocity with the same frequency as the AC voltage. It should be noted that the induced velocity is higher during the negative half-cycle than the positive part.
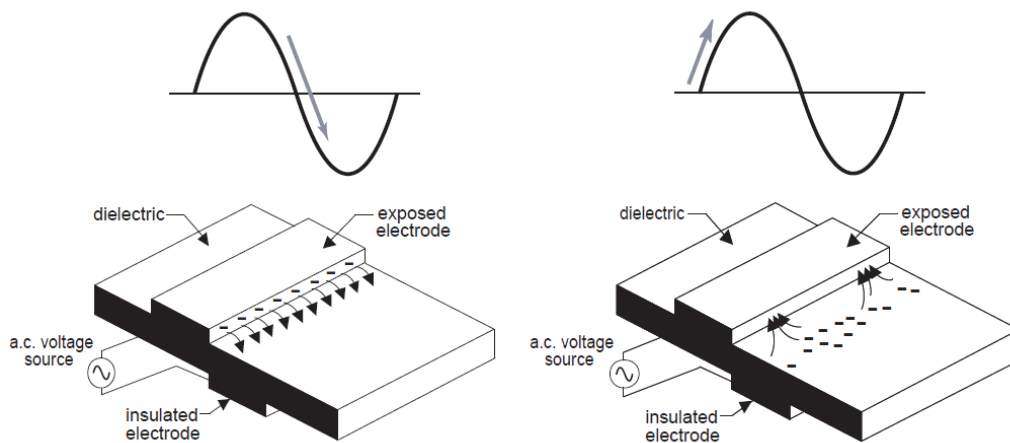
Figure 3.6: Charge buildup on the dielectric surface when the applied voltage is negative going (l), when the voltage reverses (r) [28].

Mechanical characteristics

The influence of the plasma actuator on the induced flow field is strongly dependent on geometric and electrical parameters. For separation control purposes, especially the maximum induced velocity and induced velocity profiles are interesting. Examples of parameters which could affect the generated plasma are: electrode gap, insulated electrode width, used materials and electric source frequency and voltage amplitude. Forte et al. [12] showed that an optimization of these geometrical and electrical parameters resulted in a maximum ionic wind velocity equal to $7m/s$ at 0.5mm from the wall for a single plasma actuator. For multiple actuators, this maximum induced velocity equals the amount of actuators placed multiplied by the maximum induced velocity per actuator [11].

Figure 3.7(a) shows the development of the maximum induced velocity with respect to electrode gap. One can see that there is a optimal electrode gap to obtain the largest induced velocity; exceeding this value of electrode gap reduces the velocity induction. Furthermore, the maximum induced velocity increases asymptotically with the insulated electrode width and the AC frequency (Figure 3.7(b) and 3.7(c)). The maximum velocity increases also with the applied voltage amplitude but not in an asymptotic manner (Figure 3.7(c)). The influences of the different parameters on the generated plasma, and thus on the induced ionic wind velocity, are collected in Figure 3.7.
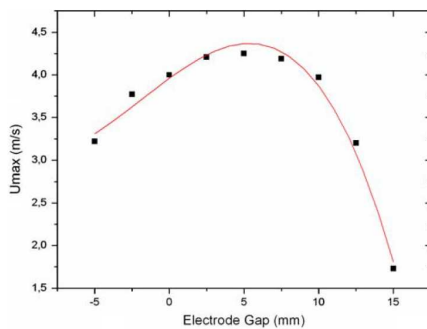
(a) Development of maximum induced velocity versus electrode gap.
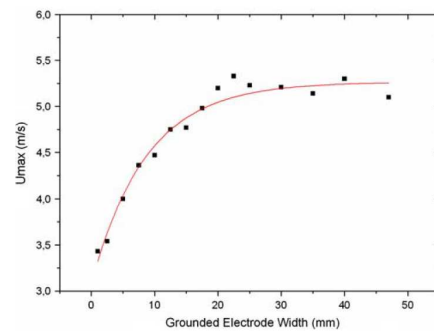
(b) Development of maximum induced velocity versus grounded electrode width.
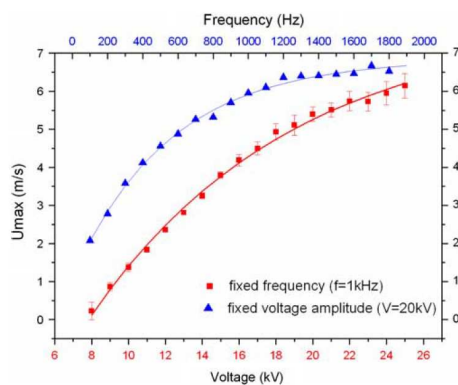
(c) Development of maximum induced velocity versus frequency and voltage.
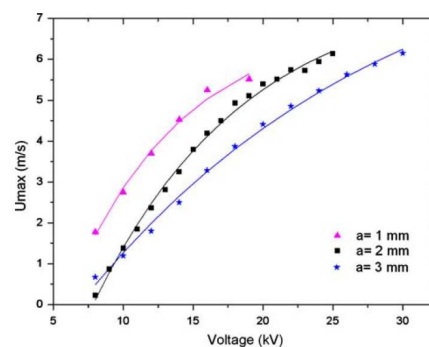
(d) Development of maximum induced velocity versus voltage for three actuators with different dielectric thickness.

Figure 3.7: Effects of geometric and electrical parameters on the generated plasma [12].

3.2.2   Physics of the NS DBD plasma actuator

The mechanism by which the nanosecond pulse driven DBD plasma actuator acquires flow control is significantly different from the AC powered one. The electrodes are now driven by high-voltage, pulsed periodic nanosecond excitation which causes the air over the covered electrode to ionize resulting in the appearance of a plasma discharge. Unlike the standard plasma actuator this results in near zero values of the actuator-induced flow velocities. Figure 3.8 shows an overview of the NS DBD plasma actuator configuration.
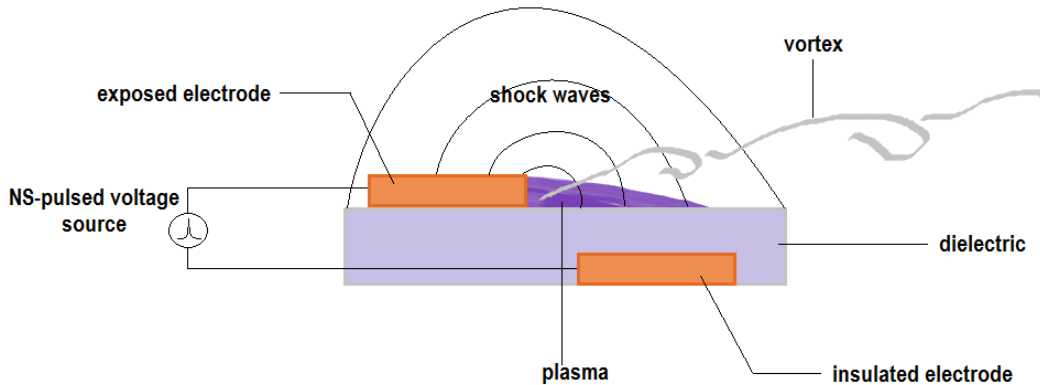
Figure 3.8: Schematic drawing of the NS DBD plasma actuator.

Roupassov et al. [31] performed measurements which have shown overheating of the discharge region at fast thermalization of the plasma imputed energy. Hereby 60% of the discharge energy was converted to heat in less than $1\mu s$. This thermal effect generates a local compression wave (shock wave), which on his turn is supposed to create secondary vortex flows, and disturbs the main flow. Consequently the phenomenon of separation can be controlled due to an efficient transversal momentum transfer into the boundary layer caused by the pulsed-periodic disturbance. The formation of shock waves are visualized by Roupassov from experimental shadow images and from CFD calculations (Figure 3.9).

The main mechanism for active aerodynamic control is thereby the energy transfer to and heating of the near-surface gas layer. The release of energy is sometimes defined as follows:

$$Q = U \times I \times \tau \tag{3.2}$$

where U is the applied voltage, I the time-averaged discharge current and τ the duration of the pulse. Whereas the heating of gas is defined by the following equation:

$$\Delta T = Q/c_p \tag{3.3}$$

It should be noted that these equations are valid under certain assumptions only: 1) the electric field energy is completely absorbed by the gas and 2) establishment of state of thermal equilibrium which is the case when the internal degrees of freedom of gas are in equilibrium with the translational degrees of freedom [31].

The most important benefit of the NS DBD plasma actuator is it effectiveness at higher velocities with respect to the AC DBD plasma actuator. Flow control by devices that rely on momentum addition becomes less effective as the velocity is increased [23].
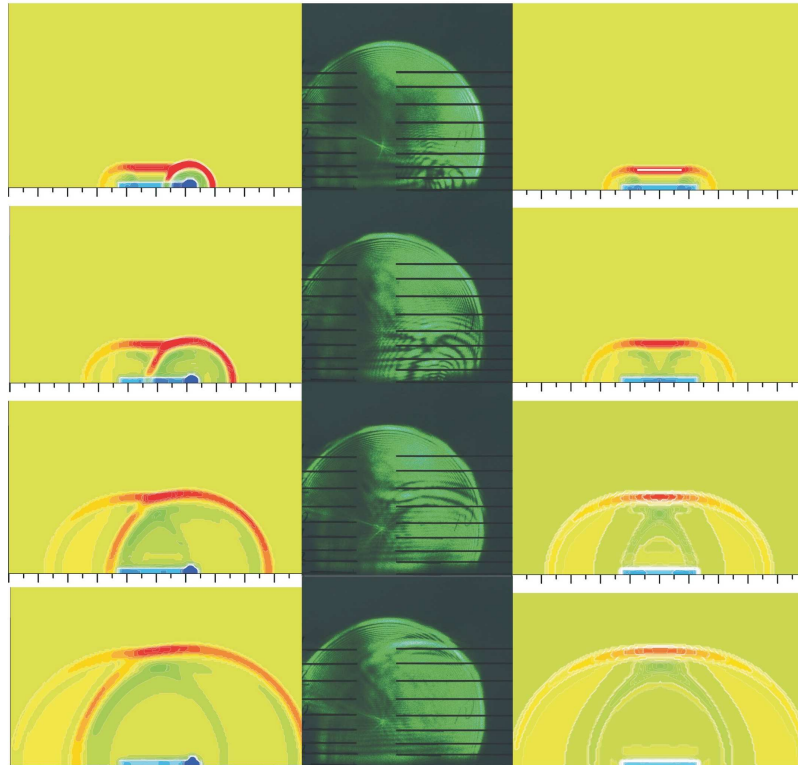
Figure 3.9: Dynamics of flow development near surface. From top to bottom: 4, 8, 16 and 25 μs after discharge. Single scale division both in horizontal and vertical directions correspond to 1 mm. Left column: discharge with "hot spot" near the edge of the exposed electrode (numerical simulation). Right column: homogeneous energy distribution (numerical simulation). Center: experimental shadow images of shock waves formation. Pulse duration is 50 ns [31].

Mechanical characteristics

Flow control authority by the NS DBD plasma actuator is achieved by the energy transfer to and heating of the surrounding gas. Although geometric parameters, such as actuator configuration, actuator dimensions and used materials, definitely influence the generated plasma, the effectiveness of this control mechanism relies more on electrical parameters. Roupassov et al. [31] studied the plasma impact on the flow around a C-16 airfoil model and a parametric study was carried out including the following variables: (discharge) frequency, pulse duration and voltage amplitude. In their work it is shown that the mean values of the occurring heating for the plasma layer can reach 70, 200 and even $400K$ for 7, 12 and $50ns$ pulse duration, respectively.

The shock wave which appears due to gas layer overheating can be calculated using one-dimensional theory, under the assumption that the heating occurs in a constant volume regime. For example, a relatively weak heating of $\Delta T \sim 200K$ results in a shock wave with $M = 1.13$ near the surface. Figure 3.10 shows the dependence of shock wave Mach number on overheating ratio.

Figure 3.11 shows the values of the induced flow velocity generated by nanosecond pulse driven DBD plasma actuator as a function of the pulse repetition frequency. It confirms that this type of actuator produces near zero values of actuator-induced flow velocities. The maximum induced
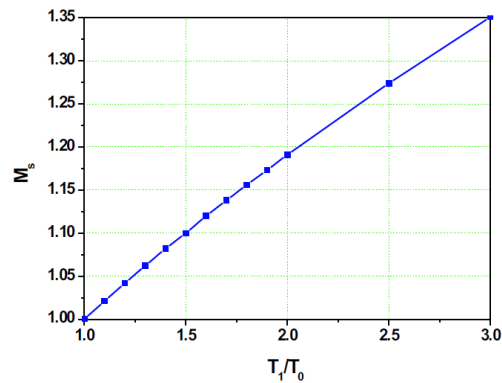
Figure 3.10: Dependence of shock wave Mach number on gas layer overheating [31].

velocity is less than $0.3m/s$ which is substantially lower than the one produced by the standard plasma actuator.
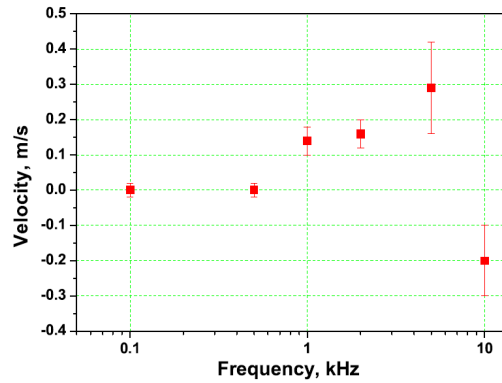
Figure 3.11: Dependence of actuator-induced velocity on pulse frequency [31].

Figure 3.12 shows the lift force dependency on discharge frequencies. In Figure 3.12(a) the electrodes were placed perpendicular to the main flow whereas in Figure 3.12(b) they are positioned parallel. One can observe that the plasma impact is similar for both. This confirms the fact that the impact of discharge is attributed to more than gas acceleration only; vortex formation and flow turbulization might be the driving mechanism of flow separation control.
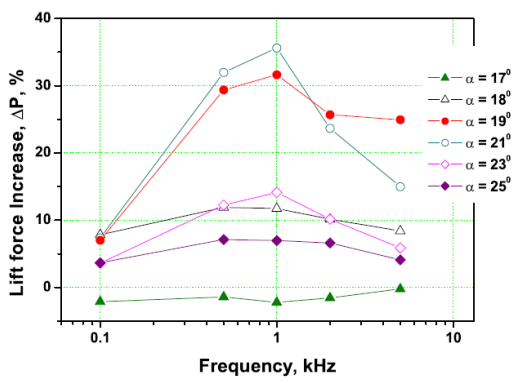
(a) Discharge parallel to flow.
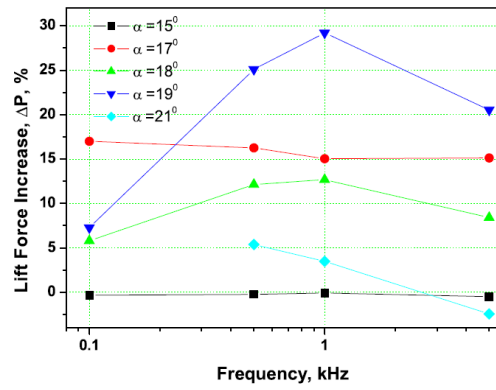
(b) Discharge perpendicular to flow.

Figure 3.12: Dependence of lift force on discharge frequency for different α (at $110m/s$) [31].

3.2.3   State of the art

AC DBD plasma actuator

Little et al. performed multiple studies on separation control using DBD plasma actuation. In one of the works [21] separation control from the flap of a high lift airfoil was examined. More specifically, this test model was a simplified high lift version of the so-called NASA Energy Efficient Transport (EET) airfoil, see Figure 3.13. For this study the control effectiveness for two actuator locations was investigated as well as various reduced frequencies, applied voltages and waveforms.
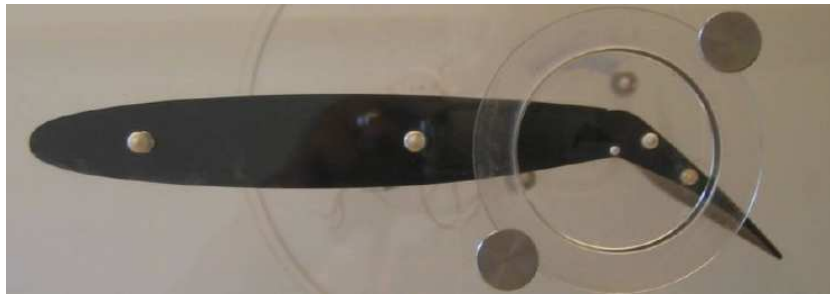
Figure 3.13: Simplified high lift EET airfoil with deflected flap [21].

A previous study [18] showed that an actuator positioned slightly upstream the separation location is more effective. Little et al. utilized this finding and located for the first test an actuator at $x/c = 0.60$, which is well upstream the separation point. For the second test the actuator was moved to $x/c = 0.75$, on the flap shoulder. Both tests were carried out using a sinusoidal amplitude modulation, airfoil at zero incidence with 30° flap deflection and a Reynolds number of $0.24 \cdot 10^6$ ($\approx 15m/s$). It was shown that an actuator located at the flap shoulder can slightly increase or reduce the size of the time-averaged separation bubble over the flap depending on the frequency of actuation. Thus by moving the actuator to the flap shoulder, additional control authority could be achieved. Additionally, the effectiveness of plasma actuation was not improved by an increase in applied voltage or a change from sinusoidal to positive sawtooth waveform.

Also an attempt was made within this field to show the potential of AC DBD plasma actuator as a replacement of the leading-edge slat and the trailing-edge flap of an airfoil (Corke et al. [15]). To mimic their effects, an array of plasma actuators was placed on the leading edge ($x/c = 0.0$) and an array of plasma actuators on the trailing edge ($x/c = 0.9$). Flow control tests were conducted at chord Reynolds numbers of $0.217 \cdot 10^6$ and $0.307 \cdot 10^6$. Figure 3.14 illustrates the test model.
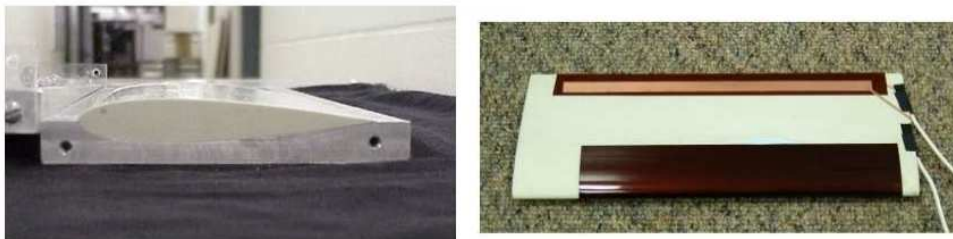
Figure 3.14: NACA 0015 airfoil model with leading-edge (plasma slat) and trailing-edge (plasma flap) actuators [15].

The leading edge separation control resulted in an increase in both C_{lmax} and α_{stall} and a lift-to-drag improvement of as much as 340%. The trailing edge actuator was found to produce the same

effect as a plain trailing edge flap. This included a uniform shift at all angles of attack of the lift coefficient and a shift toward higher lift coeffients of the drag bucket.

It should be noted that one of the main drawbacks of these studies is the simplification of the airfoils. The effects of gaps, mentioned by A. M. O. Smith [33] (Section 2.3), as well as the possible interaction with plasma actuator physics were ignored. The obtained results may therefore be appointed as rough approximations but definitely not representing the slotted multi-element airfoil. Another drawback is that the operating Reynolds numbers were relatively low, thus these studies does not guarantee the effectiveness of DBD plasma actuation when operating at higher Reynolds numbers.

A parametric experimental investigation by Thomas et al. [35] aimed at optimizing the body force produced by DBD plasma actuators used for aerodynamic flow control. A primary goal of the study was the improvement of actuator authority for flow control applications at higher Reynolds number than previously possible. The study examined the effects of dielectric material and thickness, applied voltage amplitude and frequency, voltage waveform, exposed electrode geometry, covered electrode width, and multiple actuator arrays. The metric used to evaluate the performance of the actuator in each case was the measured actuator-induced thrust which was proportional to the total body force. They demonstrated that actuators constructed with thick dielectric material of low dielectric constant produce a body force that is an order of magnitude larger than that obtained by the Kapton-based actuators used in many previous plasma flow control studies. These actuators allow operation at much higher applied voltages without the formation of discrete streamers which lead to body force saturation.

NS DBD plasma actuator

NS DBD plasma actuators are successfully tested for flow separation control at high Reynolds and Mach numbers [7][23][29][31], although in the field of separation control on two element airfoil models the amount of literature is rather limited. Some examples of succeeded flow control on single element airfoils are shortly discussed hereafter.

In a work of Little et al. [23] the efficacy of DBD plasmas driven by repetitive NS pulses for flow separation control was investigated experimentally on an airfoil leading edge up to $Re = 1 \cdot 10^6$ ($62m/s$). The NS pulse driven DBD plasma actuator transfers very little momentum to the neutral air, but generates compression waves similar to localized arc filament plasma actuators. Experimental results indicated that NS DBD plasma performs as an active trip at pre-stall angles of attack and provides high amplitude perturbations that manipulate flow instabilities and generate coherent spanwise vortices at post-stall angles. These coherent structures entrain free stream momentum thereby reattaching the normally separated flow to the suction surface of the airfoil.

In another work by Rethmel et al. [29] the ongoing development on the use of NS DBD plasma actuators for high Reynolds numbers aerodynamic flow control is shown. Leading edge separation control on an 8-inch chord NACA 0015 airfoil was demonstrated at various post-stall α for Reynolds numbers and Mach numbers up to $1.15 \cdot 10^6$ and 0.26 respectively ($U_\infty = 93m/s$). The NS-DBD can extend the stall angle at low Re by functioning as an active trip. At post-stall α, the device generates coherent spanwise vortices that transfer momentum from the free stream to the separated region, thus reattaching the flow. The impact of actuation on the separated flow is visualized in Figure 3.15.

(a) Actuation off.   (b) Actuation on.

Figure 3.15: Smoke flow visualization at $Re = 1.15 \cdot 10^6$ and $\alpha = 18°$ with NS DBD plasma actuator "off" (a) and "on" at $F^+ = 2.75$ (b) [29].

Chapter 4

Experimental setup

This chapter describes the aspects related to experimental setup of the research project. As the focus is on a two element airfoil, a wing-flap model was chosen that was already available for windtunnel testing. This model together with the flow facility in which the experiments were carried out and other relevant topics will be discussed in this chapter.

4.1 Experimental facility: Low Turbulence Tunnel

The experiments of this research were conducted in the Low-Speed Low-Turbulence Windtunnel (LTT) of Delft University of Technology. This atmospheric tunnel is of the closed-throat, single-return type and was constructed around and through a building, see Figure 4.1. A six-bladed fan is driven by a 525 kW DC motor, giving a maximum test section velocity of about $120m/s$. The maximum Reynolds number for two-dimensional testing is about 4.8 million based on a chord model of 0.6m.

The combination of anti-turbulence screens located in the settling chamber and a high contraction ratio of 17.8 results in an uniform velocity profile with a low free-stream turbulence level in the test section; variation from only 0.015% at $20m/s$ to 0.07% at $75m/s$. The interchangeable octagonal test-section is 1.80m wide, 1.25m high and 2.6m long.

Mechanically actuated turntables flush with the test-section top and bottom wall provide positioning and attachment for a two-dimensional model. The standard windtunnel testing equipment consists of an electronically read 200 tubes multi-manometer with fiber optic cells, a 6-component balance, a 192 ports electronic pressure scanner system and hot wire anemometry and PIV systems. For flow visualization purposes an infra-red camera system is available. Data are recorded using an electronic data acquisition system and are on line reduced using the laboratory computer. To perform pressure measurements for a test model, the software package profmeas was used. This program allows the user to measure, store and correct the data from each test.
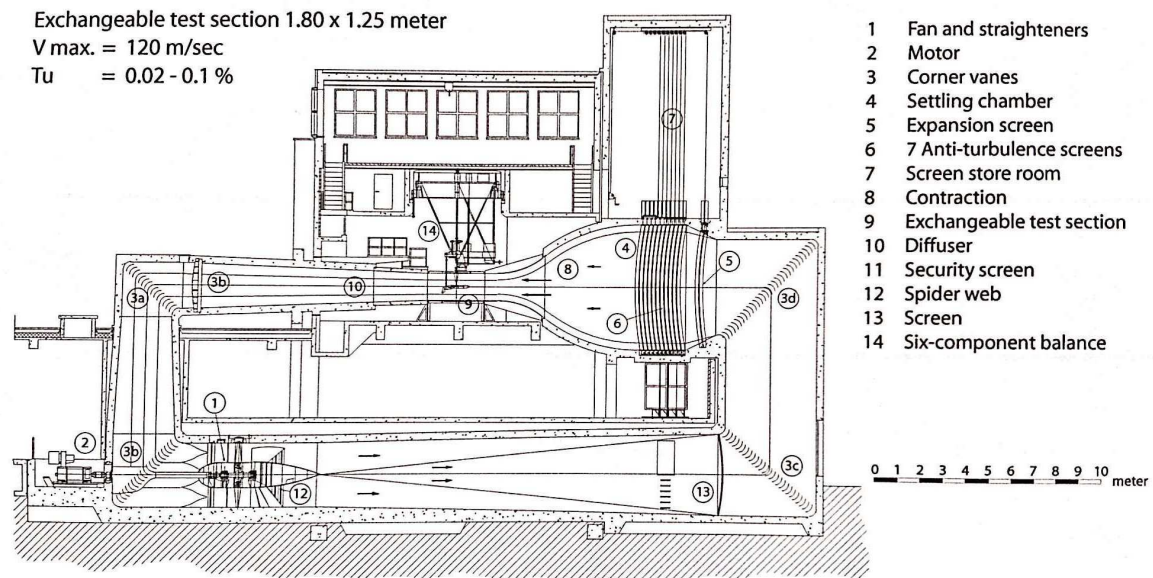
Figure 4.1: Schematic layout of the Low-Speed Low-Turbulence Windtunnel [4].

Figure 4.2: Overview LTT test section area.

4.2   The wing-flap model

The wing-flap model used for this research project has its roots in the early 90's when the Extra company started the EA-400 project in cooperation with the Delft University of Technology. The airfoil's design requirements were defined as a $C_{lmax} \geq 3.2$, drag as low as possible at a $C_{ldesign} \geq 0.4$, stall characteristics at least equal to the NLF-416 airfoil and the implementation of a flap. Finally, the end product of this cooperation was the Natural Laminar Flow airfoil modification number 22(A) (NLF-MOD22(A), see Figure 4.3). Extensive testing however of model A resulted in a redesign of the slot entrance combined with the application of a zig zag tape just upstream of where the new flap cove starts (latter to eliminate a laminar separation bubble); these adjustments realized lower drag of the airfoil [4]. The new modified airfoil was appointed as the NLF-MOD22(B) which is also the model used for this research project, shown in Figure 4.4.
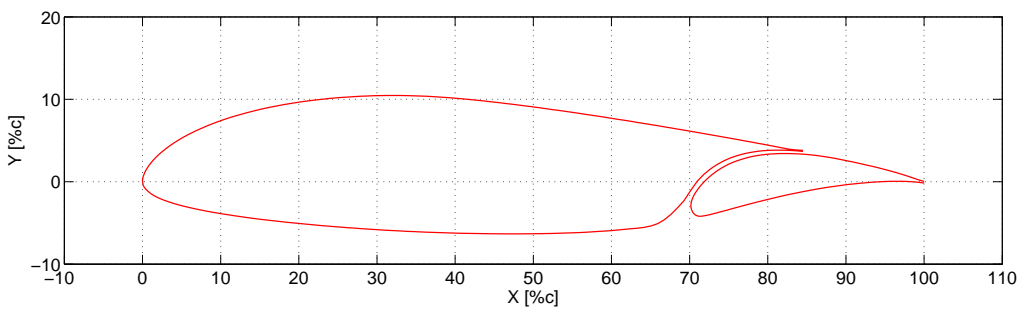
Figure 4.3: The NLF-MOD22(A) airfoil, showing the main element and the flap.
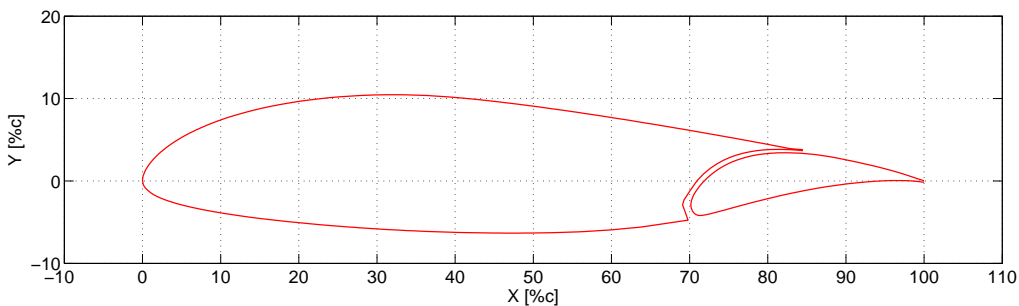
Figure 4.4: The NLF-MOD22(B) airfoil, showing the main element and the flap.

In the flap-nested configuration model B has a chord of 0.6m and with its length of 1.25m it spans the entire tunnel height (Figure 4.5). The model is installed vertically between rectangular endplates which are flush with the turntables. The axis of rotation of the turntables was at 50%c. The flap is of a fowler type with a chord length of 30%c. Figure 4.6 shows the geometric details of the flap settings defined by the gap, overlap and deflection. The definition of the flap deflection is set as the chord line of the flap in nested position.

Hence, the NLF-MOD22(B) is characterized by the sharp slot entry shape resulting in a small gap between the lower surface of the wing and the retracted flap. For pressure measurements, a total of 56 pressure orifices on the main wing and 28 on the flap (0.4mm diameter) were located in diagonal rows between 0.45m and 0.55m from the bottom of the test section. This pattern was designed to minimize interference effects from upstream pressure orifices with downstream ones. To prevent three-dimensional separated flow near the tunnel walls as a result of early separation, boundary layer suction was applied through 5mm diameter holes with centres spaced 10mm apart and from

the main wing. Near the flap surface the suction is applied through 4mm diameter holes with centres spaced 8mm apart, see Figure 4.7.
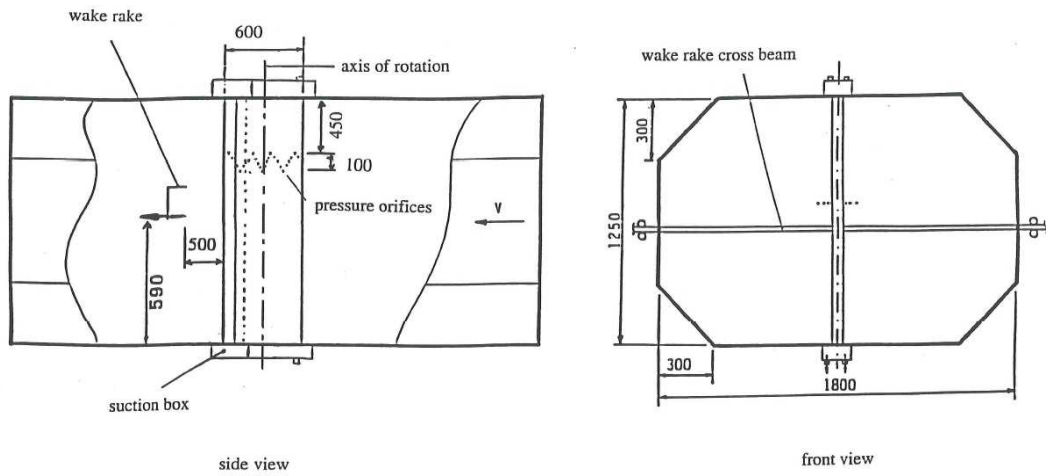
Figure 4.5: Model setup in the windtunnel section [4].
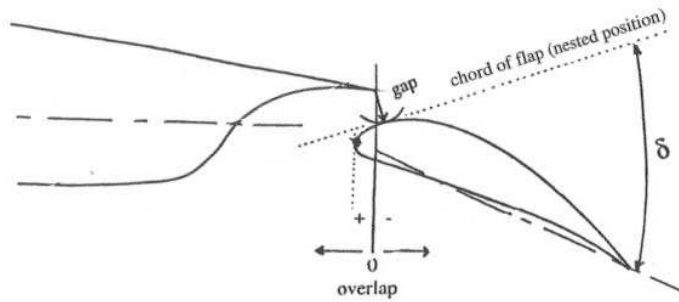
Figure 4.6: Gap and overlap definitions [4].
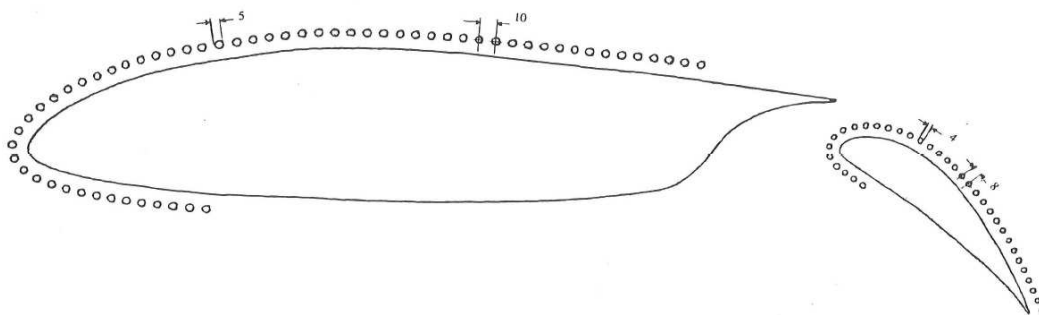
Figure 4.7: Suction orifices at the windtunnel wall [4].

4.3   Multi-manometer and wake rake

To complete the test setup two important instruments are required to extract flow data around the test model: the wake rake and the multi-manometer (MMM device). The wake rake was placed downstream, in transversally direction with respect to the model. In Figure 4.9 the rake position in the windtunnel is shown. This instrument, consisting of 50 total and 12 static pressure tubes, was capable of measuring the momentum defect due to the wake. To monitor the pressure distribution in a wake and along the test model, the pressure orifices are directly connected to the MMM device (Figure 4.10) by means of small plastic tubes. On his turn, by linking this device to the LTT computer, data could be transferred to the previously mentioned program - profmeas. It returns a plot of the C_p distribution along the chord line and calculates the aerodynamic coefficients e.g. C_l and C_d.

With the wake rake adjustable in height, wake traverse measurements were performed to check the two-dimensionality of the flow and to find a wake rake position giving a representative drag for the model. In Figure 4.8 a traverse is shown for 0° angle of attack and a flap deflection of 45° at a Reynolds number of $1.7 \cdot 10^6$. This angle is in the range of angles of attack in which the model deals with largely attached flow around the main wing element.
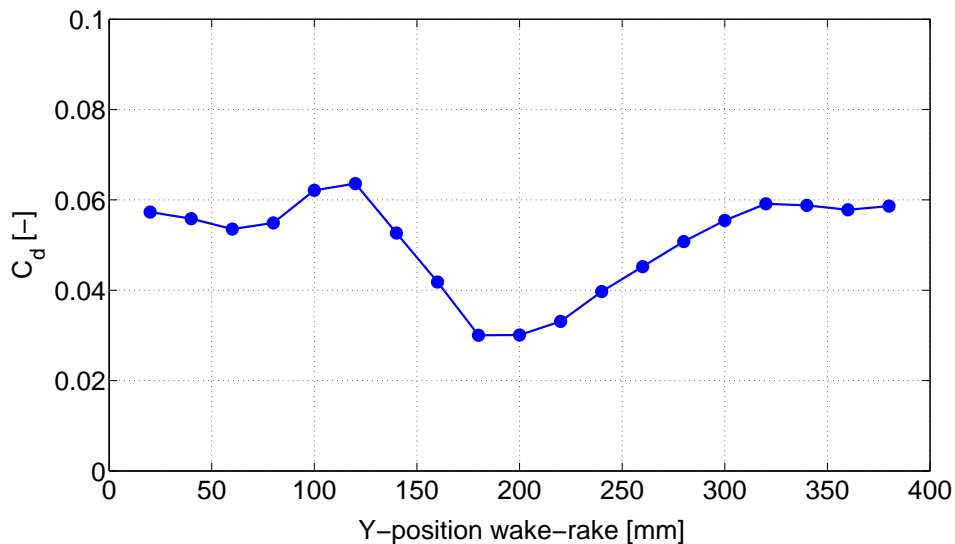
Figure 4.8: Wake rake traverse measurements showing the effect on span wise wake drag at $\alpha = 0°$ and $Re = 1.7 \cdot 10^6$.

The figure clearly illustrates the strong three-dimensional character of the flow due to separation on the flap. Therefore for further experiments a relative stable and fixed wake rake position of y = 200mm is chosen. At this height the calculated drag is less sensitive to fluctuations.
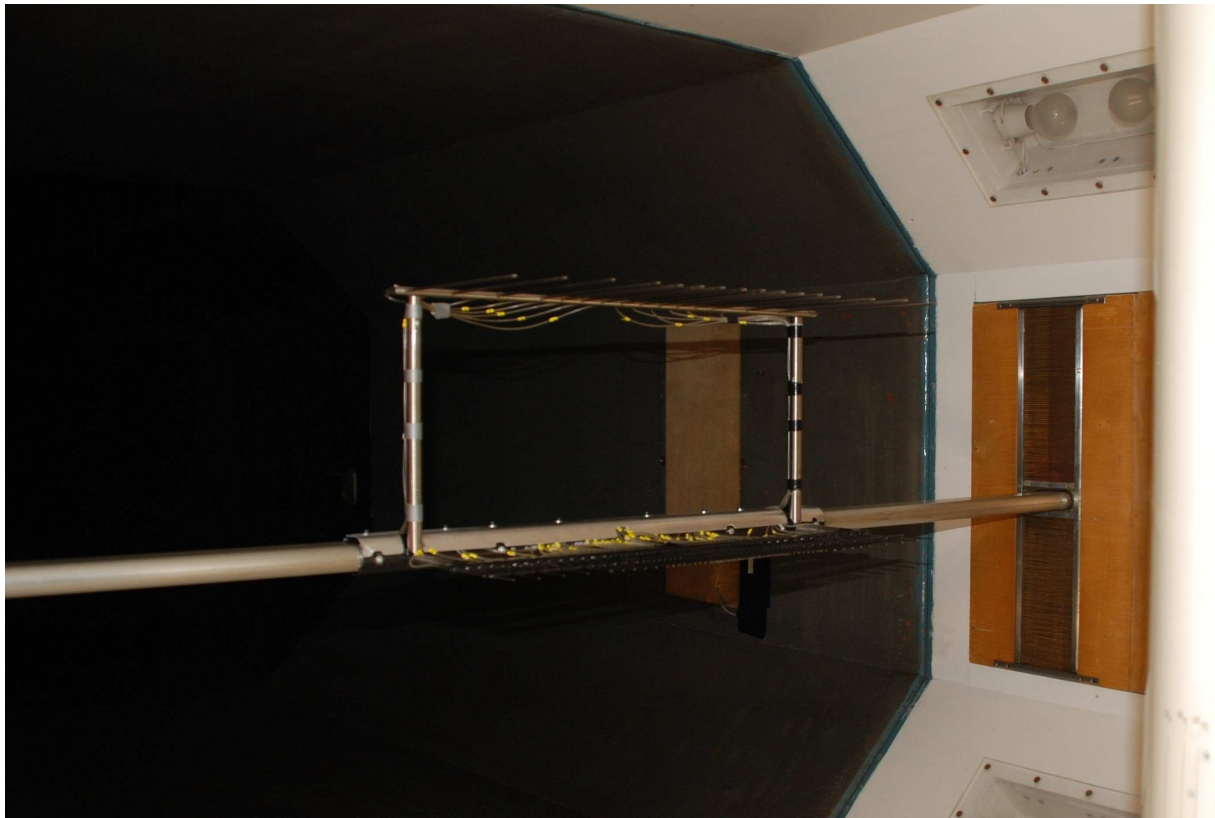
Figure 4.9: The wake rake inside the windtunnel for wake measurements.

Figure 4.10: The multi-manometer for pressure monitoring.

Chapter 5

Experimental results

Nowadays, most experiments on DBD plasma actuators are focused on the understanding of its fundamental physics and applications, which so far makes DBD plasma actuation merely a laboratory-tested device. One of the current research goals is to bring some added value for future progress. To bring the DBD plasma actuator a step closer towards the implementation in real life cases. Of course, this should not reduce the importance of understanding the basic principles of DBD plasma actuators.

Hence, motivated by the positive separation control on single element airfoils shown in the experimental work of Correale [6], the intention of this work was to apply flow control on more applied cases i.e. separation control on multi-element airfoils. In addition to the active flow controls also specific passive flow control devices will be investigated. Furthermore, the airfoil model used for the research has a fixed flap deflection of $\delta_f = 45°$ and is characterized by separated flow on the flap at low angles of attack. As α is increased the wake from the main wing suppresses the pressure distribution on the flap and eventually the flow gets attached on this part of the airfoil. This means that beyond $C_{l,max}$ the flow is completely separated from the main wing whereas it is attached on the flap. Improving $C_{l,max}$ is therefore out of the scope of this research. Instead the focus is on how to deal with the separated flow on the highly deflected flap, before stall occurs. To what extent are flow control techniques able to delay, or maybe even to prevent completely separation on the flap. The experimental part of the analysis is discussed in this chapter.

5.1   Model baseline data

The NLF-MOD22(B) airfoil model is subjected to numerous tests in this research. Before getting started with the study of flap applications it is important to see what the exact aerodynamic properties are for this model in the configuration as it is. At the lower surface of the main wing four small metal plates were attached (at around 65%c) which served as support elements from a previous research (see Appendix Figure A.2). That research might need a followup study therefore it was decided to leave those support elements on. Also at this lower surface chord postion a zigzag tape was attached with thickness of 0.55mm. This resulted from previous work on the same model done by Boermans [4]: artificial tripping on the lower surface is needed in order to eliminate a detrimental laminar separation bubble on the flap's lower surface. As mentioned earlier, the model

has a fixed flap deflection of 45°. This is kept constant for all the upcoming experiments. In fact it was possible to change the flap deflection, although this was a rather complicated and time consuming task. In addition, the focus of this work is on critical flight conditions; more specifically on high flap deflection angle and high Reynolds number ($Re = 1.7 \cdot 10^6$). To get a feeling for this, these numbers are potential conditions at landing configuration.

The pressure distributions for the selected configuration are shown in Figure 5.1. The airfoil is characterized by a pressure peak on the flap nose, a fast trailing edge stall of the main airfoil as indicated by the trailing edge separation on the main airfoil which suddenly moves forward after 11.3° angle of attack, and partially separated flow on the aft side of the flap for low α indicated by the flat pressure distribution. As α is increased the flap's upper surface pressure distribution is being more and more suppressed by the displacement effect of the main airfoil wake above the flap. This finally leads to attached flow on the flap over its full length at angles of attack beyond 11° and a decrease of the flap's pressure peak (i.e. no separation on the flap at and beyond stall). Now decreasing the angle of attack causes the flow on the main airfoil to reattach at 10° angle of attack (hysteresis loop is not shown), where the lift coefficient becomes less than previous $C_{l,max}$. The baseline characteristics are shown in Figure 5.2. The maximum lift coefficient is 3.2 at about $\alpha = 11.3°$. The drag coefficient increases in a slightly exponential fashion until the point of $C_{l,max}$.
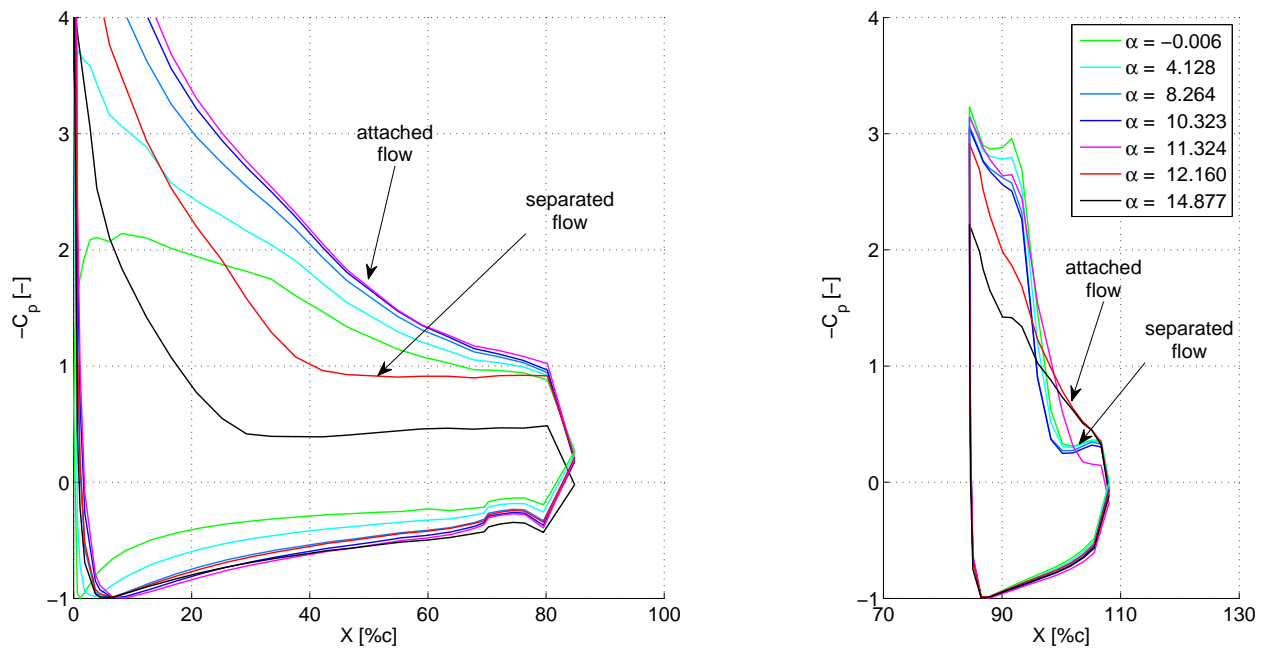
Figure 5.1: Baseline C_p distribution of NLF-MOD22(B) for $\delta_f = 45°$, $x_{overlap} = 0\%c$, $y_{gap} = 3.5\%c$ and $Re = 1.7 \cdot 10^6$ ($\approx 42m/s$).
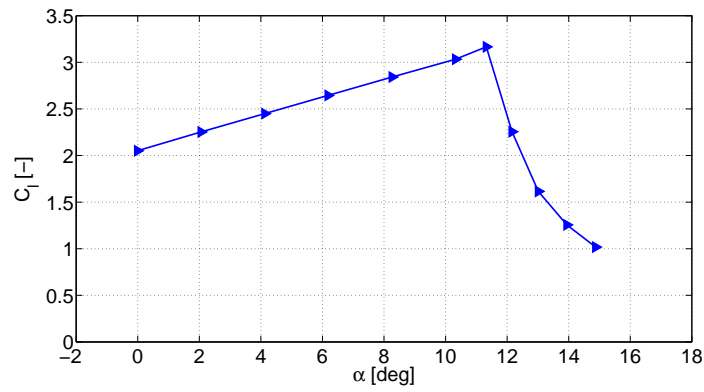
(a) C_l versus α.
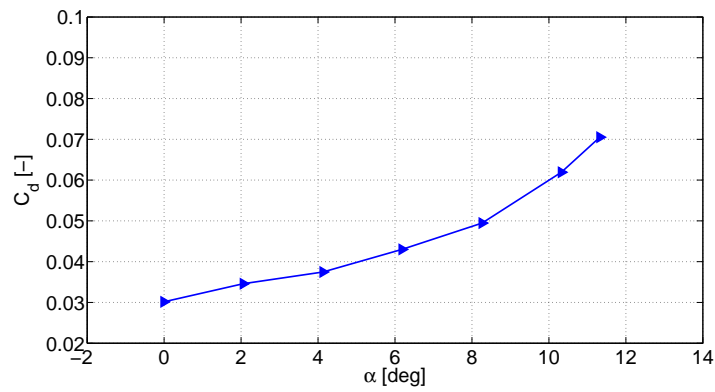
(b) C_d versus α.
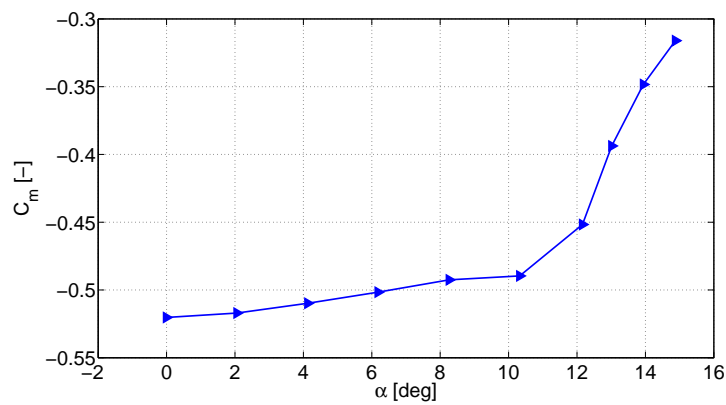
(c) C_m versus α.

Figure 5.2: Baseline aerodynamic characteristics of NLF-MOD22(B) for $\delta_f = 45°$, $x_{overlap} = 0\%c$, $y_{gap} = 3.5\%c$ and $Re = 1.7 \cdot 10^6$.

5.2   Oil flow visualization

To get some insight into the flow dynamics on the flap oil flow visualization experiments were conducted. As regards the time schedule (windtunnel availability) this was a very fast tool compared to the more comprehensive PIV technique to analyze the flow field. Firstly, the flap is lubricated with some kind of fluorescent oil. Thereafter the tunnel is turned on for a period of time giving the oil the opportunity to develop. Finally in a dark environment, the oil is illuminated with ultraviolet light to make the oil patterns visible. Note that this process is repeated for each single test. The results can be seen in Figure 5.3. Here the first row of pictures are taken at $0°$ angle of attack, the second row at $\alpha = 5°$ and the last row at $\alpha = 10°$ which is just prior to airfoil stall. Some additional remarks: the flow inlet is from the right and the small light blue squares are just pieces of tape to cover the pressure holes from oil flowing in.

In all the images, a long straight illuminated line is clearly visible just behind the flaps leading edge. Boundary layer flow over most wings will transition from laminar to turbulent flow at some point. This transition is often accompanied by a *separation bubble* that effectively makes the wing thicker in that region (see also Figure 2.10). In front of the bubble there is an extended separation zone where the laminar flow lifts and diverges from the surface. The airflow on the surface, beneath the separated laminar stream, is stagnant. This causes the straight fluorescent line. At the rear edge of the bubble, the separated flow plunges back to the surface. The mechanism that causes this and the impact with the surface generates turbulence in the attached flow that follows. This is both advantageous as detrimental. The bad part is that it results in more drag. The good part however is that turbulent flow stays attached to curved surfaces much better than laminar flow and this is very important e.g. for holding off the stall condition at low airspeeds. In addition, the short bubble appears stable at a fixed chord position for all incidences.

After this separation bubble the pictures show the occurrence of a remarkable phenomenon on the flap, known in literature as stall cells or mushrooms. When a plane rectangular wing (in this case the flap) is pitched up to angles close to and beyond stall, stall cells appear as the result of a periodic spanwise breakdown of the separated region. This spanwise periodic breakdown gives rise to independent stationary separated flow regions, in which the structure of the streamlines is organized around two counter-rotating loci. It should be noted that this phenomenon is not due to windtunnel adverse wall interference effects; it also occurs on finite wing models free of any significant wall interference [37].

The cells in Figure 5.3 behave quite similar for $\alpha = 0°$ and $\alpha = 5°$. The oil is being attracted by the multiple vortex-like movements which leads to an accumulation of oil at each vortex-center. This structure is identical to CFD calculations from [30], see Figure 5.4, where the influence of the flow's eigenmode is shown on stall cells creation.

Furthermore, there also seems to be some kind of balance between the cells, and as α is increased this balance is disturbed. At $\alpha = 10°$ a completely separated flow is noticed at one half of the flap, while the other half is still dominated by stall cells. The exact physics behind this instability remains unknown as it out of the scope of this research.
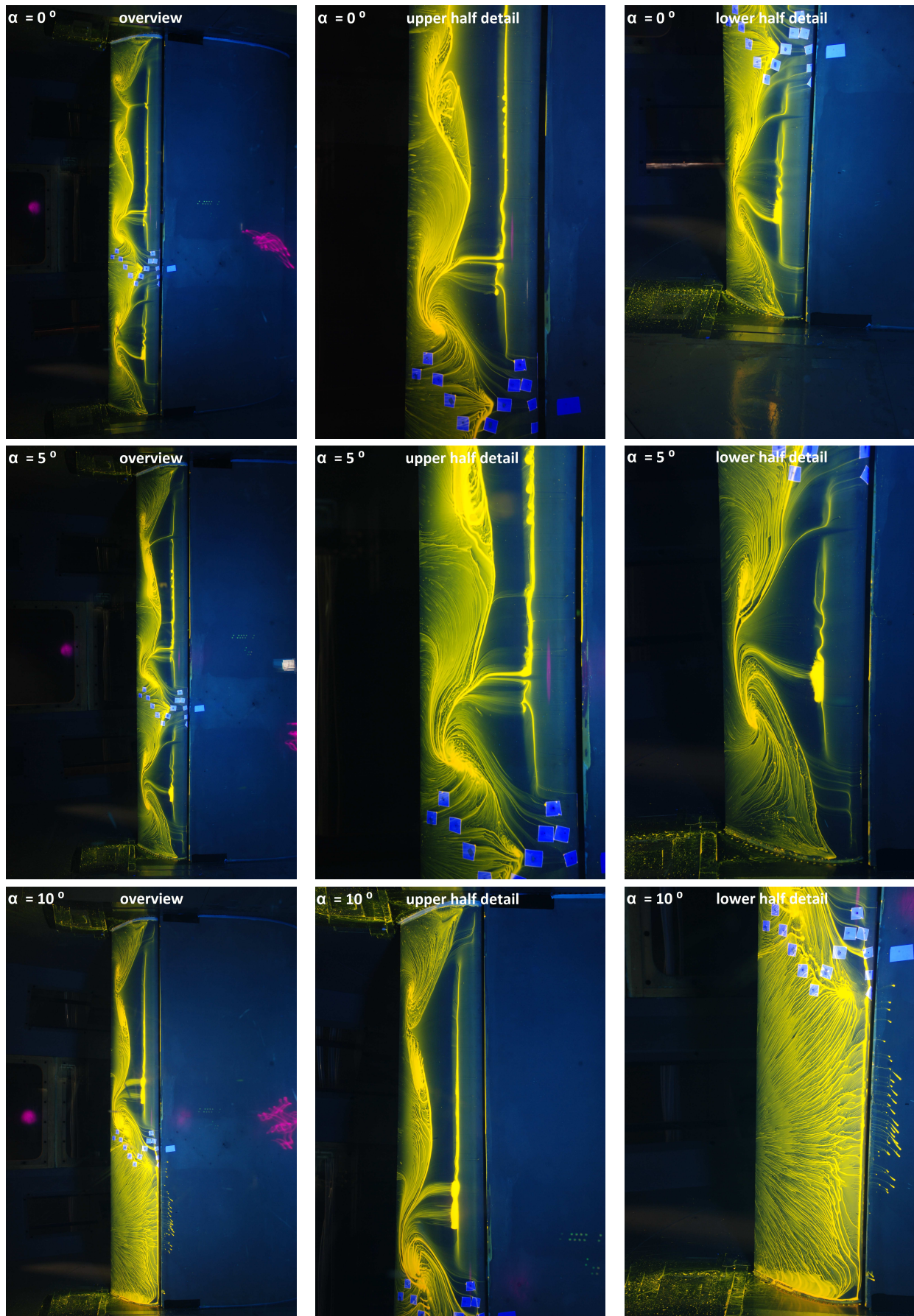
Figure 5.3: Oil flow visualization on flap only ($\delta_f = 45°$ and $Re = 1.7 \cdot 10^6$): first row at $\alpha = 0°$, second row at $\alpha = 5°$ and third row at $\alpha = 10°$. Structure from left to right: overview flap, upper half detail and lower half detail.
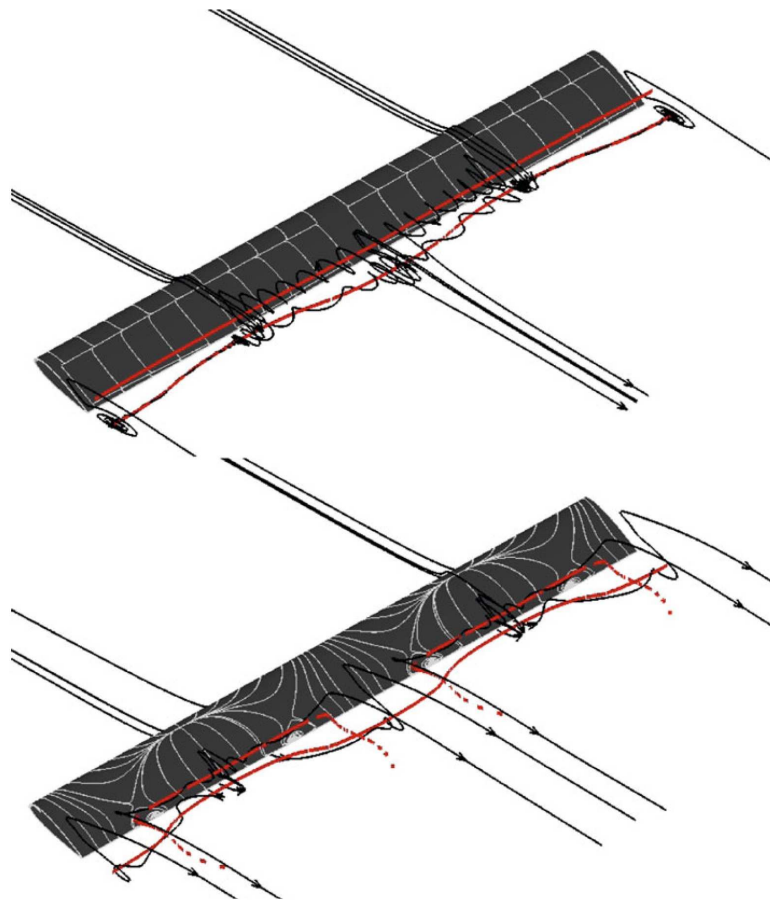
Figure 5.4: Three-dimensional reconstruction of the flow field around a stalled airfoil of its leading stationary three-dimensional eigenmode with amplitudes $\epsilon = 10^{-4}$ (up) and $\epsilon = 5 \cdot 10^{-3}$ (down). Shown are streamlines (black lines), surface streamlines (light grey) and vortex cores (red lines) [30].

5.3   Artificial transition

In order to delay or prevent flow separation the boundary layer should be energized as discussed in Chapter 2. In Section 3.1 some passive flow control methods were discussed to manipulate a flow field. There VG's were introduced: their presence results in the formation of co- or counter-rotating vortices, which transfer high momentum fluid down to the airfoil surface and delay separation. In the field of wind turbine blades VG's are commonly used applications. They are often used at the inner part of the blades located on the suction side between $10\%c$ and $30\%c$, resulting in a higher lift coefficient and at the same time increase the drag coefficient [3]. Flaps however are not that often equipped with VG's simply because space becomes an issue and of course the fact that passive methods can not be turned off when not needed.

In this section the effect of flap leading edge applications are investigated for three different kinds of passive tripping:

- zigzag tape

- carborundum grains

- "V" turbulator

Figure 5.6a shows the dimensions of the zigzag tape used with a 60° angle, a thickness of 0.205mm, a stream wise length of 11mm and a width of 3mm. Too thick zigzag tapes would cause to much additional drag, hence as requirement it had to be as thin as possible and still trip the boundary layer into turbulent flow.

Secondly the influence of a 10mm wide strip with carborundum 30 grains was tested, see Figure 5.6b. As this strip was manufactured by hand the exact density varies but it should be approximately $15 \sim 25$ grains per square cm with an average particle diameter of $632 \mu m$.

As last test case a semi-VG was investigated, i.e. the "V" turbulator, which should mimic the effects of a real VG. The idea was to cut a zigzag tape into pieces (see Figure 5.6c) to create this type of turbulators. As requirement it had to be sufficient thick to penetrate the boundary layer and create tip vortices from the edges, but still flexible enough to stay attached around the curvature of the flap. The most appropriate thickness was found to be the one of 0.85mm, and again with a 60° angle for each "V" shape.

All the trip types were mounted from $x/c = 0$ according to [3], i.e. the flap leading edge, towards the suction side just upstream the transition point, and cover the entire span. The transition point on the flap was showed to occur relatively stable in previous section, in contrast to the separation pattern which is highly dependent on the stall cell stability as α is increased. Therefore in the ideal case the tripping should be replaced each time α is changed so that tripping is initiated at the right position. Unfortunately, the LTT was available for a limited time and such elaborated cases would take too long.

The experiments were carried out at $Re = 1.7 \cdot 10^6$. Results are shown in Figure 5.7 for C_l versus α and C_d versus α for each roughness type. The "smooth"-line represents the clean flap configuration.

Focused on C_l, it is clear that the addition of any tripping type deteriorates the lift performance significantly with respect to the smooth configuration. It can be inferred from the figure that until the point of $C_{l,max}$ the airfoil delivers approximately 26%, 36% and 26% less lift for respectively the zigzag tape, carborundum and "V" turbulator. In terms of drag this is even worse; the airfoil is subjected to approximately 206%, 260% and 246% more drag for respectively the zigzag tape,

carborundum and "V" turbulator. Thus the smooth condition delivers more lift and less drag compared to the addition of any kind of tripping. The reason for this deterioration is because tripping initiates turbulent flow and increases the boundary layer thickness. Consequently the circulation on the flap decreases which also decreases the circulation on the main element; endresult is the total lift decrease and drag increase.

Also an important conclusion from the results is that the used "V" turbulator does not function as a VG at all, but more like a zigzag tape. Obviously VG's require more decent ways of production and implementation according to Hoerner and Borst [16]. The only practical problem is the lack of space on a flap, taking into account the small slot when the flap is retracted. Furthermore, to get VG's do their job they have to be placed in front of the separation point which leads to two issues: 1) in general separation point moves with δ_f so in theory the VG position should adapt to that for optimum excitation, and 2) even if δ_f is held fixed separation does not occur on one straight line as shown in Section 5.2, which makes it questionable of how to place these VG's correctly.

For the C_p distributions of the test cases one is referred to Appendix B.1.

Figure 5.5: "V" turbulator (l) and carborundum 30 grains (r) on flap's LE.
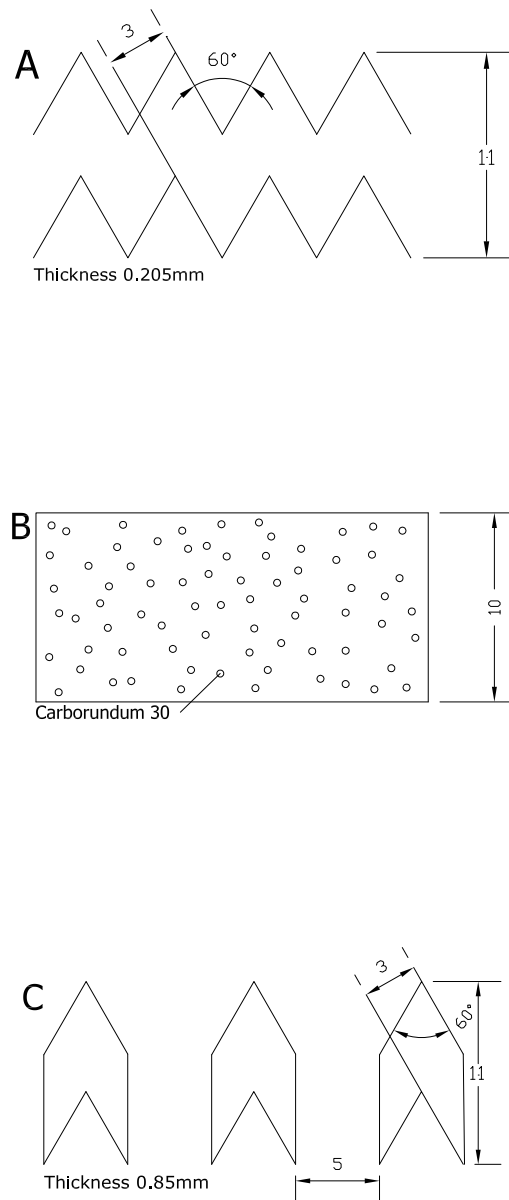
Figure 5.6: Schematic of roughness types (dimensions in mm): a) zizag, b) carborundum and c) "V" turbulator.
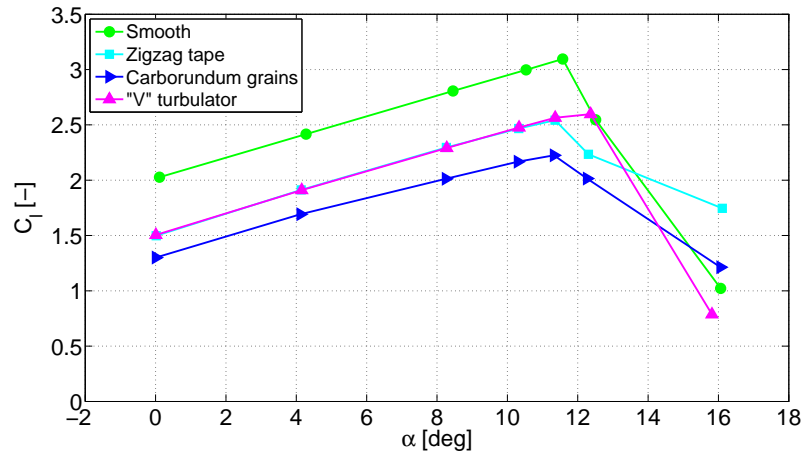
(a) C_l versus α.
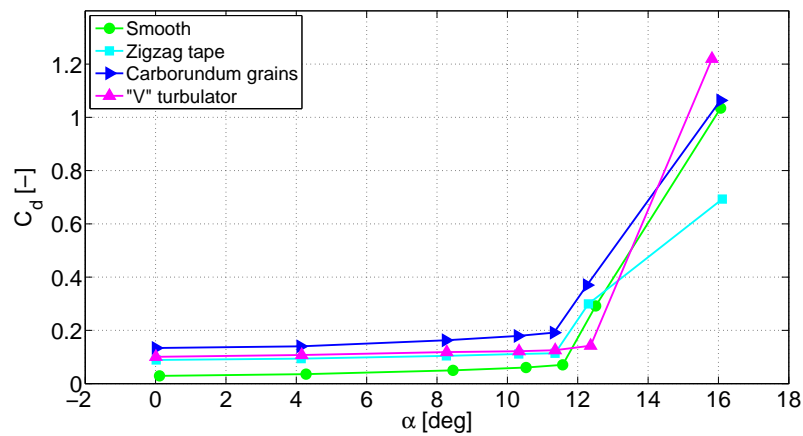
(b) C_d versus α.

Figure 5.7: Effects of artificial transition on the aerodynamic characteristics lift and drag for $\delta_f = 45°$, $x_{overlap} = 0\%c$, $y_{gap} = 3.5\%c$ and $Re = 1.7 \cdot 10^6$.

5.4   Length of roughness

Although in Section 5.2 the three-dimensional flow behaviour on the flap is clearly showed, tests in the LTT with the NLF-MOD22(B) are intended to be two-dimensional cases. As a sequel to the research on the influence of roughness types, the length and setup of the roughness is also analyzed. It has to be mentioned that these tests are not intended to improve anything, but as preparatory work for upcoming experiments more specifically for experiments with plasma actuators. These actuators are driven by a generator which can deliver a specific amount of maximum power, which could limit the effectiveness of an actuator in terms of generated body force, plasma or induced flow. As a consequence, this could also limit the size of an actuator since we are dealing with a rather large model. Therefore the following question arises: What is the minimum actuator length along airfoil's span to achieve a C_l within an acceptable threshold (i.e. 1%) compared to a span-sized actuator? To answer this question the problem is converted to a more covenient one: What is the minimum gap/strip length of roughness along the airfoil's span to achieve a C_l within an acceptable threshold (1%) compared to a clean airfoil? The idea is to determine the minimum gap or strip length, and thus the actuator length, at which the delivered lift force becomes quite independent of this length. The roughness which was attached to the flap's LE consisted of a 10mm wide tape with carborundum 30 grains (approximately $15 \sim 25$ grains per square cm). The two scenarios can now be described as follows (see also Figure 5.8):

1. A clean gap from the middle of the flap. This simulates a plasma actuator improving the flow in this region (enhancing separation delay) while at the sides the flow is still disturbed due to the roughness (Figure 5.8(a)).

2. A roughness strip from the middle of the flap. This simulates a plasma actuator disturbing the flow in this region (deterioration) while at the sides the flow is still attached (Figure 5.8(b)).

(a) Case 1: gap in middle without roughness.   (b) Case 2: strip in middle with roughness.
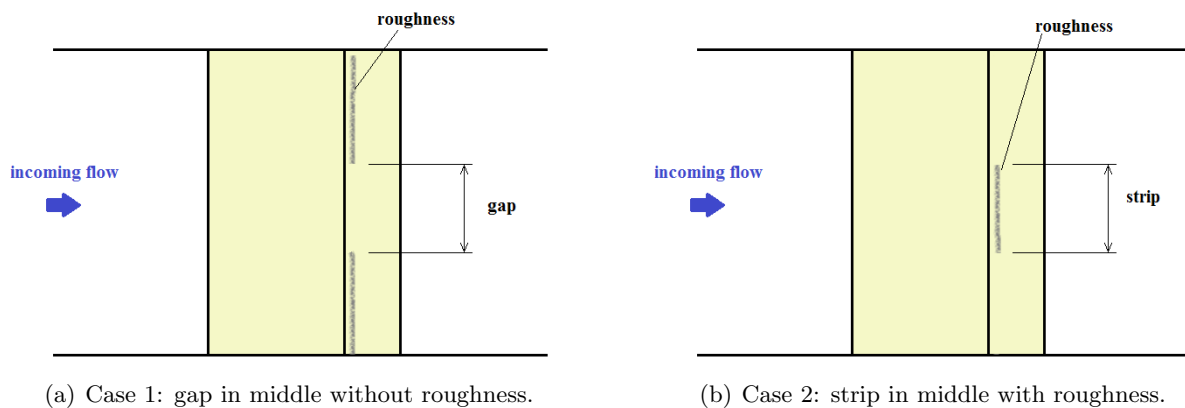
Figure 5.8: Schematic of side view LTT with roughness on the flap.

The results of these two cases in terms of C_l are shown in Figure 5.9 and Figure 5.10 for respectively different gap length and different strip length. As mentioned in previous chapters the span of this model is 1.25m, thus the "entire LER" C_l-curve refers to a roughness length of 1.25m. In both cases roughness lengths are tested from totally clean to full spanned roughness (or vice versa) with an overall step size of 10cm and some small jumps from 30 to 50cm and from 100 to 125cm.

In the linear region ahead of stall, Figure 5.9 shows a gradual increase in lift as the gap is increased (upwards movement of the lift curves). For example "entire LER" delivers 36% less lift with respect

to the clean flap configuration, for 50cm gap length ΔC_l = -12% and for 100cm gap length ΔC_l = -4%. Thus even at very large gap lengths C_l is still not within the threshold of 1% mentioned before.

In the strip-case, the limit is much more visible. The following results are calculated with respect to the "entire LER" instead of the clean configuration, as explained in 2: for 10cm strip length ΔC_l = 34%, for 50cm strip length ΔC_l = 10% and for 100cm strip length ΔC_l = 0.5%. Note again that these Δ's are only valid within the linear regime and not near or beyond $C_{l,max}$.

In conclusion, the second case suggests that the "actuator" length should be at least 100cm long, overlapping as good as the whole model span, to achieve a C_l within an acceptable threshold of 1% compared to a full spanned actuator. This of course is not the conclusion we hoped for, as we desired to have the smallest actuator as possible to be able to control and concentrate the inputted energy effectively while still minimizing three-dimensional flow effects.
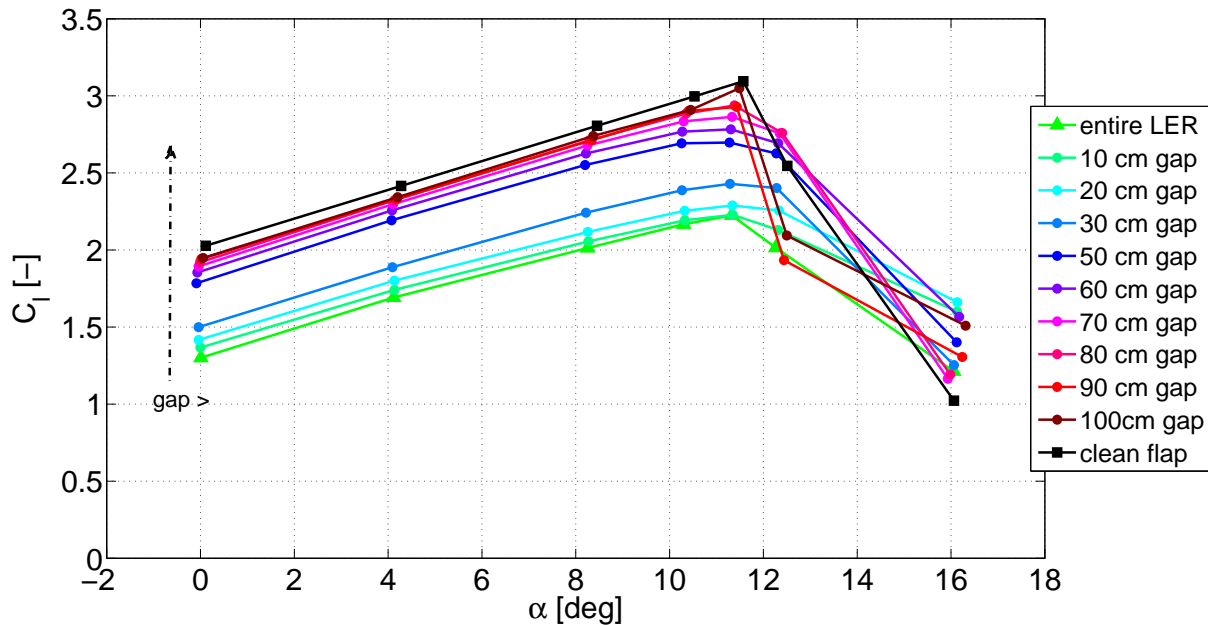
Figure 5.9: C_l versus α curves for different gap length for $\delta_f = 45°$, $x_{overlap} = 0\%c$, $y_{gap} = 3.5\%c$ and $Re = 1.7 \cdot 10^6$.
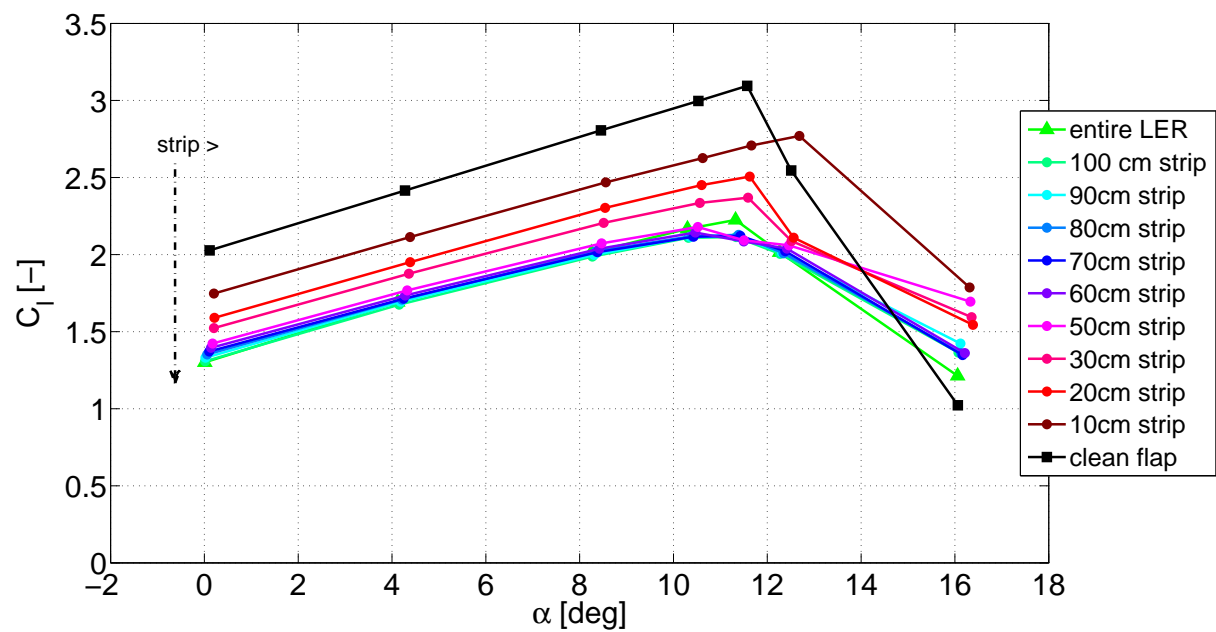
Figure 5.10: C_l versus α curves for different strip length for $\delta_f = 45°$, $x_{overlap} = 0\%c$, $y_{gap} = 3.5\%c$ and $Re = 1.7 \cdot 10^6$.

5.5   Plasma actuators

The original goal is to investigate plasma actuator effectiveness at critical circumstances: high flap deflection angle and high Reynolds number. Therefore, this simply requires the strongest plasma actuator possible. It turned out that an extensively parametric study to achieve this was too optimistic since effects from the model negatively influenced the plasma actuator working as well as difficulties with the flow data acquisition.

To clarify this, the experimental results are mainly based on pressure measurements along the airfoils surface. The focus of improvement is on the flap where a total of 28 pressure orifices were located and equally distributed along the lower and upper surface. Placing an actuator on the flap means that some orifices are directly covered by the electrodes and thus lack of data at these points. As an additional drawback it turned out that the orifices are made of small metal tubes which led to actuator discharge at these locations. To prevent or minimize efficiency losses, extra precautions had to be taken by:

- Protection of the model by a long strip of dielectric layer underneath the actuator.

- Additional coverage of orifices which were to close to the electrodes by 1×1cm pieces of dielectric.

- The high voltage electrode should be led along the lower half of the model since the pressure tubes are led beneath the skin of the upper half of the model. Leading the high voltage electrode along the upper half leads to small discrete discharges due to the metal tubes beneath the skin.

However, if necessary due to an actuator configuration the last point could be resolved by separating the lower electrode from the surface with a dielectric. Some precautions are illustrated in Figure 5.11.

More in this section a discussion of the operation and setup of the AC and NS DBD plasma actuators. After this, attention will be paid to the results of each actuator.

5.5.1   AC DBD plasma actuator

Description

The AC DBD actuator consist of 60μm thin rectangular copper electrodes made out of self-adhesive copper tape. In upcoming results only the effective spanwise length is mentioned along which plasma is generated, while in reality the electrodes are made longer because of connection issues. A dielectric layer (for these experiments Kapton is used) separates the upper electrode from the lower one. Tests are carried out with one to three Kapton tape layers. To prevent that the actuators discharge with the model itself, the surface is locally insulated by one Kapton layer before placing an actuator. The thickness of one such layer measures 2mil (1mil = 25.4μm).

The upper electrode is connected to the HV output cable of a TREK 20/20C HV amplifier ($\pm$ 20kV, $\pm$ 20mA, 1000W) while the lower electrode is connected to a grounded cable. In Figure 5.12 one can see how this generator is positioned in the LTT. To minimize any loss in energy due to interconnections the isolated HV cable should be as close as possible to the actuator. For this reason the cable is brought into the tunnel. However, bringing this cable in means that the tunnel flow is

Figure 5.11: Some precautions for the actuator. Left: a dark rectangular area were multiple layers of dielectric are placed to prevent discharge with the metal orifice. Also some orifices could be uncovered to acquire more data. Right: prevention of discharge at the flap lower side where the high voltage connection was led.

being disturbed by its presence. The degree of disturbance is not exactly studied and therefore can not be quantified. There were a couple of reasons why this cable is not aligned in the least disruptive way along the wings lower surface i.e. along the connection of the model with the turntable:

1. Boundary layer suction was applied around the model to prevent early separation near the tunnel walls. Placing the cable at this position would prevent the suction being applied properly.

2. The end plates are of metal thus in order to prevent conduction with the surroundings the HV cable should be kept far away from any conductive materials. Besides the fact that this is a potential factor of energy loss it is also a safety requirement.

3. Another safety measure is that the HV cable should be kept away from any grounded connections. Since the ground itself is not dangerous, this was led over the metal end plates instead of the HV cable to reach the actuators position.

This list of reasons resulted in the configuration as found in Figure 5.13. The HV cable was brought into the tunnel in a wide half circel, following the turntables' edge, until flap's position where it is further connected with coper tapes. Control of the actuator operation is finally done remotely via a computer workstation. Through a software program, called LabView, the driving signal can be created which is sent to the amplifier via a Digital/Analog (D/A) converter. Internal measurement probes of this amplifier provides direct readings of the output voltage and current.

Figure 5.12: The TREK 20/20C HV amplifier placement in the LTT.

grounded connection   HV cable
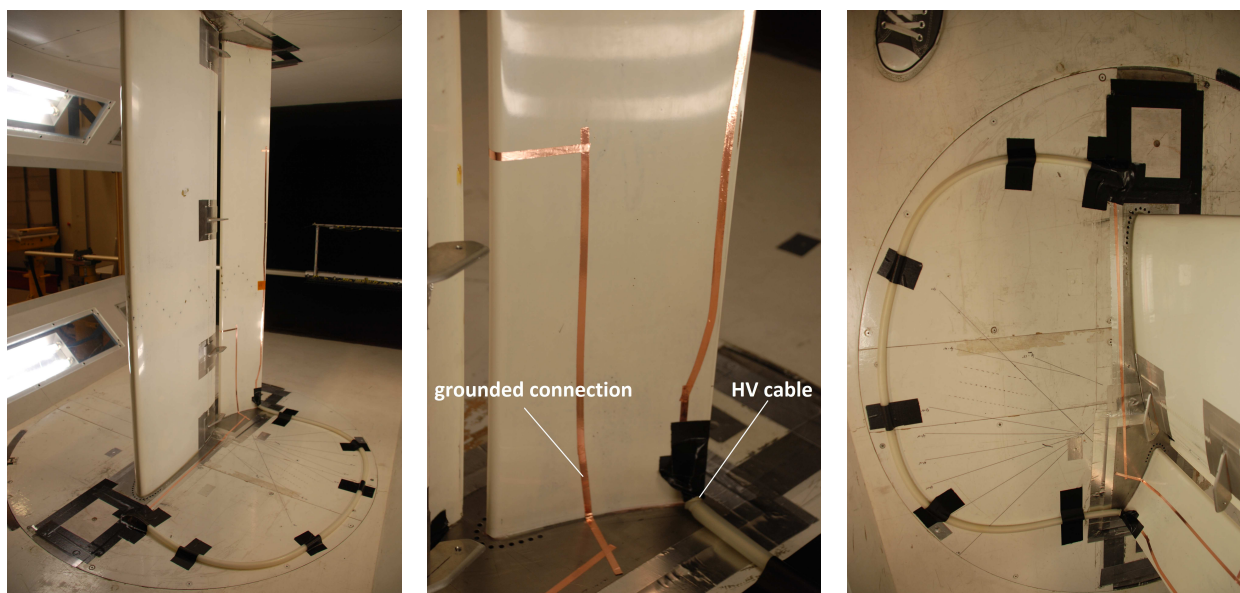
Figure 5.13: AC DBD actuator setup in the LTT.

Results

Previous results on the length of roughness, see Section 5.4, showed in a hypothetical way that an actuator should span at least 80% of the total flap length i.e. at least 100cm span length of the total 125cm. Alongside this, it is also hypothesized that the longer the actuator length, the lower the discharge energy density per span centimeter. A to long actuator could therefore be at the expense of any macroscopic effect. To determine the right balance, numerous experiments were conducted in advance with different plasma settings and configurations. Note that in all cases the intention was to get the actuator working at maximum accessible settings in terms of applied voltage and carrier frequency to produce the greatest body force i.e. induced velocity [12][35]. The range of some analyzed major parameters are listed below:

- actuator length 20∼100cm

- applied voltage 20∼30kV

- carrier frequency 600∼800Hz

- actuator position w.r.t. transition

- tunnel speed 10∼40m/s

Any effects in these experiments were quantified by applying tufts visualization on the flap's upper surface. The reason that an external parameter (i.e. tunnel speed) is added is to seek for possible limits in macroscopic effects due to tunnel running speed.

However remarkable enough, in none of these cases the AC DBD plasma actuator succeeded in showing any macroscopic effects when using tuft visualization. Even not at very low velocities up to $10m/s$. Of course tufts are not the ideal means for flow visualization since they are a source of disturbance which could reduce any (minimal) improvement due to the actuators. Thus clean airfoil pressure measurements with only an actuator "doing its job" should give more insight.

To continue the research, the preliminary parametric resulted in the adoption of some constant parameters listed in Table 5.1. Some of those were predefined due to material requirements (i.e. insulating, conductive), other due to material manufacturing (i.e. t_u, t_l, t_d). It was also decided to take a constant actuator length of 50cm because: 1) to increase the energy density distribution of the discharge e.g. a 100cm long actuator would have a relatively low discharge energy density, and 2) to preserve as much as possible the two-dimensionality of the flow e.g. a 20cm long actuator would possible introduce significantly more three-dimensional effects.

The actuator was then positioned in such a way that the diagonal located pressure gauges were completely within the by-actuator-manipulated flow field. Nevertheless this setup might still introduce three-dimensional flow behaviour resulting in a redistribution of the pressure in spanwise direction. As a consequence a lower pressure value is expected to be measured which automatically affects C_l and C_d since these are calculated from the measured C_p distribution.

The results for the AC DBD plasma actuator will be presented by showing the actuator in "on" and "off" mode for a range of angles of attack for two different cases at $Re = 1.7 \cdot 10^6$, see Table 5.2. Basically these cases differ in the width used for the upper electrode. The actuator is then exposed to maximum achievable values for applied voltage and carrier frequency; this is mostly just before an actuator burns out locally. Note that these actuators are the strongest obtained ones in terms of voltage, frequency and discharge density among all other AC DBD actuators tested and

	parameter	value
Signals	voltage waveform	sine
	duty cycle D [%]	100
	pulsed frequency f_p [Hz]	0
Dimensions	length actuator l_{ac} [mm]	500
	width lower electrode w_l [mm]	25
	electrode thickness t_u, t_l [mm]	0.06
	dielectric thickness t_d [mil]	6
	horizontal gap g [mm]	0
Materials	electrode material	copper
	dielectric material	Kapton polyimide

Table 5.1: Constant parameters for the AC DBD plasma actuator.

Parameter	value case a	value case b
width upper electrode w_u [mm]	10	5
applied voltage V [kV_{pp}]	28	23
carrier frequency f_{ac} [Hz]	700	650

Table 5.2: AC DBD plasma actuator settings for case a and b.

therefore are chosen to illustrate any improvement. As an example the actuator setup for "case a" can be seen in Figure 5.14.

In Appendix Figure B.5 the C_p distributions with respect to the dimensionless chord are shown for "case a" in actuator on and off mode. Left diagram of Figure B.5(a) illustrates the pressure distribution along the main element and right diagram for the flap. A detail from the flap at actuator position is shown in Figure B.5(b) to see any differences more clearly.

As expected, the main element does not show any exciting happenings and is more or less identical to the baseline wing C_p-data. By increasing α the pressure gradient increases at the main element which leads to flow separation at this part somewhere between 12° and 16°. Furthermore when observing the flap diagram lack of data at certain points can be pinpointed due to the presence of the actuator. The flat horizontal line at around 90%c position is a direct consequence of the actuator closing of some pressure taps giving fault measurements at these locations. Also at the flap's lower surface a pressure tap is closed to prevent discharge with the high voltage connection (Figure 5.11 right), which can be linked to the sharp pressure line near the trailing edge. This number of incorrect datapoins will affect the lift calculations since those are based on the measured C_p and thus correction at these points could be considered by predicting the C_p development. However, this is not done as this will lead to an additional uncertainty factor in the results by possibly incorrectly predicting the actuator effect. More suitable is to look at Δ-improvements for each single case without any correction. Thus if the actuator would improve anything, a direct effect in C_p should be noticed behind the actuator between roughly 95%c and 105%c: the horizontal C_p-line in this region, which indicates separated flow, should get a positive gradient to indicate that the flow has been attached to some extent. However, taking a closer look at the flap's C_p distribution, it seems that the actuator does not show any effect at all. C_p distributions for the actuator in "on" and "off" condition for each single α overlap eachother and therefore suggests that the actuator is not able to improve anything. Even at higher α's when the flap is being relieved by the displacement
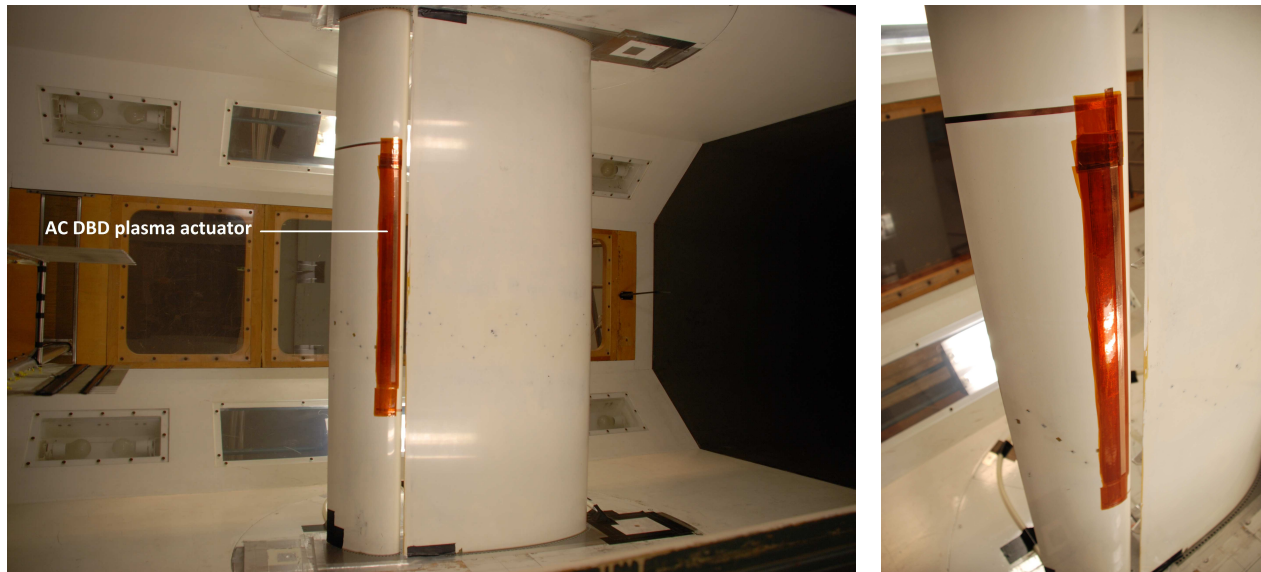
Figure 5.14: The AC DBD actuator from case a, located along the transition line of the flap.

effect of the main airfoil wake and thus less impuls is required to attach the flow, the actuator is still not capable to do so. In fact at 16°, the actuator "on" mode suggests to perform even worse than actuator "off". But as this difference is minimaal it could also be atrributed to measurement error instead of deterioration due to the actuator.

With this in mind the lift, drag and momentum polars in Figure 5.15 show not surprisingly almost similar results. The lift and momentum polar for the two conditions are completely overlapping. With respect to drag, small improvements are visible at $\alpha = 2°$, 4° and 11° and thus not continuously.

"Case b" C_p distributions are shown in Figure B.6 with the corresponding lift, drag and momentum polars in Figure 5.16. Remember that for this case a smaller upper electrode width size is used which allowed lower values of voltage and carrier frequency to be applied. The setup is also more optimized which enabled to uncover multiple pressure taps. Missing data has now been brought to the minimum, see also the detailed part of the pressure distributions.

As in previous case no improvements are visible. C_p distributions for the actuator in "on" and "off" condition for each α overlap eachother and the lift polar confirms this observation. The drag however seems to be increased if the actuator is turned on, but the shape and difference w.r.t. the off mode strongly gives the presumption that this is a measurement error.
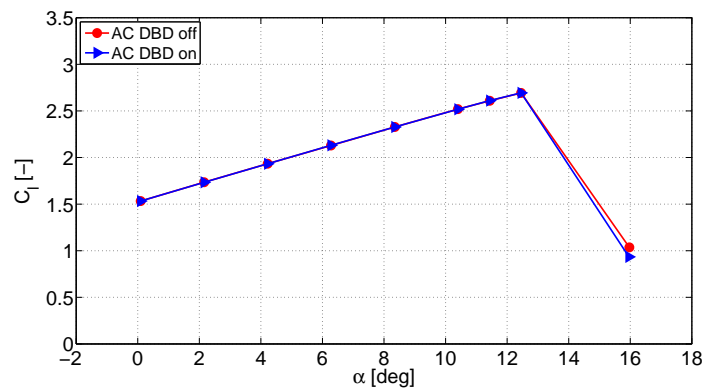
(a) C_l versus α.
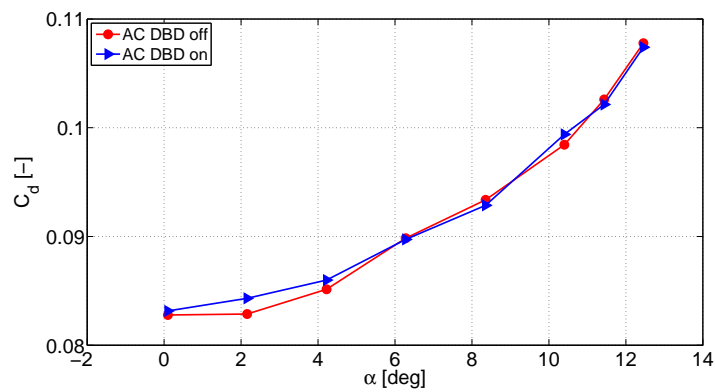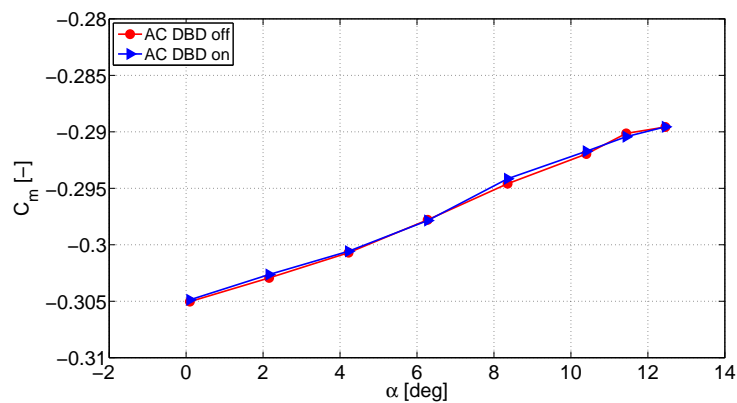
(b) C_d versus α.

(c) C_m versus α.

Figure 5.15: Case a: Effects of the AC DBD plasma actuator placed on the LE flap on the aerodynamic characteristics lift, drag and momentum for $\delta_f = 45°$ and $Re = 1.7 \cdot 10^6$.
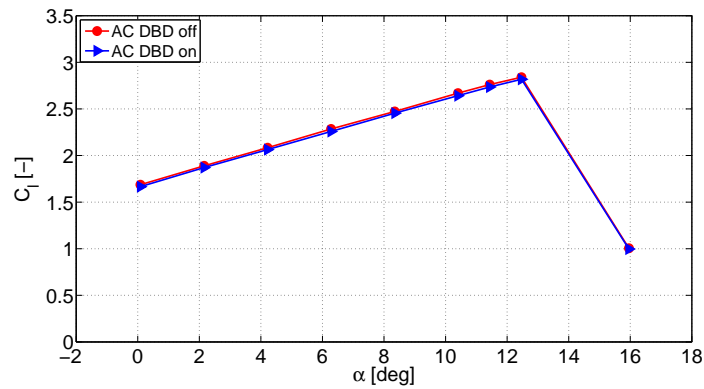
(a) C_l versus α.
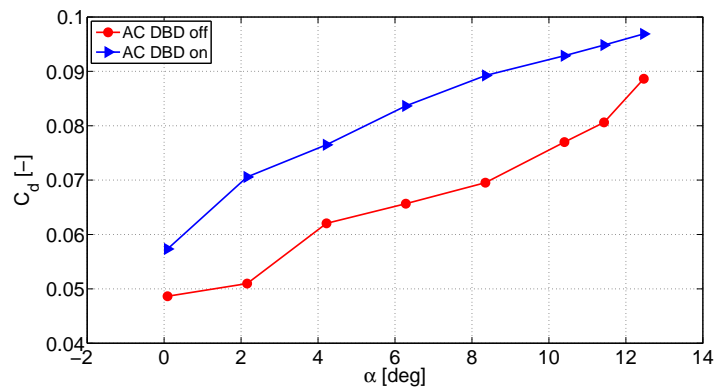
(b) C_d versus α.
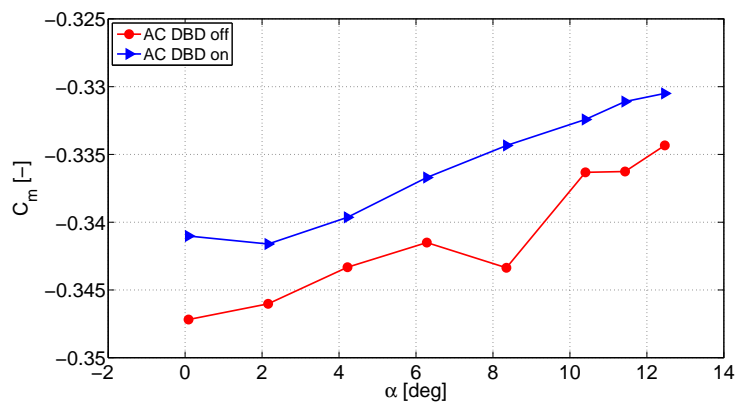
(c) C_m versus α.

Figure 5.16: Case b: Effects of the AC DBD plasma actuator placed on the LE flap on the aerodynamic characteristics lift, drag and momentum for $\delta_f = 45°$ and $Re = 1.7 \cdot 10^6$.

Besides the standard configuration of the AC DBD plasma actuator, the actuator can also be set up in such a way to function as a vortex generator for flow separation control (Figure 5.17). Literature [19] has shown that an actuator in this configuration produces vortices at free stream velocities up to $10m/s$. But the more important question remains whether the same can be achieved at higher velocities. The main difference with respect to the standard configuration is that now several, relatively short, actuators are aligned parallel to the flow (yaw angle $\beta = 90°$) so that they produce spanwise wall jets. Through interaction with the oncoming boundary layer, this creates streamwise longitudinal vortices. Hence, as additional test for the AC DBD actuator two approaches are investigated for the DBD-VG: co-rotating (CoR) and counter-rotating (CtR) vortex arrays.
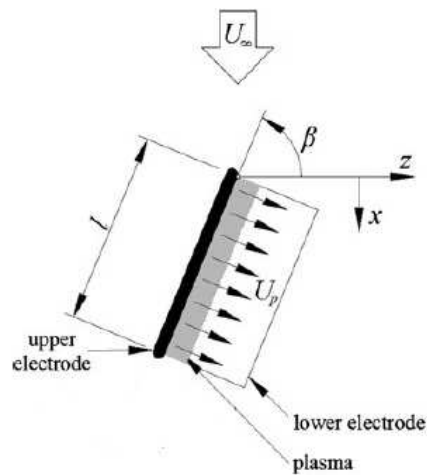
Figure 5.17: Schematic of DBD-VG [19].

Unfortunately exact results from the DBD-VG are not available since this setup covers almost 75% of the pressure taps on the flap's upper surface. Also tuft visualization did not show any effect but one must note that this wasn't the most suitable means; alternatively experimental setup was required (e.g. PIV) to visualize and analyze the DBD-VG effect. In Figure 5.18 one can see how the actuators were placed on the flap.
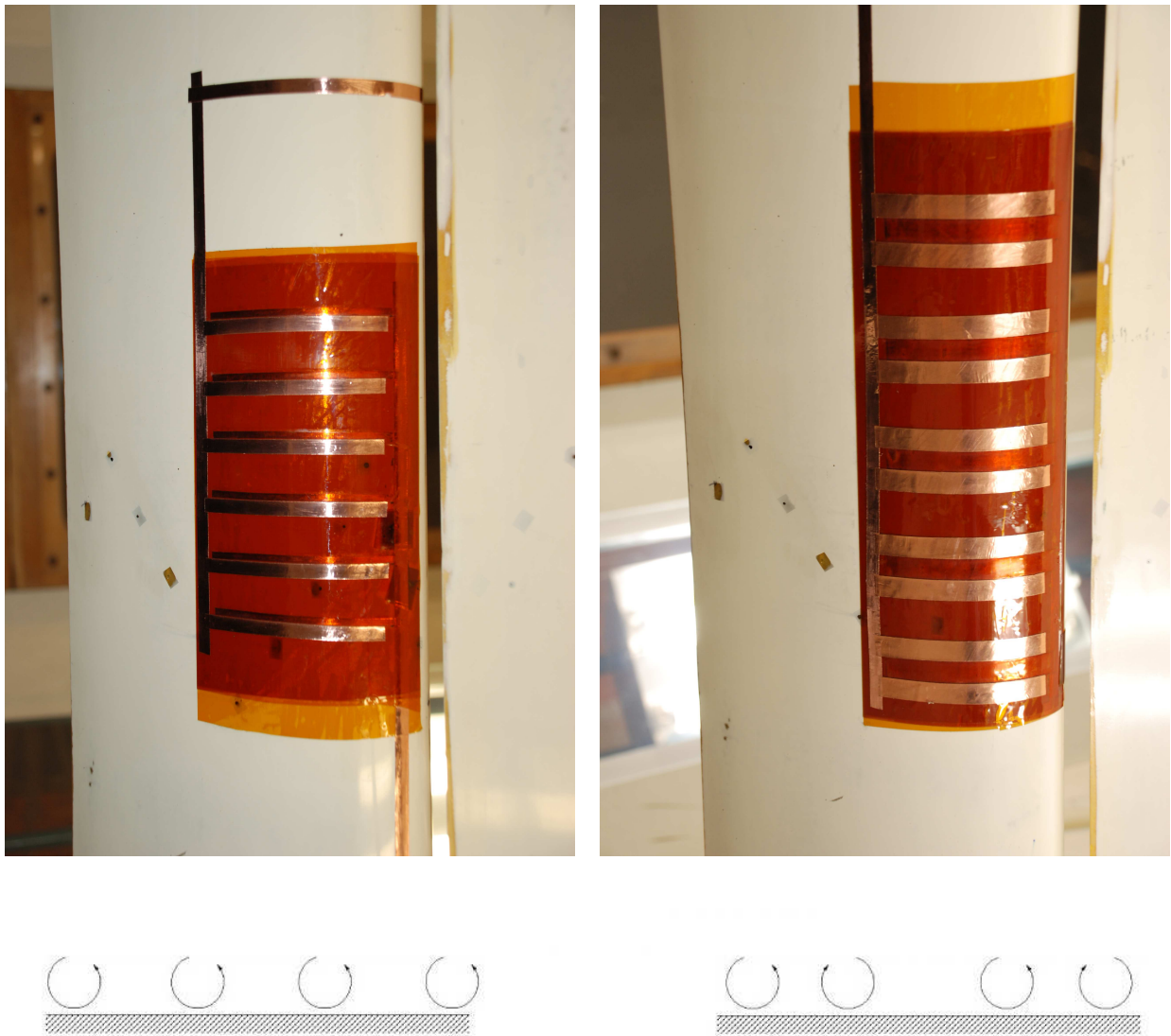
Figure 5.18: DBD-VG applied on flap for co-rotating vortex arrays (l) and for counter-rotating vortex arrays (r).

5.5.2   NS DBD plasma actuator

Description

Basically the setup of the NS DBD actuator is the same as for the AC DBD actuator. Again a 60μm thin, self-adhesive copper tape is used to make the rectangular copper electrodes. However, the width of this tape is much smaller (3mm), since previous studies by [6] demonstrated favorable properties for this width size. Furthermore, a 2mil thick Kapton layer is used as dielectric to separate the upper and lower electrode and to insulate the model locally.

The biggest difference in setup is that the NS DBD actuator requires its own special equipment to control and to power the actuator. A HV-coaxial cable, with an impedance of 100Ω, connects the actuator with the output of a nanosecond pulse solid-state generator. This generator can produce pulses up to 10kV with a rising time of 3ns and length of 15ns at repetition frequencies up to 10kHz. Instead of a computer workstation a Tektronix AFG function generator is used for building the input pulse and to remotely control the actuator. The two devices are shown in Figure 5.19.
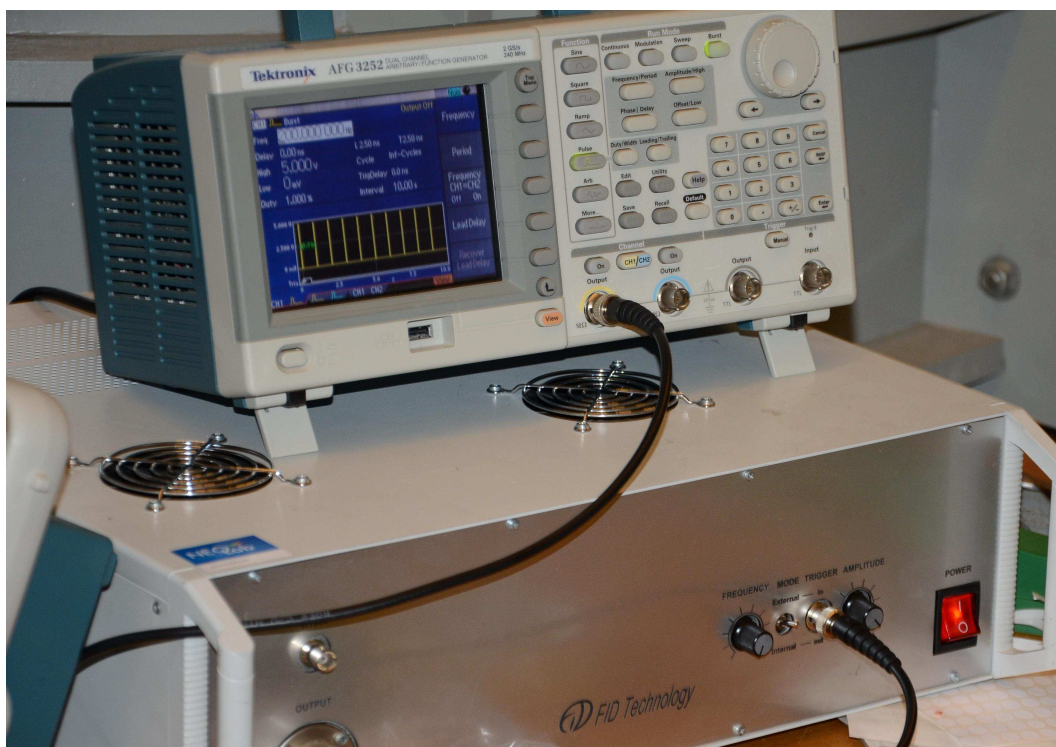
Figure 5.19: Top device: Tektronix AFG 3252 function generator. Bottom device: FID solid-state power generator [6].

There was however a practical problem due to the HV-coaxial cable: it was way to short to connect with the actuator if the same path into the tunnel was followed as the HV cable of the AC DBD actuator. Fortunately a small gap was found at the lower end plate near the TE of the main wing's upper surface. This was the ideal position to get the coaxial cable into the tunnel without any major adjustments. Finally, the already built-in ground connection is also used for the NS DBD actuator. In Figure 5.20 the two connections are shown in their final setup.
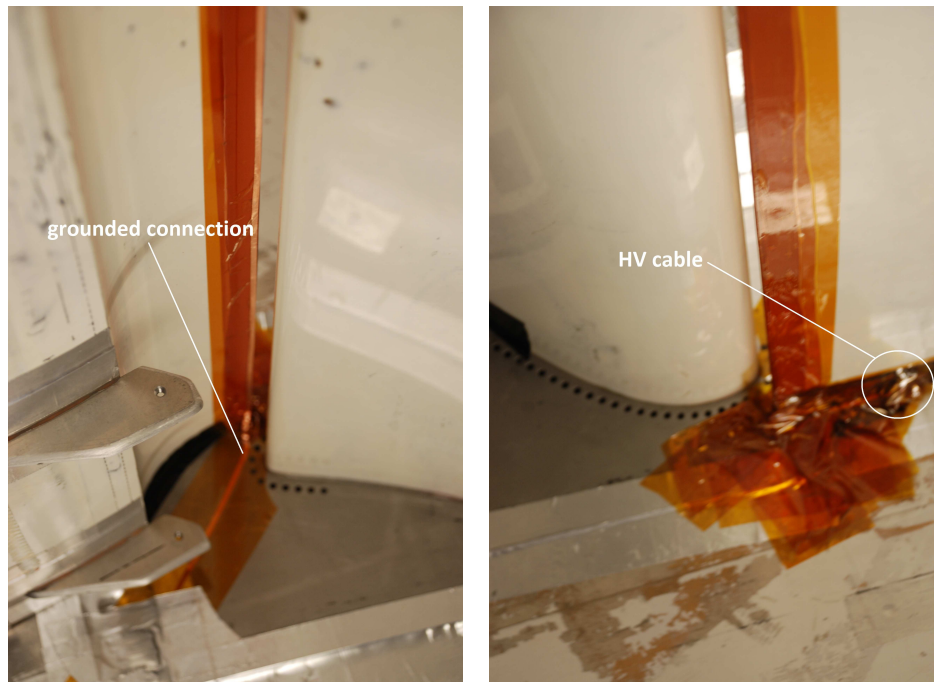
Figure 5.20: NS DBD actuator setup in the LTT: ground connection (l), high voltage connection (r).

Results

Following a similar approach as for the AC actuator, this actuator was also tested for different configurations while holding in mind the proposed minimum actuator length, the flow dimensionality and the energy density of discharge. Basically, the actuator should be strong enough to withstand against the critical flow conditions on the flap. For this reason the actuators are all driven by the maximum power the generator can deliver i.e. 10kV. First off, the effect of the actuator is investigated using tuft visualization by varying the following parameters:

- actuator length 20∼100cm

- actuator position w.r.t. transition

- tunnel speed 10∼40m/s

Since no visible flow reattachment on the flap could be observed, the amount of parameters to investigate were reduced by adopting the constants listed in Table 5.3; some were already predefined. A constant actuator length of 100cm was chosen as it was hypothesized that the generator was strong enough to power this length and furthermore the small electrode width size worked in its favor. The actuator started then from the bottom of the model (ground surface tunnel) and spanned the diagonal located pressure gauges completely. Still, lower values of pressure might be measured due to the non-mirrored setup of the actuator which could affect the two-dimensionality of the flow. Though deterioration of the pressure distribution due to this fact is expected to be of minimum order of magnitude.

The results for the NS DBD plasma actuator will be presented by showing the actuator in "off" and "on" mode for four different cases, see Table 5.4. Results are shown for three typically angles

	parameter	value
Signals	applied voltage V [kV]	10
	duty cycle D [%]	-
Dimensions	length actuator l_{ac} [mm]	1000
	width upper/lower electrode w_u, w_l [mm]	3
	electrode thickness t_u, t_l [mm]	0.06
	dielectric thickness t_d [mil]	6
	horizontal gap g [mm]	0
Materials	electrode material	copper
	dielectric material	Kapton polyimide

Table 5.3: Constant parameters for the NS DBD plasma actuator.

of attack, i.e. $\alpha = 0°$, $\alpha = 5°$ and $\alpha = 10°$, at three different velocities i.e. $V = 20m/s$, $V = 30m/s$ and $V = 42m/s$ ($Re = 0.85 \cdot 10^6$, $Re = 1.27 \cdot 10^6$ and $Re = 1.70 \cdot 10^6$ respectively). The tested cases can basically be divided into the normal discharge and the burst mode discharge of the actuator. Latter one is here introduced as an alternatively discharge type where instead of using a single pulse the burst mode gives bursts containing several pulses, each time the input was given. This method was capable of putting more energy into the flow even without increasing the energy of one single pulse. A schematic of the burst mode discharge can be found in Figure 5.21. Other investigated parameters are overall- and burst frequency. As remark to the four test cases, the inputted energy increases for increasing case number and thus a more powerful actuator is obtained.

case	signal type	overall frequency f_o [Hz]	burst frequency f_b [kHz]
1	normal discharge	50	-
2	normal discharge	200	-
3	burst mode	50	3.3
4	burst mode	200	3.3

Table 5.4: NS DBD plasma actuator settings for different cases.
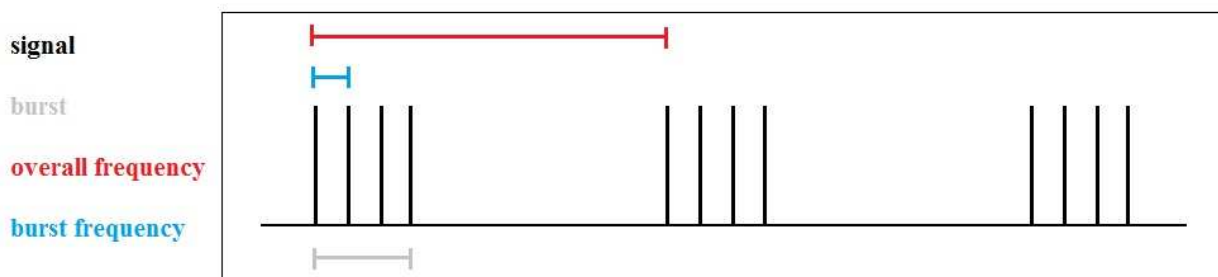
Figure 5.21: Schematic of burst mode discharge. Overall frequency: period between bursts. Burst frequency: period within a single burst.

One of the parameters is also the exact placement of the actuator. Literature [6][7] have shown that for one element airfoils the most effective position for the actuator is on the leading edge in case of leading edge separation. Now we are dealing with a two element airfoil, with more complicated flow separation behaviour and less knowledge of how to place the actuator. Therefore as a first test setup the decision was made, based on the working mechanism of the NS plasma actuator, to place

the actuator in front of the flap's transition point on a rather unusual position: the trailing edge of the main wing. This should give the actuator the opportunity to energize the flow well beyond the transition point, so that the created vortices are quite developed when reaching this point for an efficient transversal momentum transfer into the boundary layer. Regarding the actuator's setup, the covered high voltage electrode was led on the upper surface and the exposed ground on the lower surface of the main wing's trailing edge tip. In fact it doesn't matter which electrode is covered since the working mechanism is based on shock wave creation. In Figure 5.22 at the top one can see how the actuator is placed and at the bottom the blue glow discharge when the actuator is turned on.

In Figures 5.23, 5.24 and 5.25 one can see the lift, drag and momentum characteristics for respectively $V = 20m/s$, $V = 30m/s$ and $V = 42m/s$ for the different actuator modes. The corresponding C_p distributions can be found in Appendix Figures B.7-B.9, Figures B.10-B.12 and Figures B.13-B.15 respectively.

With respect to C_l, no lift increase could be perceived for none of the tested cases. The normal discharge, as well as the more powerful burst discharge do not show any significant improvement while literature [6][7][29] has proven its beneficial effect on separation delay, especially for increasing velocities. However data for latter fact are all on single element airfoils thus the application on two element airfoils obviously requires more application knowledge. Furthermore, the pressure distributions confirm this first observed fact; the flap's separated flow area remains unchanged at each V-α combination for each actuator mode. One can conclude that the NS DBD plasma actuator is not able to control separation for this specific configuration of a two element airfoil.

On the other hand the drag coefficient shows some odd behaviour. At $20m/s$ (Figure 5.23(b)) some fluctuations in the C_d-curves are noted for which the exact reason remains unknown but in all probability can be designated to measurement error. For higher velocities C_d shows a more gradual course. Further, it seems that at $42m/s$ the actuator disturbs the flow in a negative way which results in more drag w.r.t actuator off; the burst discharge "mode 4" shows in that respect the highest C_d values.

A possible cause for the non-successful test results for the proceeding experiments could be the strong vortex like movement of the stall cells. It is hypothesized that these stall cells might be to strong to be affected by the NS DBD plasma actuator for separation delay. Also, these cells cause flow separation on the flap which occurs in a non-straight line (see Figure 5.3). Therefore, as an additional experiment the effect of the NS actuator is analyzed when those stall cells are broken down and flap separation occurs more or less in a straight line. To achieve this a 60°, 0.85mm thick zigzag tape is placed on the flap's leading edge. A comparison will be made between a NS DBD plasma actuator (on mode 4) just in front of the flap's transition point and the combination of the same actuator with a zigzag tape on the LE (Figure 5.26).

In Figure 5.27 one can see the comparison between the two test cases along with the clean flap data. The "actuator + zigzag tape" yields less lift, more drag and a lower momentum coefficient with respect to the actuator only. Results are being overruled by the effect of the zigzag tape and therefore no improvement could be obtained when combining the two means. Furthermore, both tripping cases deteriorate the characteristics with respect to the clean configuration. It should be added that this deterioration can not be directly linked to the induced working mechanism of the actuator, but due to a more practical reason as was the case in previous experiments; 1) placement of the actuator covered certain pressure taps (less lift is measured), and 2) disturbance of the flow due to the addition of relief (more drag). For corresponding C_p distributions one is referred to Appendix Figure B.16 and Figure B.17.

Figure 5.22: The NS DBD plasma actuator for case 1-4.

(a) C_l versus α.

(b) C_d versus α.
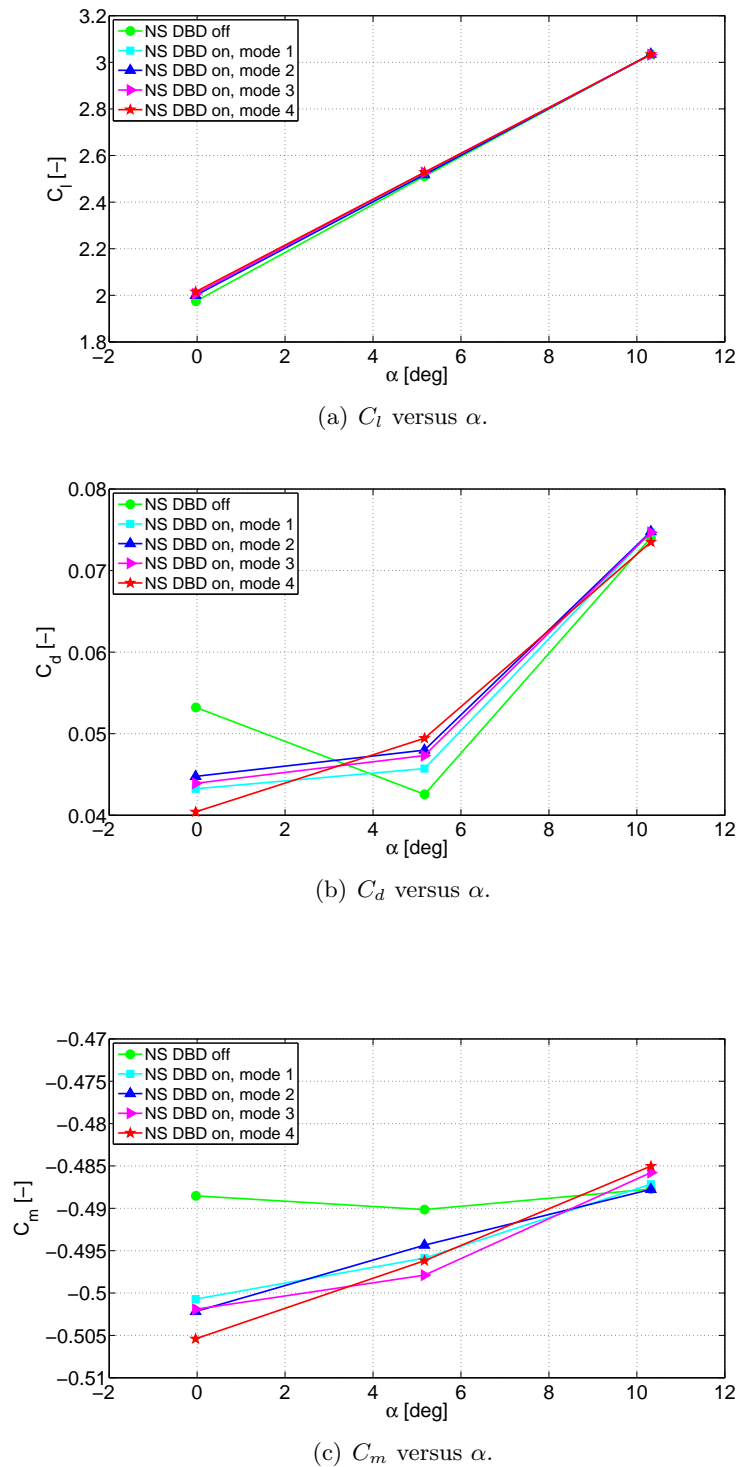
(c) C_m versus α.

Figure 5.23: Effects of the NS DBD plasma actuator placed on the TE of main wing on the aerodynamic characteristics lift, drag and momentum for $\delta_f = 45°$ and $Re = 0.85 \cdot 10^6$ ($V = 20m/s$).
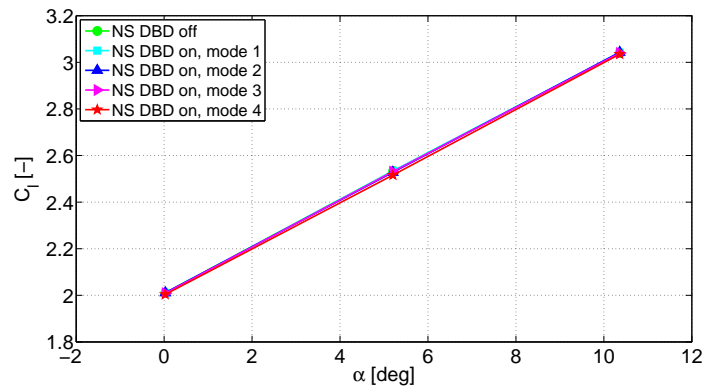
(a) C_l versus α.
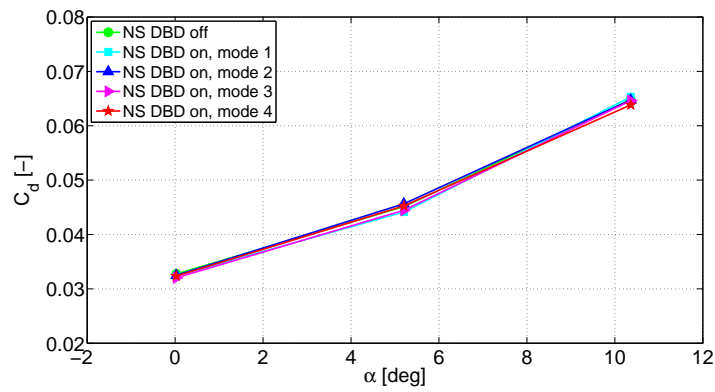
(b) C_d versus α.
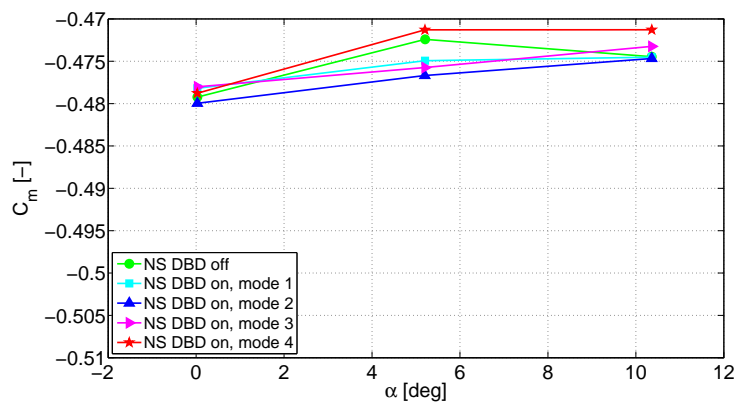
(c) C_m versus α.

Figure 5.24: Effects of the NS DBD plasma actuator placed on the TE of main wing on the aerodynamic characteristics lift, drag and momentum for $\delta_f = 45°$ and $Re = 1.27 \cdot 10^6$ ($V = 30m/s$).

(a) C_l versus α.

(b) C_d versus α.

(c) C_m versus α.
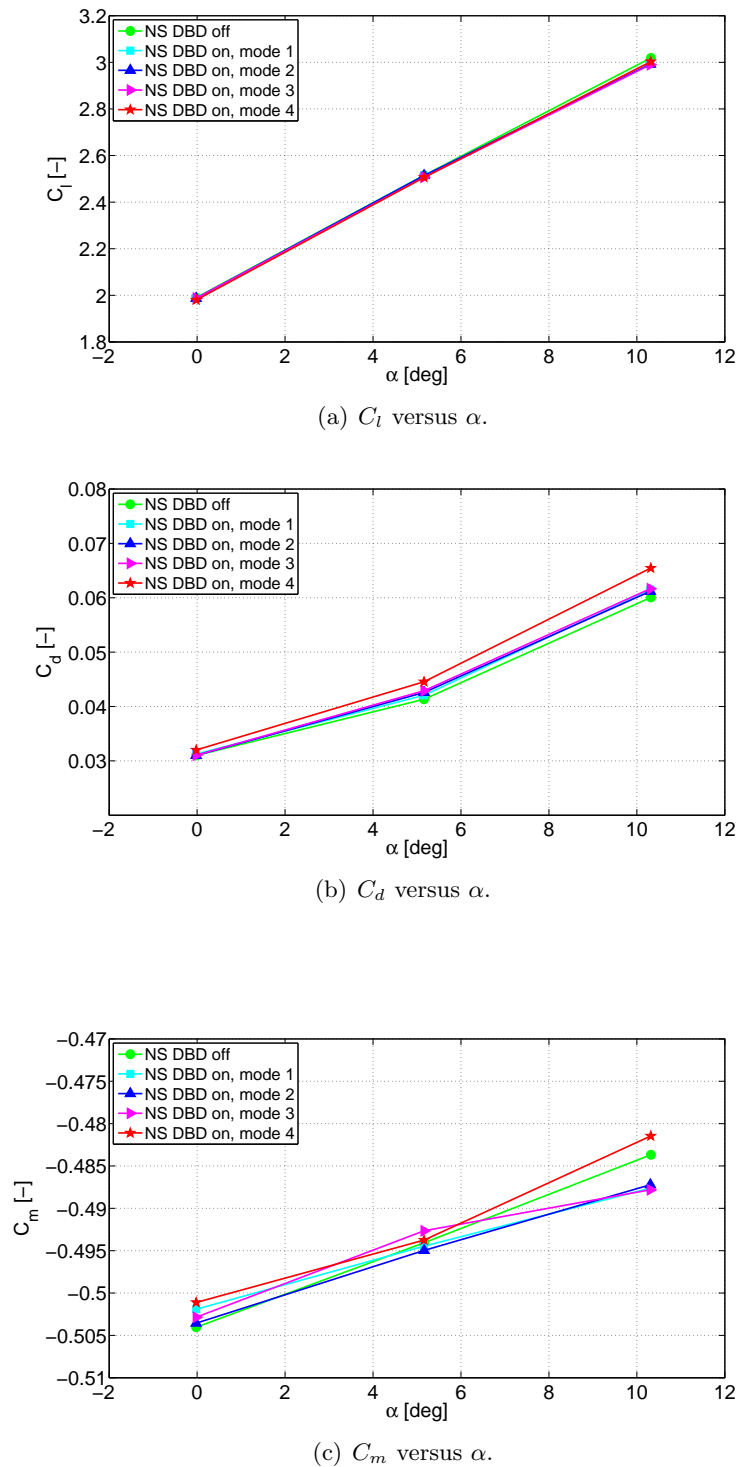
Figure 5.25: Effects of the NS DBD plasma actuator placed on the TE of main wing on the aerodynamic characteristics lift, drag and momentum for $\delta_f = 45°$ and $Re = 1.7 \cdot 10^6$ $(V = 42m/s)$.
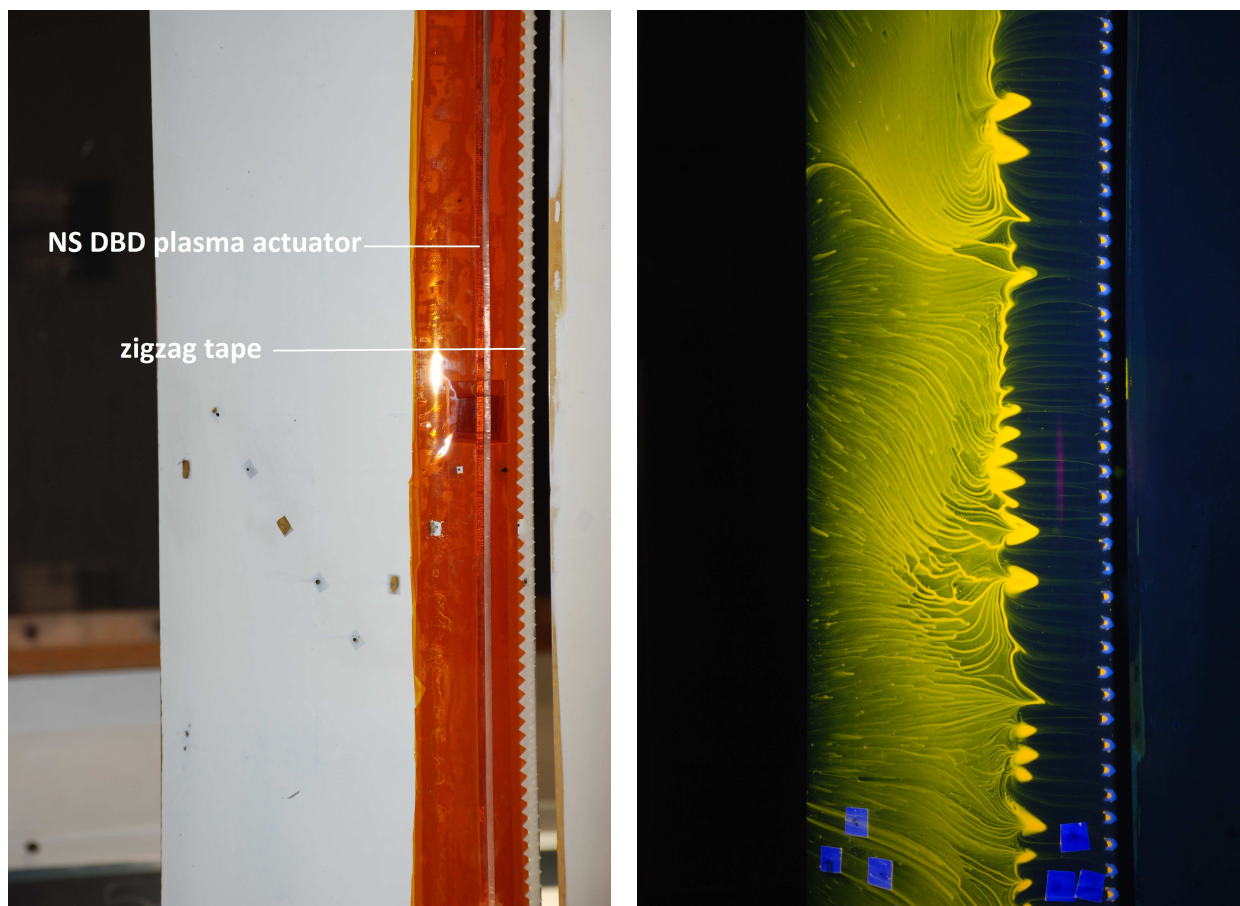
Figure 5.26: NS DBD plasma actuator + zigzag tape on flap (l), oil flow visualization with zigzag cuts on LE flap (r).
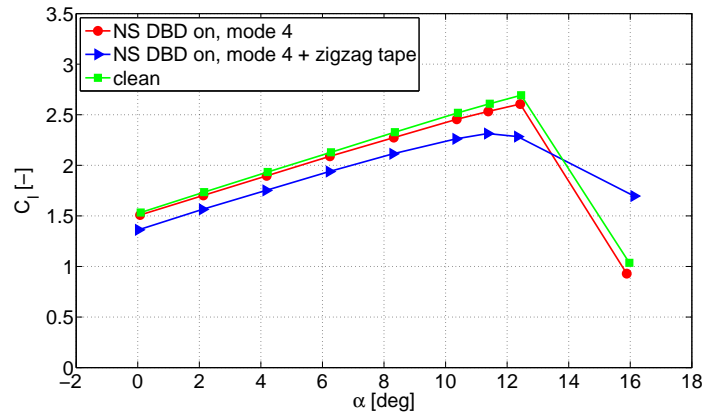
(a) C_l versus α.
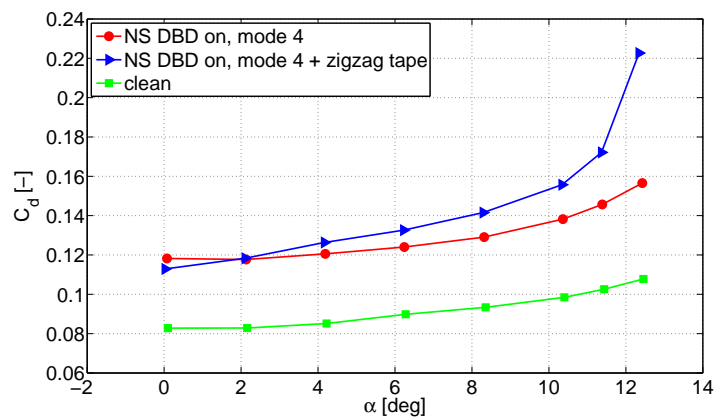
(b) C_d versus α.
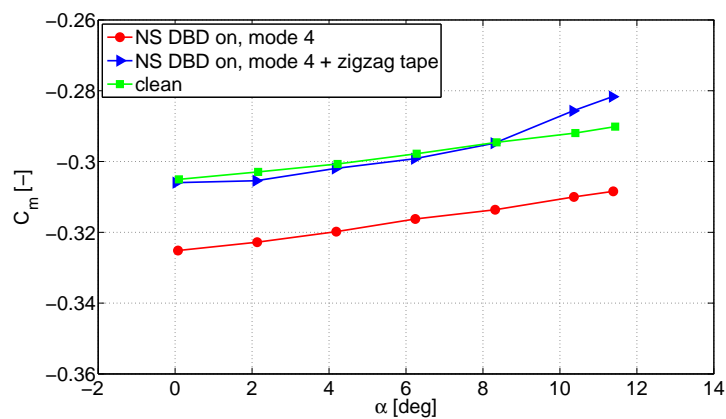
(c) C_m versus α.

Figure 5.27: Effects of the NS DBD plasma actuator placed on the LE flap on the aerodynamic characteristics lift, drag and momentum for $\delta_f = 45°$ and $Re = 1.7 \cdot 10^6$.

Chapter 6

MSES for maximum lift prediction

The passive and active flow control methods for separation delay investigated in the experimental part of this research did not succeed in gaining any lift improvement, as demonstrated in Chapter 5. It could be that a 45° flap angle causes a pressure gradient which is just to steep to overcome separation with control techniques. Then the question remains what the gain would be if flow reattachment over the entire wing was attained. A relatively simple and fast tool to answer this question is by the use of MSES.

MSES is a CFD design program for multi-element airfoils, developed at MIT University by Dr. M. Drela. It allows the user to calculate the maximum obtainable lift for ideal flow control i.e. Euler, this in comparison with (real life) viscous flow calculations. In this chapter MSES is used as a tool to analyze the lift performance of the NLF-MOD22 in different configurations. In the first section general information about MSES will be given, followed with the obtained numerical results thereafter.

6.1 Introduction to MSES (3.07)

MSES is originally distributed for all Unix platforms and for Linux. However, for this research a Windows-compatible MSES version had been used, made available by the Delft University of Technology. The aerodynamic theory behind the numerical simulation remains unchanged and therefore the Windows version of MSES should be identical to the original one except of the running platform. In the next section the theory will be discussed, followed by the user interface and the required input files to run a simulation.

6.1.1 Theory

The theory behind the numerical simulation of MSES can be divided into several topics. The following topics will be discussed briefly: 1) the flowfield related equations, 2) discretization and grid generation, 3) boundary layer equations to cover the viscous part of the flowfield and 4) the solving method.

Euler equations

MSES is an interactive program for the design, analysis and optimization of single- and multi-element airfoil sections in subsonic and transonic flow. It consists of a two-dimensional code based on the steady state conservative Euler equations [10].

Conservation of mass:

$$\oint_{\partial V} \rho(\vec{q} \cdot \hat{n}) ds = 0 \tag{6.1}$$

Conservation of momentum:

$$\oint_{\partial V} \rho(\vec{q} \cdot \hat{n})\vec{q} + p\hat{n} ds = 0 \tag{6.2}$$

Conservation of energy:

$$\oint_{\partial V} \rho(\vec{q} \cdot \hat{n})h_o ds = 0 \tag{6.3}$$

The integration is over the control volume boundary ∂V with unit normal $\hat{n}$. For the meaning of the remaining symbols in these conservation laws one is referred to the nomenclature.

The MSES code is set up by assuming that the viscous effects are restricted to a thin boundary layer and wake, and that the Euler equations cover the inviscid portion of the flowfield. Boundary layer theory describes the viscous part of the flow which is discussed later on in this section.

Grid generation

An intrinsic grid is used for the discretization of the equations in which one family of grid lines corresponds to the streamlines around the same body. Using this method the continuity equation 6.1 now simply states that the mass flux along each streamtube is constant:

$$m = \rho_1 q_1 A_{n1} = \rho_2 q_2 A_{n2} \tag{6.4}$$

Here A_n denotes the normal area of a conservation cell. Similarly the energy equation 6.3 reduces to a statement that the total enthalpy does not vary along a streamtube:

$$h_o = \frac{\gamma}{\gamma - 1}\frac{p_1}{\rho_1} + \frac{1}{2}q_1^2 = \frac{\gamma}{\gamma - 1}\frac{p_2}{\rho_2} + \frac{1}{2}q_2^2 \tag{6.5}$$

with γ the ratio of specific heats. Consequently the number of unknowns per grid node can now be reduced from four to two.

Boundary layer equations

The viscous portion of the flow is simulated by assuming that the effect of the boundary layer is to displace the inviscid flow away from the physical body to create a new *displacement body*. As long as the ratio of boundary layer thickness and streamline radius of curvature remains small this assumption has been shown to be acceptable. This is the case for a great deal of aerodynamic flows except e.g. near the trailing edge region. The boundary layer simulation starts with the Prandtl boundary layer equations [36]

Continuity:

$$\frac{\partial \rho}{\partial t} + \frac{\partial}{\partial x}(\rho u) + \frac{\partial}{\partial y}(\rho v) = 0 \tag{6.6}$$

Momentum:

$$\rho \left(\frac{\partial u}{\partial t} + u\frac{\partial u}{\partial x} + v\frac{\partial u}{\partial y} \right) = -\frac{\partial p_e}{\partial x} + \frac{\partial}{\partial y}\left(\mu \frac{\partial u}{\partial y} \right) \tag{6.7}$$

Energy:

$$\rho \left(\frac{\partial h}{\partial t} + u\frac{\partial h}{\partial x} + v\frac{\partial h}{\partial y} \right) = \frac{\partial p_e}{\partial t} + u\frac{\partial p_e}{\partial x} + \frac{\partial}{\partial y}\left(k\frac{\partial T}{\partial y} \right) + \mu \left(\frac{\partial u}{\partial y} \right)^2 \tag{6.8}$$

Assuming that we are dealing with a perfect gas and steady flows these equations reduce to

Continuity:

$$\frac{\partial}{\partial x}(\rho u) + \frac{\partial}{\partial y}(\rho v) = 0 \tag{6.9}$$

Momentum:

$$\rho u\frac{\partial u}{\partial x} + \rho v\frac{\partial u}{\partial y} = -\frac{\partial p_e}{\partial x} + \frac{\partial}{\partial y}\left(\mu \frac{\partial u}{\partial y} \right) \tag{6.10}$$

Energy:

$$\rho u\frac{\partial h}{\partial x} + \rho v\frac{\partial h}{\partial y} = u\frac{\partial p_e}{\partial x} + \frac{\partial}{\partial y}\left(\frac{\mu}{Pr} \frac{\partial h}{\partial y} \right) + \mu \left(\frac{\partial u}{\partial y} \right)^2 \tag{6.11}$$

with the Prandtl number defined as $Pr = \mu c_p/k$.

Afterwards the velocity can be eliminated using the continuity equation 6.9 by substituting for v into 6.10 and 6.11. The momentum and energy equation are then integrated from the wall to infinity. By neglecting cross-stream pressure variation and considering adiabatic freestreams only, we end up with the final simplified equations for MSES:

$$\frac{d\theta}{d\xi} + (2 + H - M_e^2)\frac{\theta}{u_e}\frac{du_e}{d\xi} = \frac{C_f}{2} \tag{6.12}$$

$$\theta \frac{dH^*}{d\xi} + (2H^{**} + H^*(1 - H)) \frac{\theta}{u_e} \frac{du_e}{d\xi} = 2C_D - H^* \frac{C_f}{2} \tag{6.13}$$

These two equations for momentum and energy respectively - in this form, also referred to as the shape parameter equation - are valid for laminar and turbulent boundary layer regions as well as for wakes. As a final step the boundary layer calculation and the rest of the flow are coupled by making the solution at the edge of the boundary layer a boundary condition for the inviscid calculation. This finally encloses the whole system for performing viscous simulations.

Newton solution procedure

Finally the system of nonlinear equations is solved by using the Newton solving method. More information about this can be found in Appendix C.1.

6.1.2   User interface

MSES is part of a set of programs to design, analyze and optimize single- and multi-element airfoils. The basic programs required to run a simulation for this research will be discussed in this section together with the specific input files for each single program. For the latter, each has its own objective. For information about all other programs or extra background information about the topics discussed hereafter, one is referred to the MSES User's Guide [9].

Input file blade.xxx - grid domain and airfoil geometry

The blade.xxx input file is a coordinate file created by the user containing the name of the profile (optionally), the four grid-boundary locations and the airfoil coordinates. This file is used in the initialization program MSET and in the airfoil manipulating program AIRSET. The "xxx" is a variable extension defined by the user, and is generally used to distinguish the case being run. For a multi-element airfoil the individual elements are separated by a "999.0 999.0" line. The exact format of this input file can be found in Appendix C.

Input file mses.xxx - runtime parameters

The mses.xxx input file is the runtime-parameter file used by the solver programs MSES and MSIS. Also here, the variable extension "xxx" defines a particular case. In this file all the variables together with the corresponding constraints are defined. It contains geometric and freestream flow data like the angle of attack, the Reynolds number and the Mach number. The user can define the kind of simulation by a selection of several parameters e.g. inviscid flow, fully isentropic or a combination of isentropic and dissipative. More information about the format of this input file can be found in Appendix C.

Airfoil geometry manipulating program AIRSET

AIRSET is a menu-driven program for manipulating multi-element airfoil configurations and reads blade.xxx or a combination of several blade.xxx files as input. AIRSET permits actions such as splitting off a flap and modifying the contour of a profile using the screen cursor. Furthermore,

element translation, rotation or scaling can readily be performed with immediate graphical feedback. An inviscid panel method, with compressibility correction, is provided for a quick sanity check on any modification.

Grid and flowfield initialization program MSET

MSET is the program used to initialize the grid, the flowfield and a variety of other variables. It reads the airfoil coordinate input file blade.xxx and the gridpar.xxx file if available (optionally). MSET is menu-driven and allows the user to iteratively generate a good initial grid. By specifying the angle of attack a panel solution is generated which is used to trace a pair of stagnation streamlines just above and below each element, as well as the upper and lower farfield streamlines. Once a good node distribution on each element is obtained, MSET proceeds to modify all the spacings to resolve conflicts between adjacent elements. An elliptic grid smoother can be used in order to eliminate grid imperfections such as kinks, overlaps and to make the grid streamlines correspond to those of the incompressible inviscid flow. This final grid then serves as an initial guess for the MSES solver.

Flow solver program MSES

MSES is the main program that solves the Euler equations. It requires two input files: mdat.xxx and mses.xxx. The output file is written back to mdat.xxx which means that mdat.xxx can either be a restart file from an old calculation or a file created by MSET. When starting MSES the user is asked for the number of iterations to be performed. This value serves as a limit since MSES will terminate earlier if the average changes of several parameters between two iterations drop below the convergence tolerance limits and the maximum changes drop below 10 times these limits.

Flow solver program MSIS

MSIS is functionally the same as MSES except that MSIS solves the Euler equations with one of the momentum equations replaced by an isentropic condition. Consequently, the Newton matrix used by MSIS is slightly changed which makes it about twice-four times as fast as MSES. Furthermore, MSIS is also advantageous as it can calculate flows with extremely low freestream Mach numbers ($M_\infty \cong 0.001$ or less). An important note is that MSIS can only be used for subcritical cases. If any part of the flowfield in the solution becomes supersonic, MSIS will fail.

Solution plotter MPLOT

MPLOT is the program which displays the solution in mdat.xxx at any time whether the solution is converged or not. It allows plotting of most of the airfoil's surface and wake boundary layer variables. Force coefficients and amplitude amplifications for transition prediction can also be shown.

6.2   Validation of Windows-MSES

Firstly, the Windows-MSES is validated using a simplified profile of the originally test model: the two elements of the NLF-MOD22 airfoil are fused by smoothly connecting the main and flap element. This results in the (solid) single element airfoil as shown in Figure 6.1. The reason of validation is to see if the conversion from UNIX to Windows platform, carried out by TU delft, is done correctly

before proceeding to multiple elements simulations. The results of the calculations performed with MSES are compared with results from another CFD program called XFOIL, and with experimental data from literature.

The experimental data is taken from Boermans and Rutten [4] who analyzed several test cases of the NLF-MOD22(A) and (B). In one of the test cases, with the flap in nested position, the gap on the lower surface of NLF-MOD22(A) was covered by an aluminum strip to prevent air flowing through the slot. This model can be assumed to be semi single element as the lower surface has one smooth surface, with still a small gap on the upper surface between the flap and main element. As no experimental data is available of the exact single element NLF-MOD22, data from the latter test case is a good approximation to compare with the numerical results. Both the experiment as the numerical calculations are conducted at cruise configuration Reynolds number of $3.0 \cdot 10^6$.
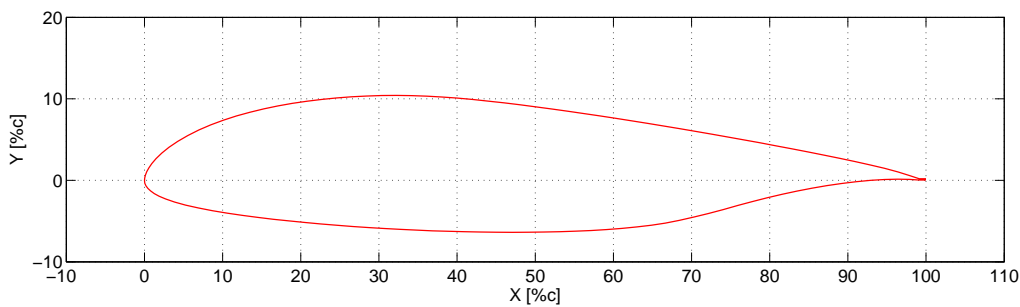
Figure 6.1: The NLF-MOD22 single element airfoil.

Simulations of the flowfield around the airfoil using XFOIL and MSES are carried out for a range of angles of attack starting at $-2°$ till $17°$. The experimental data however is limited to an angle of attack of $10°$. The focus is on the airfoil's characteristics lift and drag coefficient. Finally, the comparison of data is shown in Figure 6.2 presenting the following graphs: C_l versus α (Figure 6.2(a)), C_d versus α (Figure 6.2(b)), C_l versus C_d (Figure 6.2(c)), C_{dp} versus α (Figure 6.2(d)), C_{df} versus α (Figure 6.2(e)) and C_l versus x_{trtop} (Figure 6.2(f)). As a last note, the experimental data is limited to C_l and C_d only.

As one can see in all graphs, XFOIL and MSES results show great similarities. However, near the stall region at higher angles of attack, MSES predicts a slightly lower lift- and lower drag coefficient. Overall, the pressure drag increases with increasing α and is lower than the friction drag for $\alpha < 9°$. At higher α's the pressure drag overrules the friction drag. Furthermore, the transition point location predicted by both programs is identical.

With respect to the experimental data, the lift curve is very similar to that from XFOIL and MSES (up to stall) whereas a small discrepancy is noticeable in drag coefficient, see Figures 6.2(a), 6.2(b) and 6.2(c) respectively. This coefficient discrepancy can probably be attributed to the open slot entry on the model's upper surface, which disturbs the flow causing additional drag. It is hypothesized that if this gap was covered next to the already covered lower slot entry, a "single" element is created of the model and the drag would diminish reaching the same values as predicted by XFOIL and MSES.

As an additional check the experimentally measured pressure distributions are compared with those calculated by MSES for certain angles of attack (Figure 6.3). One can clearly see that the distributions are as good as identical e.g. at cruise condition ($\alpha \approx 0°$) both data show laminar flow up to $45\%c$ on the upper surface and $65\%c$ on the lower surface, with stall of the fast trailing edge type.

(a) C_l versus α.

(b) C_d versus α.

(c) C_l versus C_d.

(d) C_{dp} versus α.

(e) C_{df} versus α.

(f) C_l versus x_{trtop}.
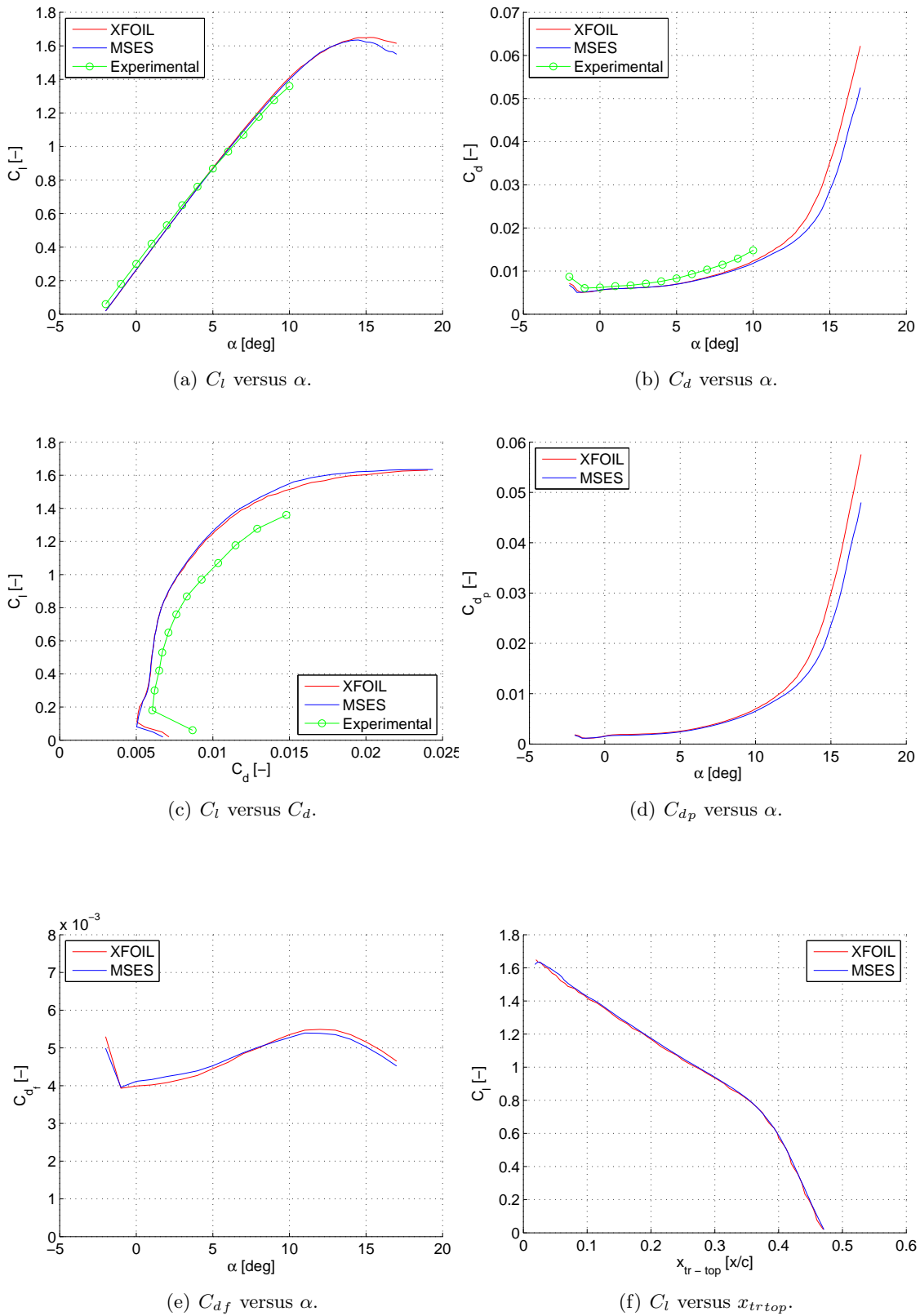
Figure 6.2: Comparison of XFOIL, MSES and experimantal data from Boermans [4] for single element NLF-MOD22 at $Re = 3.0 \cdot 10^6$.
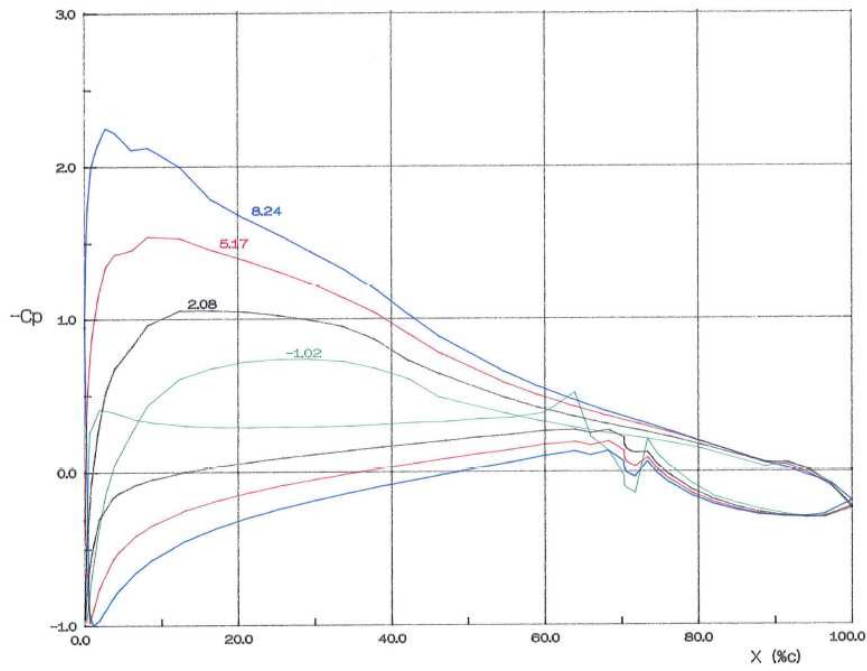
(a) Experimental data from [4].
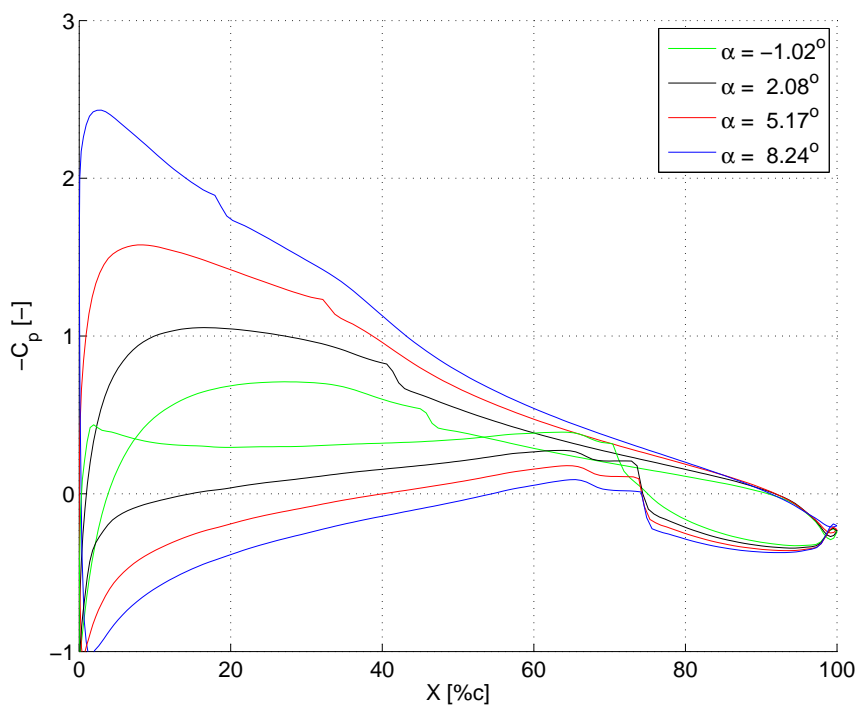
(b) Numerical data from MSES.

Figure 6.3: C_p distribution of single element NLF-MOD22 at $Re = 3.0 \cdot 10^6$, experimental and numerical data.

6.3   The NLF-MOD22(A) lifting limits

Since MSES encounters convergence problems when a model contains sharp edges, the profile used for the calculations is the NLF-MOD22(A) (see Figure 4.3 illustrated below again) instead of the experimental model NLF-MOD22(B) (Figure 4.4). The two models are mainly differentiated by a smooth and sharp slot entrance shape, model A and B respectively, which therefore makes model A more suitable for MSES simulations. Differences in performance between model A and B are demonstrated to be relatively small according to Boermans and Rutten [4] what makes the findings and conclusions in this section also valid for NLF-MOD22(B).

The profile will be investigated for a range of flap angles, with corresponding overlap and gap settings according to Table 6.1, to see how the maximum lift propagates with increasing δ_f. Important to add is that all the calculations are performed with the program MSIS, since the Mach number for the calculations is very low (0.123) and therefore isentropic conditions can be assumed. Consequently, the advantages of the use of this tool are twofold: 1) extremely fast convergence time and 2) the ease to calculate for larger α.
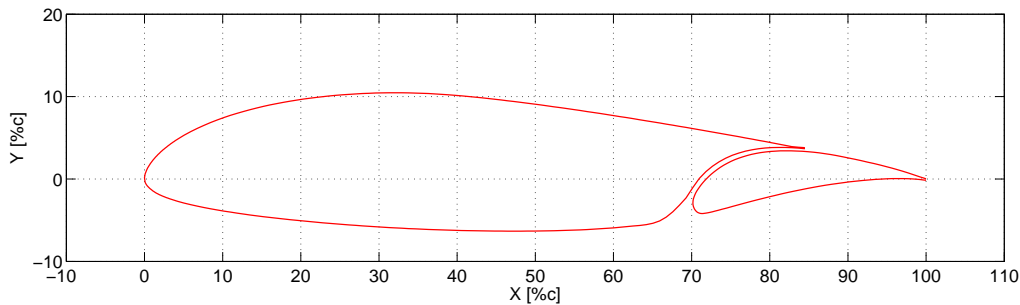
Figure 4.3: The NLF-MOD22(A) airfoil, showing the main element and the flap.

δ_f [°]	$x_{overlap}$ [%c]	y_{gap} [%c]
5	10.0	1.2
10	8.0	1.5
15	8.0	2.0
20	5.5	2.0
25	3.0	2.5
30	1.0	3.0
35	0.5	3.0
40	0.0	3.0
45	0.0	3.5

Table 6.1: Model flap position settings.

Results

The MSES results for the NLF-MOD22(A) are presented by analyzing four scenarios at different angles of attack i.e. $\alpha = 0°, 4°, 8°$ en $12°$ for both inviscid as viscous flow calculations ($Re = 1.7 \cdot 10^6$). The inviscid calculations are here assumed to represent the case for an ideal flow control over the complete wing by a non-specified mean; the viscous calculations however show the real life case. As a result, Figure 6.5 and 6.6 illustrate the lift polars as a function of the flap deflection angle. The

left side of the figures show the total lift graphs and on the right side the lift breakdown into main element and flap. Furthermore, it should be added that MSES experiences convergence problems for flap nested ($\delta_f = 0°$) calculations due to the small gap between the flap and the main element. For this reason, to complete the polars, lift data for flap nested positions are replaced by calculations using the single element NLF-MOD22.

Looking at the total lift curves in Figures 6.5 and 6.6 the inviscid potential flow calculations result in linearly increasing lift curves for increasing flap deflection angle, as expected. Basically a higher α results in an upwards swift of the lift curve, i.e. each 4° of α increase results in a net increase of $C_{l_{total}}$ with a factor of ~ 0.5 (Figure 6.5(a), 6.5(c), 6.6(a) and 6.6(c)). As mentioned before, these are the maximum achievable C_l's for ideal flow control (no separation) in terms of angle of attack and flap deflection angle. Important to notice is the difference in (vertical) scales between each α-case.

The next step is to see how the inviscid results compare with the viscous results and thus what the potential gain would be. Again, the focus is on $C_{l_{total}}$ and one can clearly observe an overall linear increase of the lift curves until $\delta_f = 20°$, with a slightly lower gradient compared with the inviscid calculations. Increasing this flap angle, for fixed $\alpha = 0°$, decreases the lift-gradient more and more reaching $\partial C_{l_{total}}/\partial \delta_f \approx 0$ at $\delta_f = 45°$ (Figure 6.5(a)). The same can be observed for higher angles of attack only data is now limited till 40° flap angle as MSES encounters convergence difficulties due to the high α-δ_f combinations; MSES can hardly predict large areas of separated flow.

So the overall trend is that the potential lift gain increases with increasing flap deflection angle. Hence, the question rises of how this potential is distributed over the two elements. The answer to this can be found on the right hand side of Figures 6.5 and 6.6. The main element's lift coefficient is to a large extent similar to that of $C_{l_{total}}$, only a factor lower, with $C_{l_{main}}$ reaching a limit as $\delta_f > 40°$. Looking at $C_{l_{flap}}$, the inviscid calculations show again a linearly increasing lift curve while the viscid calculations show a gradually decreasing lift gradient as $\delta_f > 15°$. One remarkable thing for $\alpha = 0°$, $\alpha = 4°$ and $\alpha = 8°$ (Figures 6.5(b), 6.5(d) and 6.6(b)) is that for $\delta_f < 15°$ the viscous calculations seem to predict a higher lift compared to the inviscid ones. This can be attributed to a beneficial viscous interaction between the two elements; streamlines reduce the effective gap space between the flap and the main element creating a local flow acceleration and a lift increase. This effect however diminishes for increasing α until it vanishes (Figure 6.6(d)).

To get a closer look of why the airfoil looses an increasing part of its potential lift at larger flap deflection angles, pressure distributions are to be consulted. An example C_p-distribution extracted from MSES is shown in Figure 6.7. On the lower part the airfoil is shown with the calculated streamlines. The corresponding pressure distribution is illustrated on the upper part of the figure. Note that different colors are used to distinguish the streamlines and to link them with the airfoil's surface pressure. As a result, the pressure distributions are summarized in Figures 6.8-6.15 showing distributions for

- $\alpha = 0°$ - inviscid/viscous

- $\alpha = 4°$ - inviscid/viscous

- $\alpha = 8°$ - inviscid/viscous

- $\alpha = 12°$ - inviscid/viscous

respectively. Here each color represents a certain flap deflection angle.

The inviscid cases show how the limit pressure distributions would look like in case of an ideal flow control. As the lift force can be deduced directly from C_p by integration, the previous found linear

lift curves are in line with the corresponding distributions i.e. a constant $\Delta \int C_p dy$ increase for both main element and flap for each $\Delta \delta_f = 5°$.

The viscous calculations show however some typical viscous effects. Starting at $\alpha = 0°$ and $\delta_f = 5°$ (Figure 6.9) a laminar separation bubble is visible at the suction side of the main element near $45\%c$. The flow gets turbulent after the bubble, but otherwise there is no separation of the flow yet. Also the bubble moves forward as δ_f is increased. A larger area becomes dominated by turbulent flow which is one of the reasons why the main element is characterized by a deflectng lift curve. On the pressure side of the main element some irregularities are visible near $65\%c$. This is however not a bubble since the inviscid calculations show the same local disturbance and furthermore its insensitive to any δ_f change. Thus this phenomenon is very likely an geometry effect caused by the airfoils curvature near the lower side slot entry. With respect to the flap, it is important to add that the distributions move to the right because of the flap configuration settings as listed in Table 6.1. Still at $\alpha = 0°$, the flow around the flap's pressure side is completely laminar at all δ_f. Continuing to the suction side, a strange pressure peak appears on the leading edge for all flap angles (and at all α). The peak is not visible in any of the inviscid calculations and thus not directly related to the airfoil's geometry. The only scenario remains that there is viscous interference effect between the first and second element. Viscous calculations with the flap only support this statement as the peak then disappears (Figure 6.16 and 6.17). The next important viscous effect on the suction side is the visual appearance of a laminar separation bubble starting somewhere between $\delta_f = 5°$ and $10°$ and moves forward for increasing δ_f. Also now a growing area is dominated by a yet attached turbulent flow until it starts to separate from the trailing edge after approximately $\delta_f = 20°$, indicated by the flat pressure distribution. From this point on, the flap loses more lift as noticed in the lift curve. As a consequence the positive influence on the circulation of the first element decreases which makes the lift of this element to increase less fast with increasing flap angle.

For higher α's the inviscid pressure distributions increase linearly. Viscous calculations show however a very sharp pressure peak rise on the leading edge of the main element, with e.g. at $\alpha = 12°$ the suction side is almost entirely dominated with turbulent flow and separation is very close to occur (Figure 6.15). In accordance with the experimental baseline data in Section 5.1, the increased α causes a positive interference of the main element on the flap: the viscous displacement effect of the main element's wake on the pressure distribution of the flap makes the flow to reattach completely on this element (the flat pressure distribution disappears). However the net lift force is relatively low for this part and the main element is close to stall, which is finally the reason for the stall of the complete system.

Thus in the context of flap leading edge applications on the NLF-MOD22(A) ideal flow control on the flap could theoretically increase the lift coefficient with up to 0.3 for low angles of attack, based on the following calculation: $\Delta C_{lf} = C_{lf,invisc.} - C_{lf,visc.}$. A graphical illustration for this is shown in Figure 6.18. Though this potential does not take into account the viscous flow interaction between main and flap element if this gain was achieved. However, to see if this potential gain can be achieved on the flap an additional experiment is conducted for pressure adaption. This will be discussed in the next section.
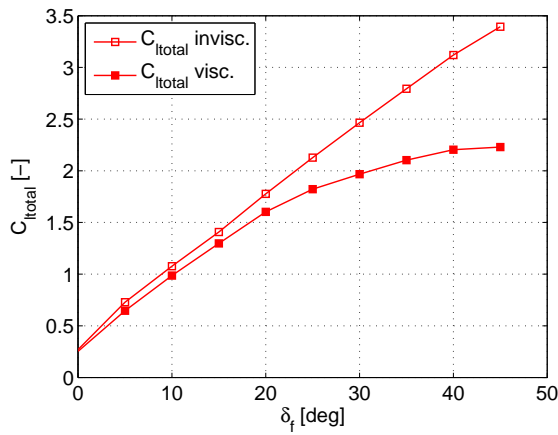
(a) C_{ltotal} versus δ_f at $\alpha = 0°$.
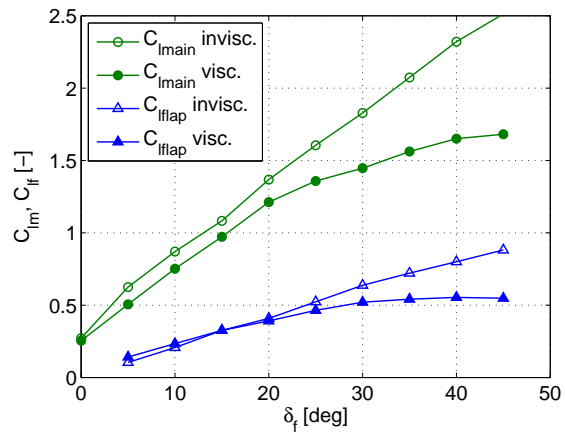
(b) C_{lmain} and C_{lflap} versus δ_f at $\alpha = 0°$.
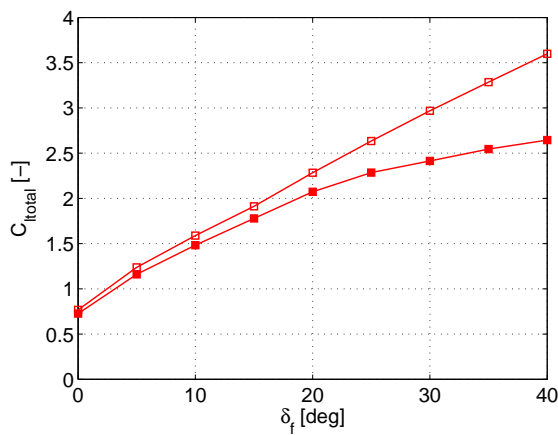
(c) C_{ltotal} versus δ_f at $\alpha = 4°$.
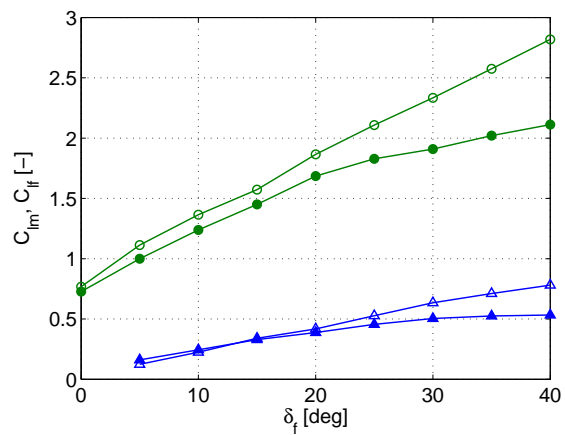
(d) C_{lmain} and C_{lflap} versus δ_f at $\alpha = 4°$.

Figure 6.5: MSES simulated C_l data for the NLF-MOD22(A) profile for $\alpha = 0°$ and $\alpha = 4°$ at $Re = 1.7 \cdot 10^6$.
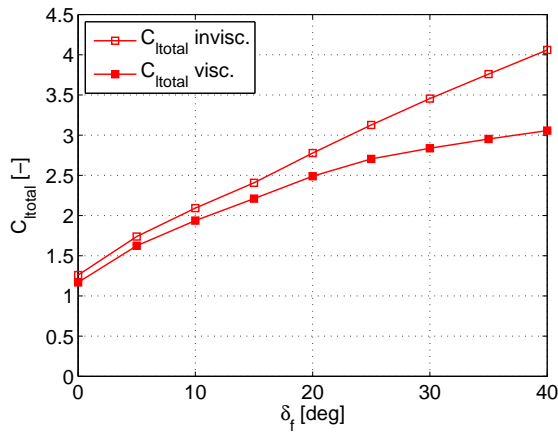
(a) $C_{l_{total}}$ versus δ_f at $\alpha = 8°$.
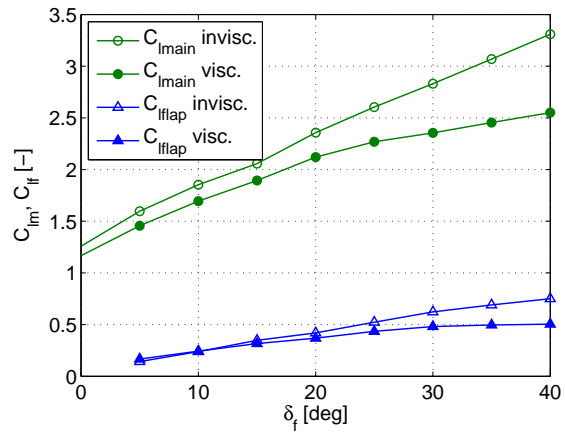
(b) $C_{l_{main}}$ and $C_{l_{flap}}$ versus δ_f at $\alpha = 8°$.
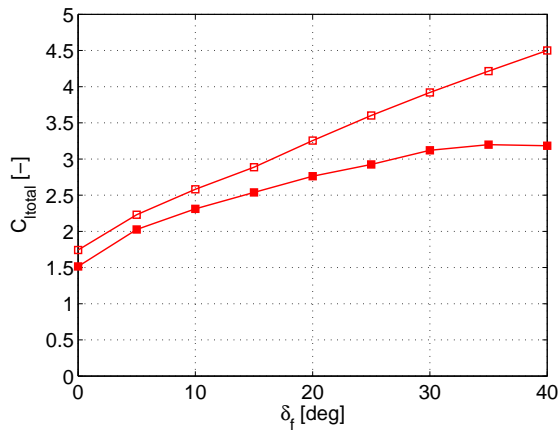
(c) $C_{l_{total}}$ versus δ_f at $\alpha = 12°$.
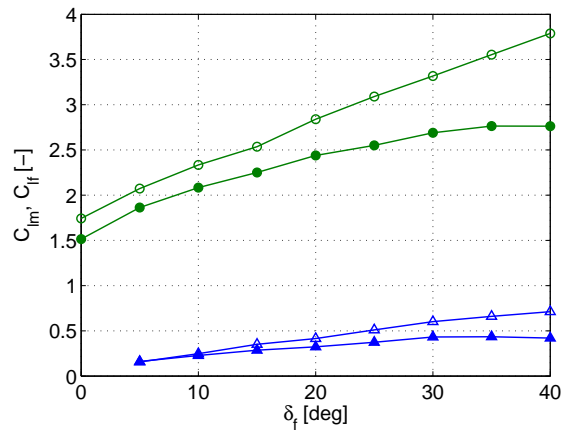
(d) $C_{l_{main}}$ and $C_{l_{flap}}$ versus δ_f at $\alpha = 12°$.

Figure 6.6: MSES simulated C_l data for the NLF-MOD22(A) profile for $\alpha = 8°$ and $\alpha = 12°$ at $Re = 1.7 \cdot 10^6$.
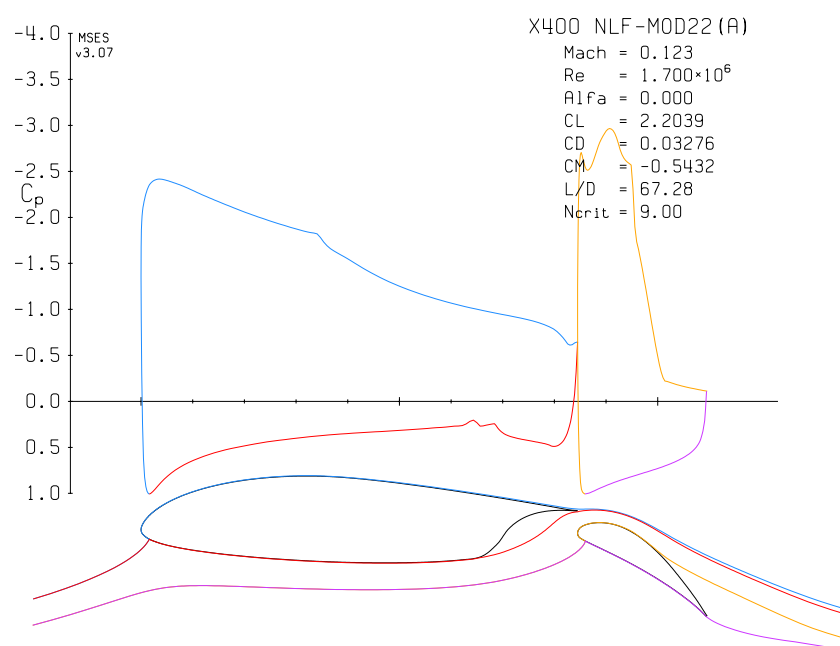
Figure 6.7: Example pressure distribution with $\delta_f = 40°$.
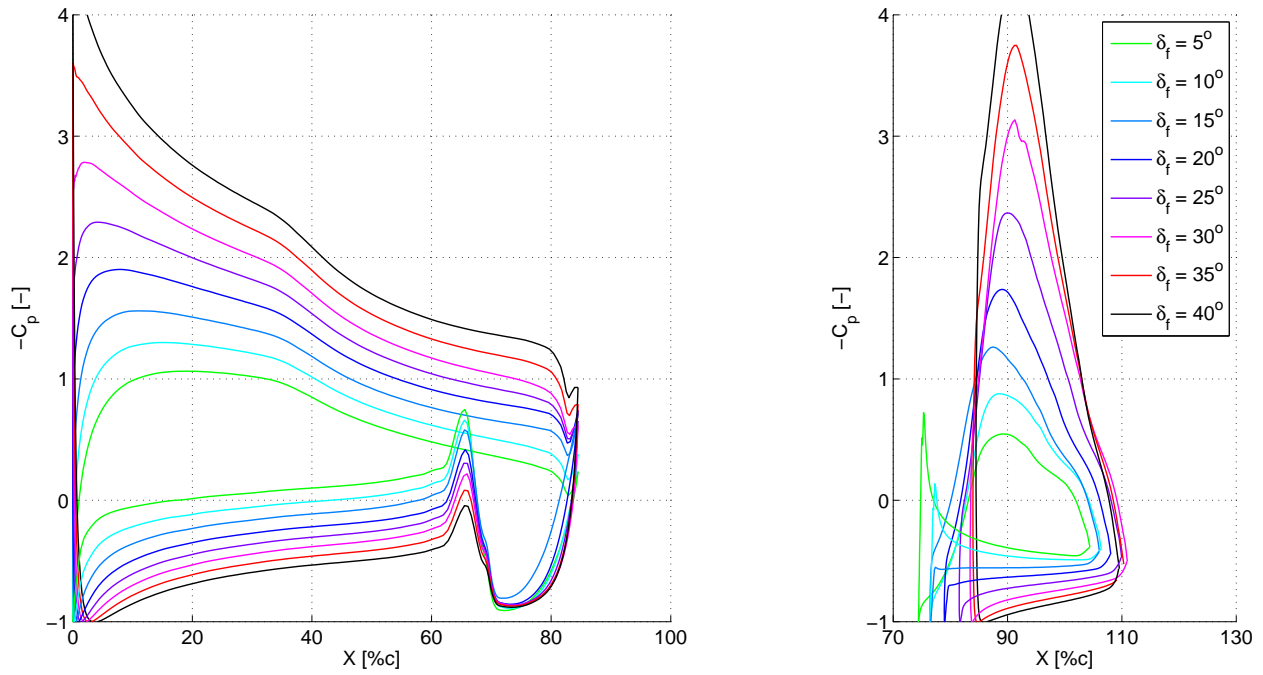
Figure 6.8: C_p distribution of NLF-MOD22(A) for $\alpha = 0°$, inviscid MSES calculation.
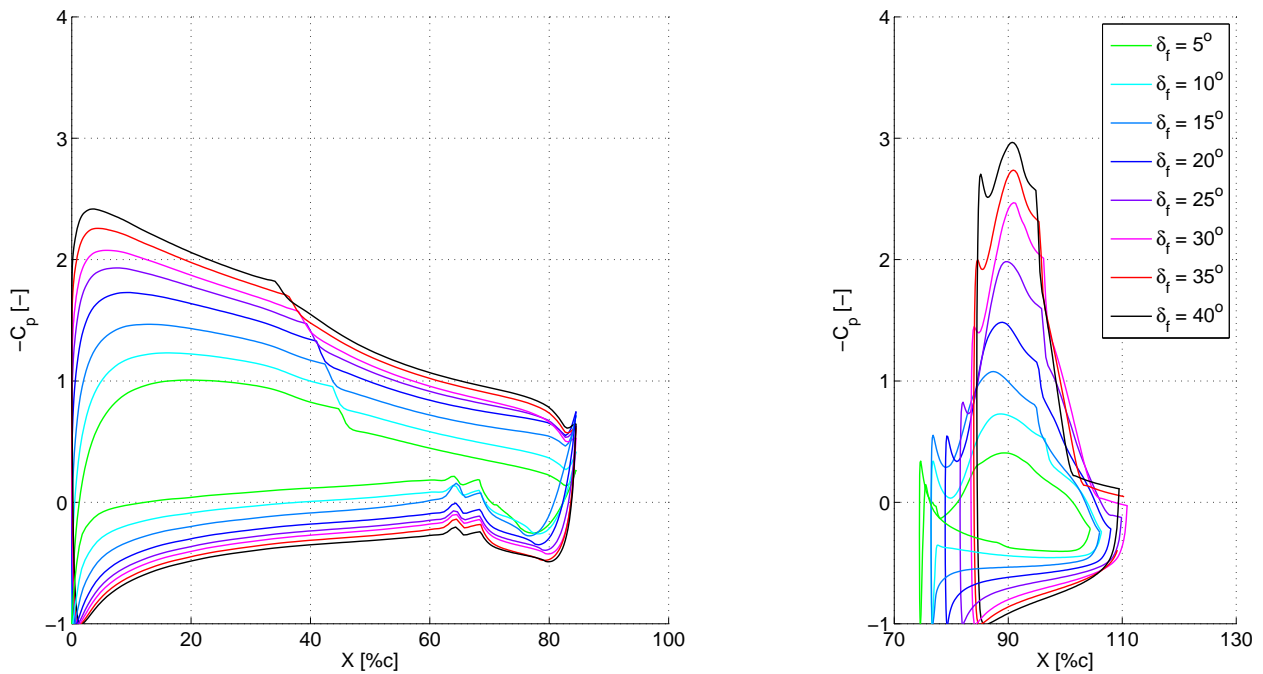
Figure 6.9: C_p distribution of NLF-MOD22(A) for $\alpha = 0°$ and $Re = 1.7\cdot10^6$, viscous MSES calculation.
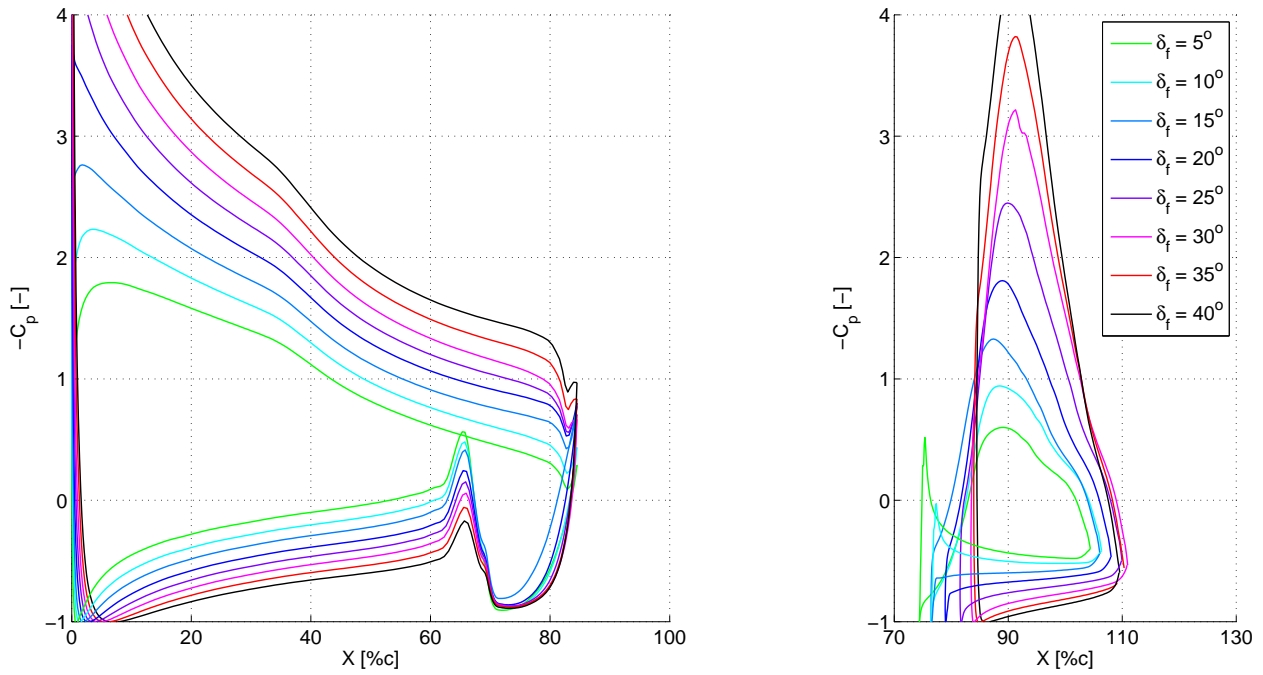
Figure 6.10: C_p distribution of NLF-MOD22(A) for $\alpha = 4°$, inviscid MSES calculation.
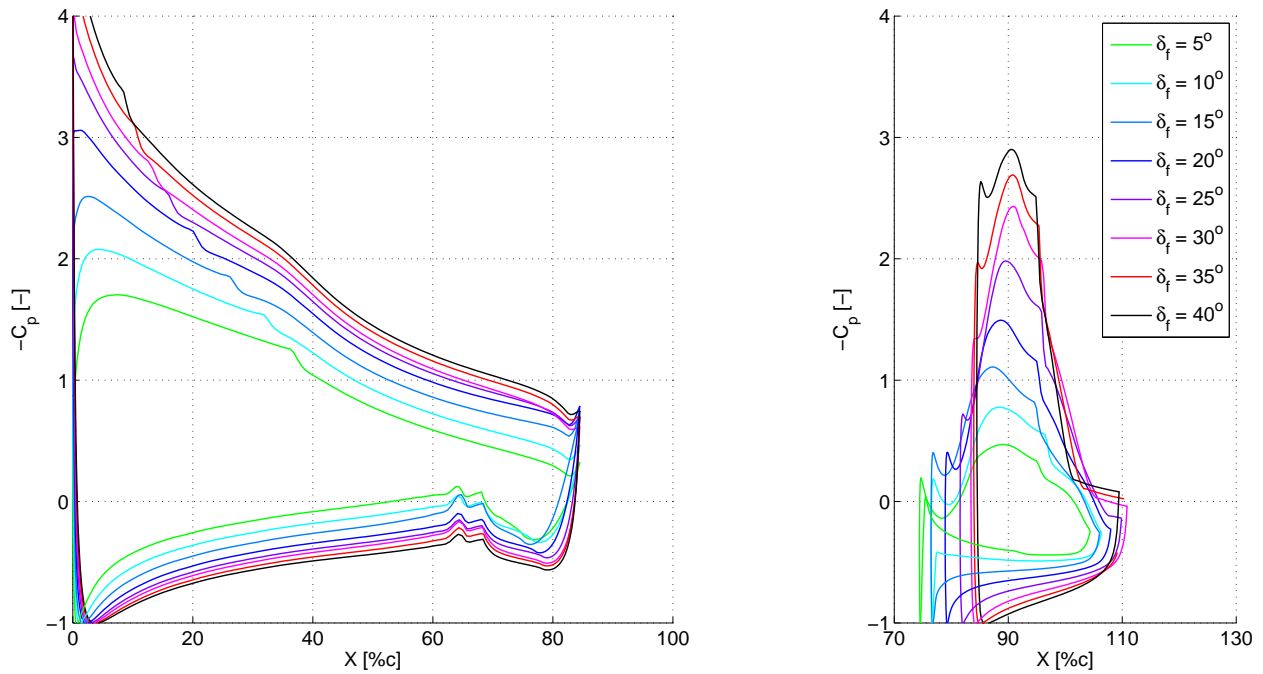
Figure 6.11: C_p distribution of NLF-MOD22(A) for $\alpha = 4°$ and $Re = 1.7 \cdot 10^6$, viscous MSES calculation.
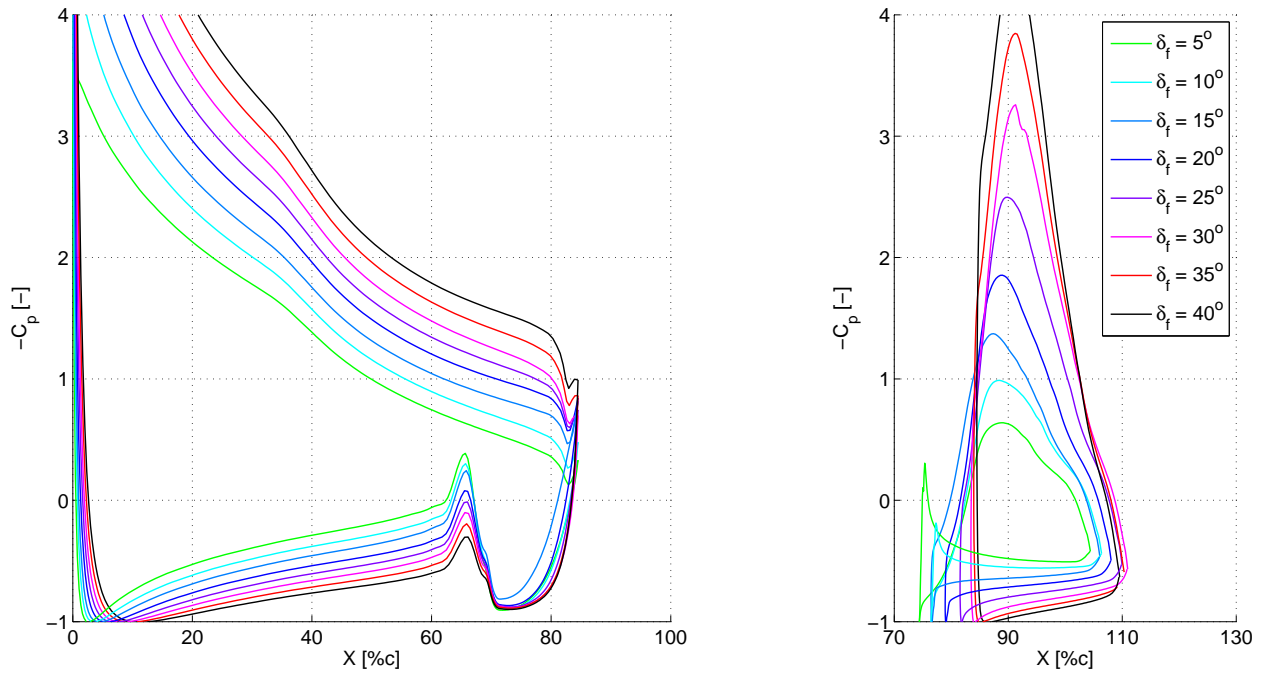
Figure 6.12: C_p distribution of NLF-MOD22(A) for $\alpha = 8°$, inviscid MSES calculation.
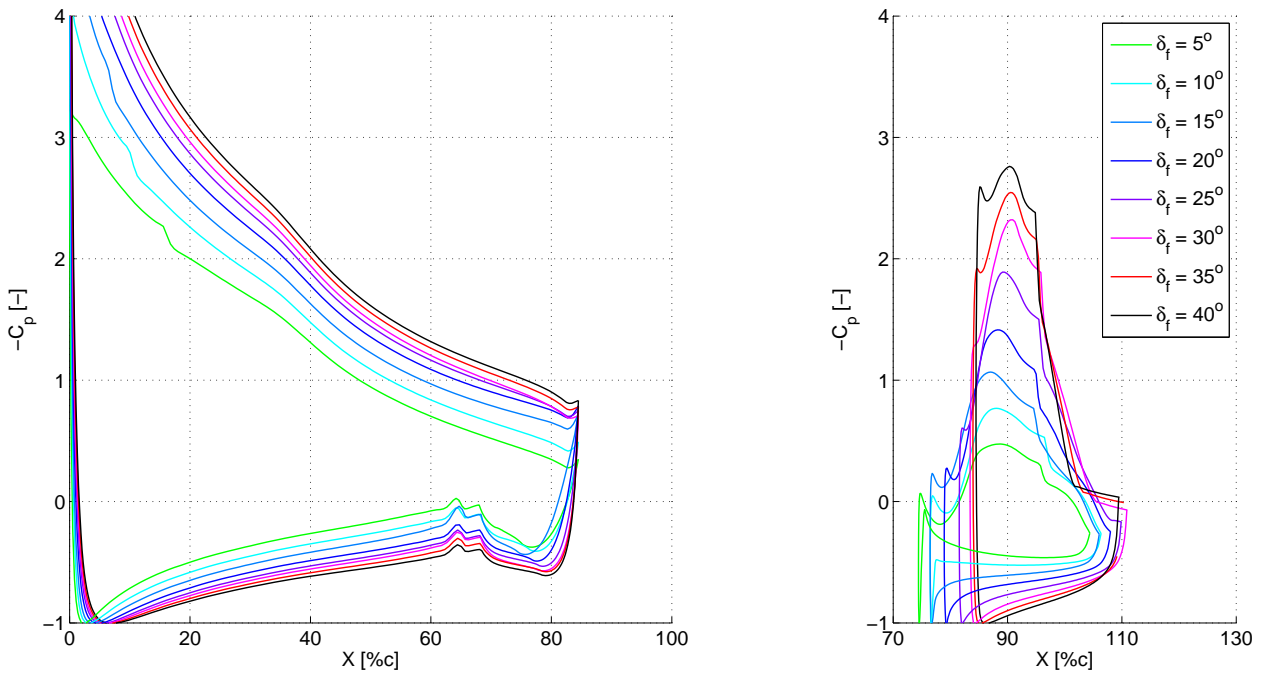
Figure 6.13: C_p distribution of NLF-MOD22(A) for $\alpha = 8°$ and $Re = 1.7 \cdot 10^6$, viscous MSES calculation.
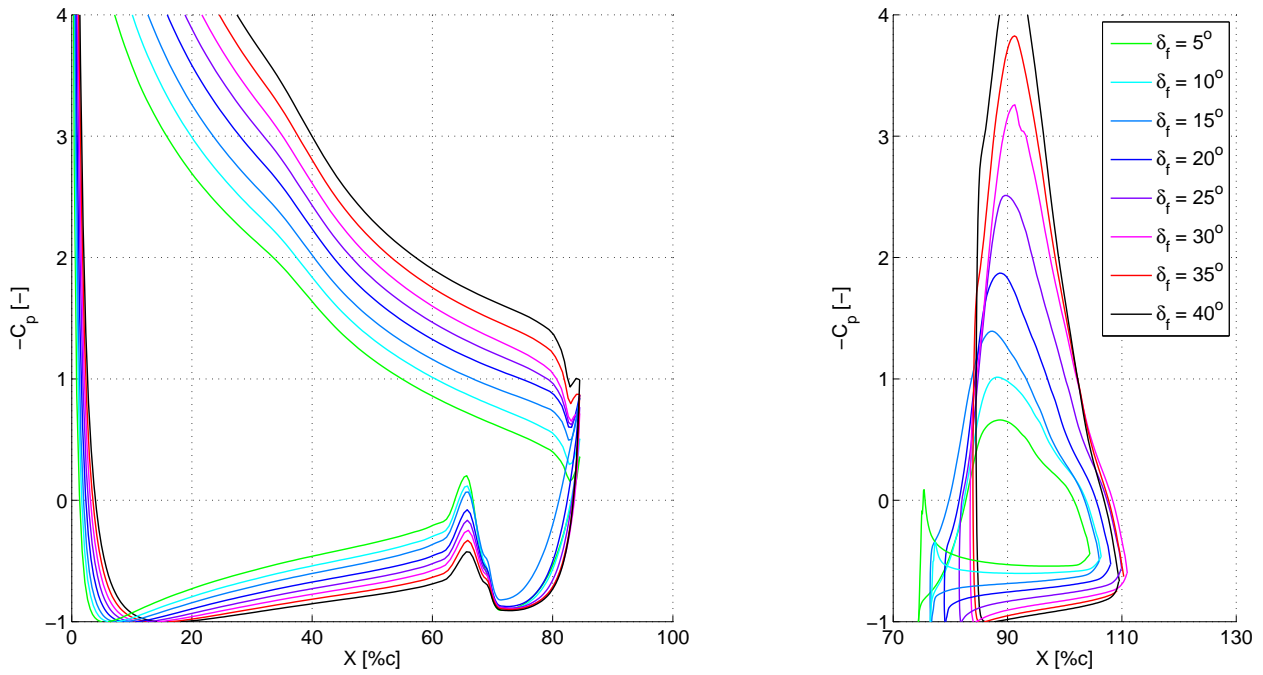
Figure 6.14: C_p distribution of NLF-MOD22(A) for $\alpha = 12°$, inviscid MSES calculation.
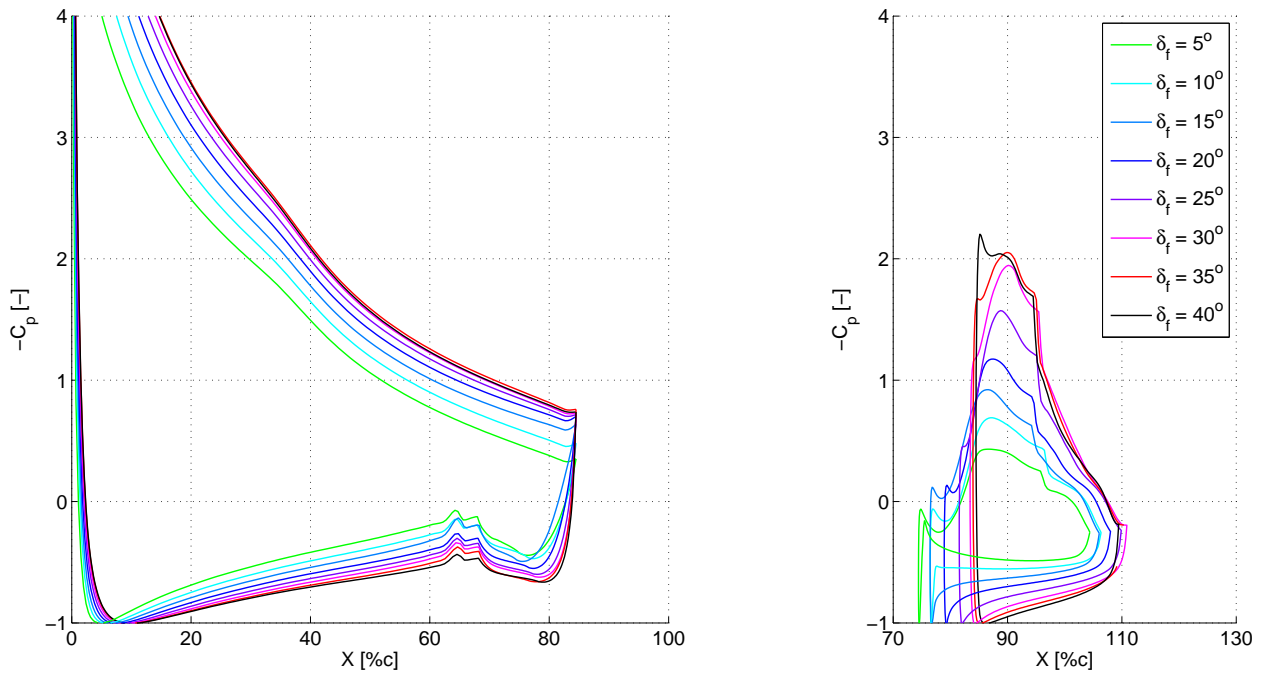
Figure 6.15: C_p distribution of NLF-MOD22(A) for $\alpha = 12°$ and $Re = 1.7 \cdot 10^6$, viscous MSES calculation.
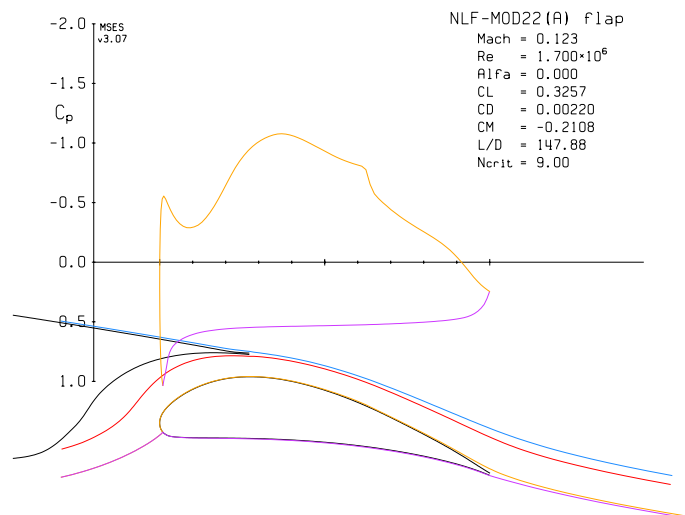
Figure 6.16: Simulation with main element, flap's C_p distributions for $\delta_f = 15°$.
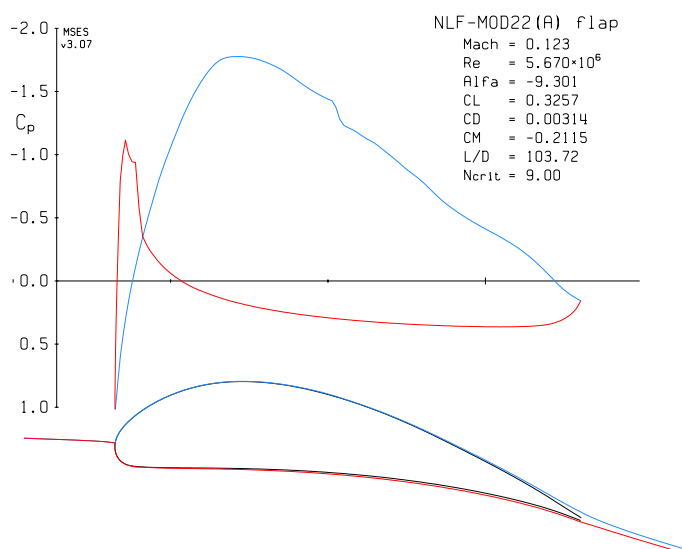
Figure 6.17: Simulation without main element, flap's C_p distributions for $\delta_f = 15°$.
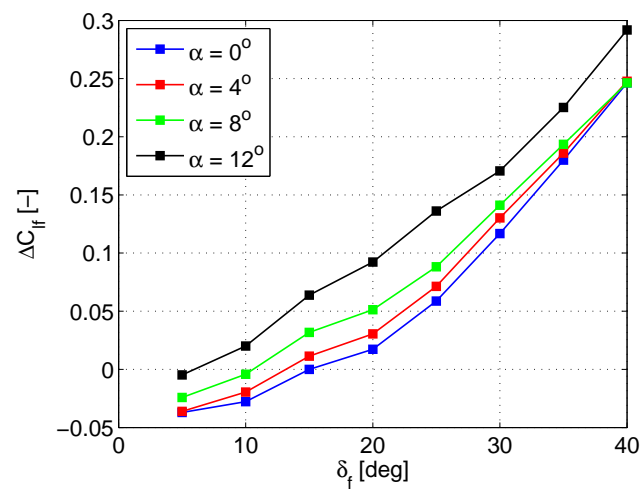
Figure 6.18: $\Delta C_{lflap}(= C_{lf,invisc.} - C_{lf,visc.})$ versus δ_f for different angle of attack, $Re = 1.7 \cdot 10^6$.

6.4 Adapted pressure distribution for attached flow

In order to complete the analysis in this chapter we want to see how the pressure distributions are being affected if the flow is completely (re)attached on the flap. With MSES this was done showing the inviscid calculations, which is probably to optimistic but certainly shows the limits of what can be achieved. The approach for this part of the analysis however goes back to the LTT with the physical NLF-MOD22(B) model, set at 0° angle of attack and again a 45° flap angle. To reattach the flow around the flap an "external slat", mounted on a beam, is pushed into the tunnel under a certain angle. A schematic lay out of this test setup is shown in Figure 6.19, more illustrations of the setup can be found in Appendix A.

The presence of the "external slat" suppresses the flap upper surface pressure distribution, which reduces separation on the flap as soon as a favorable pressure gradient is reached. Experiments are conducted at two speed levels, i.e. $V = 42m/s$ and $V = 20m/s$, and any hysteresis effect is shown by pushing the slat in or pulling it out of the tunnel. The results consist of the pressure distributions, the total lift coefficients and the lift breakdown for the separate elements. The lift is here calculated by integration of the pressure distribution and thus no windtunnel corrections are applied. Therefore the real C_l value deviates from the calculated ones, what means that a reasonable quantitative comparison is not possible. However we can tell something about a general improvement or deterioration (a qualitative comparison) which is sufficient within the scope of this analysis.

The results are divided into the following cases:

- Hysteresis 1a: slat pushed in, $V = 42m/s$

- Hysteresis 1b: slat pulled out, $V = 42m/s$

- Hysteresis 2a: slat pushed in, $V = 20m/s$

- Hysteresis 2b: slat pulled out, $V = 20m/s$
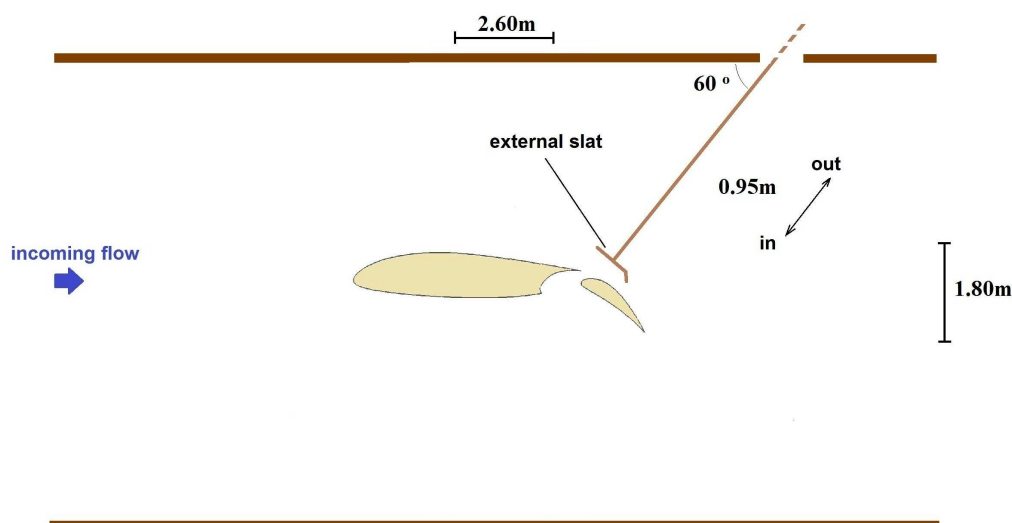
Figure 6.19: Schematic of top view LTT with extertal slat to perform manipulated pressure distribution measurements; shown is slat at maximum length of 0.95m i.e. 0.15m from the flap's upper surface.

Discussion

There is no hysteresis effect for $V = 42m/s$. The pressure distributions for the external slat pushed in or pulled out are identical (Figure 6.20 and 6.22). The total lift coefficient and lift breakdown support this observation (Figure 6.21 and 6.23). Pushing the slat gradually in shows that the pressure distribution on the flap gets "fuller" (flat C_p due to separated flow disappears) and the flap's lift coefficient increases. At the same time the main element looses lift continuously. A maximum $C_{l\,flap}$ is reached when the external slat is at 0.30m distance from the flap showing a $\Delta C_{l\,flap}$-increase of 0.06 with respect to the clean setup; the flow is then mostly attached over the flap's upper surface with a small separated region on the aft side. Assuming that a correction factor is of low order of magnitude, the corrected $\Delta C_{l\,flap}$ should not deviate much from 0.06. Thus a careful comparison shows that the current gain is still significant lower than the potential gain of 0.3 deduced from Figure 6.18. This is a very important observation as it suggests that a completely elimination of flow separation on the flap (by any control method) gives merely a lift increase in the order of one hundredth. Furthermore, moving the slat closer to the flap decreases $C_{l\,flap}$ significantly as well as $C_{l\,main}$. The same features are visible if the external slat is pulled out.

For $V = 20m/s$ small hysteresis effects occur. One can notice small differences between the pressure distributions in Figure 6.24 and 6.26. The lift curves indicate the differences more clearly, see Figure 6.25 and 6.27. More important however is the qualitative comparison which shows that the features are still the same as previous case; gradually reattachment of the flow on the flap is coupled with a decrease of the main's element lift coefficient. The reattachment of the flow in this case gives a $\Delta C_{l\,flap}$ increase of approximately 0.05.

In conclusion, even though flow separation from the flap could be prevented by a specific flow control mechanism, the airfoil will probably deal with a much greater problem: significant lift decrease from the main element which reduces the total lift force. This is due to the occurrence of a phenomenon known in literature as *wake bursting*, a specific type of stall. The low momentum wake of an upstream element could adversely be affected by the pressure gradients in the field of a downstream element. If the adverse pressure gradient is too great, the low momentum wake of the upstream element is decelerated and may even experience an off-the-surface flow reversal. Rapid growth of the wake consequently effectively decambers the airfoil system and reduces its circulation leading to a loss in lift [8][17], as also observed in current experiment. The minimal valued $C_{l\,flap}$ improvement becomes thereafter overruled by this phenomenon. More in depth study about the physics and maybe prevention of wake bursting is left for future researchers at Delft University of Technology.

Hysteresis 1a: slat pushed in, $V = 42m/s$
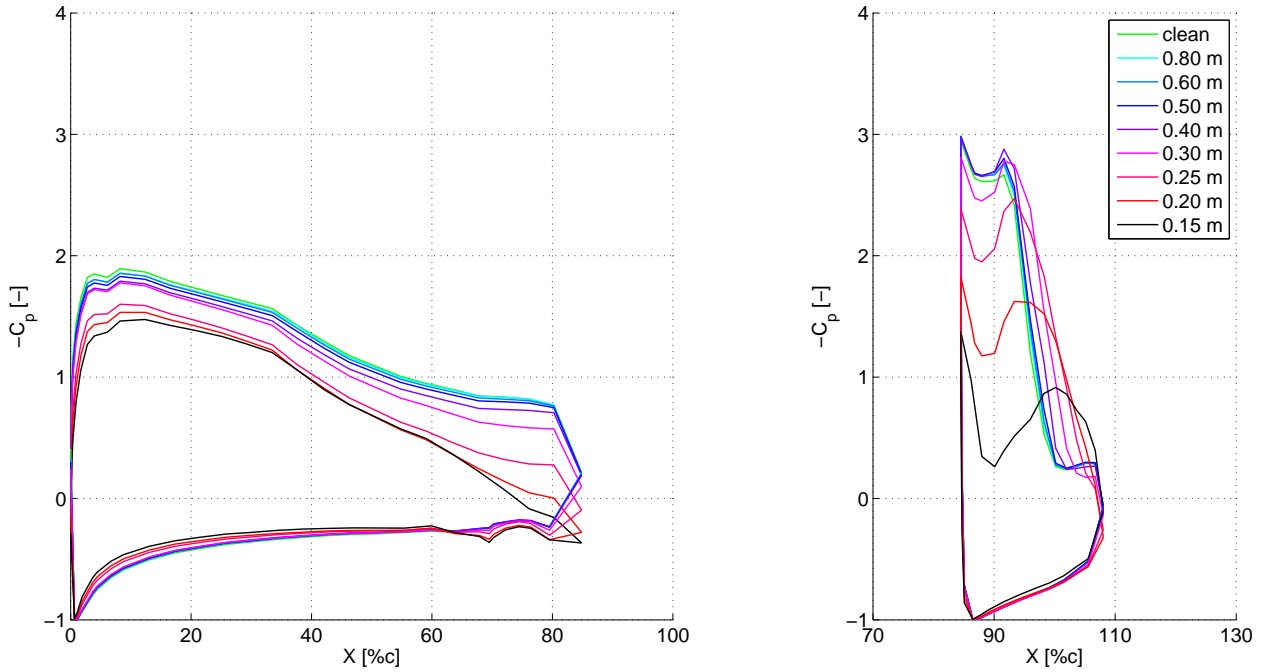
Figure 6.20: C_p distribution of NLF-MOD22(B) with external slat pushed in at $V = 42m/s$. Distributions shown for different slat distances to flap ($\delta_f = 45°$ and $Re = 1.7 \cdot 10^6$).
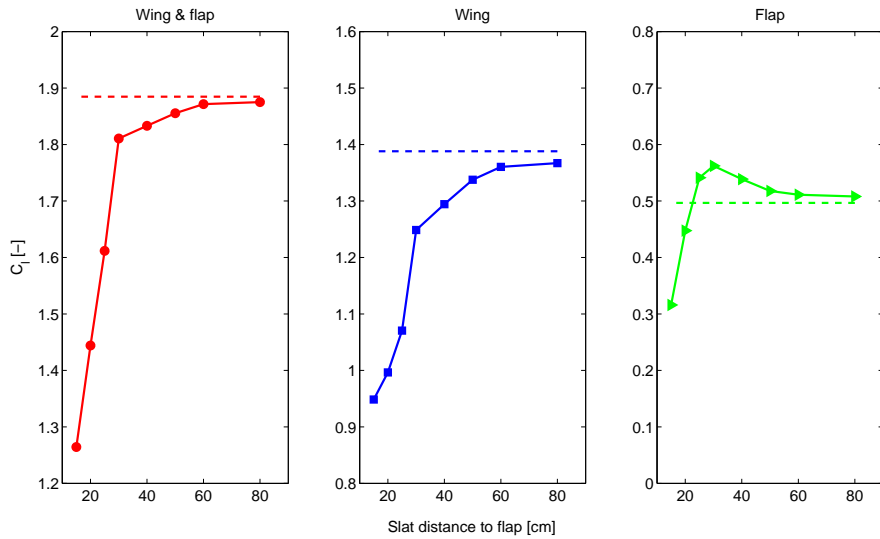
Figure 6.21: C_l breakdown at $42m/s$. Dashed line represents the clean, undisturbed setup.

Hysteresis 1b: slat pulled out, $V = 42m/s$
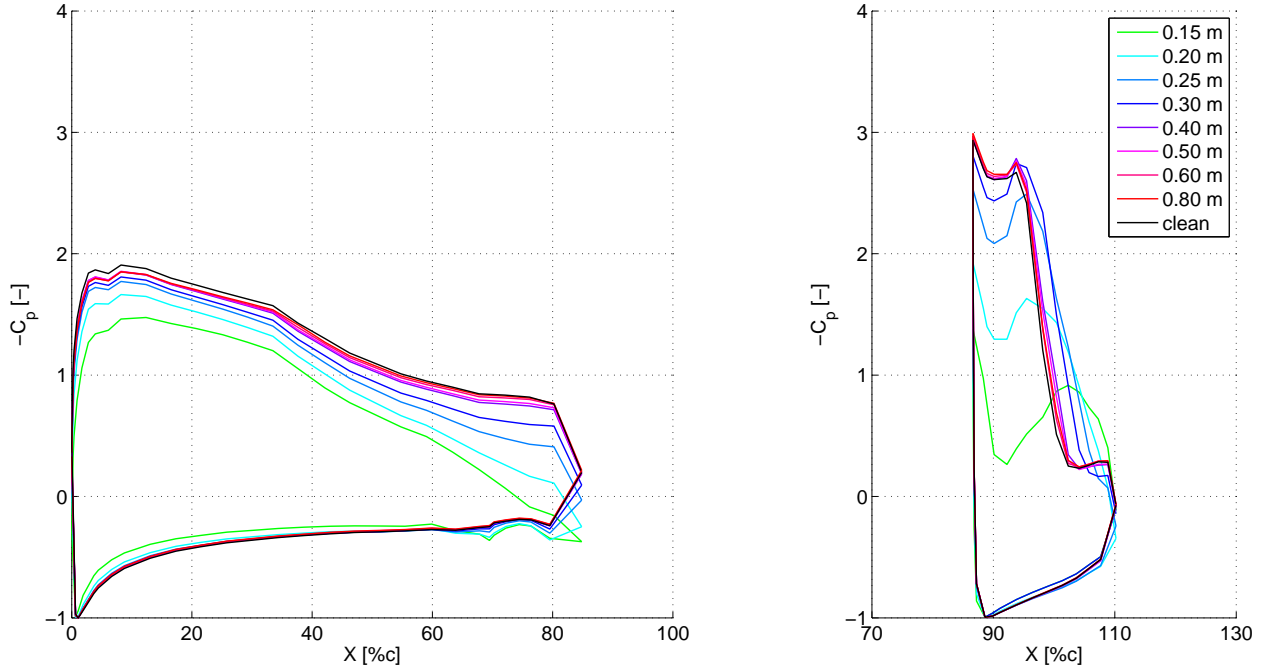
Figure 6.22: C_p distribution of NLF-MOD22(B) with external slat pulled out at $V = 42m/s$. Distributions shown for different slat distances to flap ($\delta_f = 45°$ and $Re = 1.7 \cdot 10^6$).
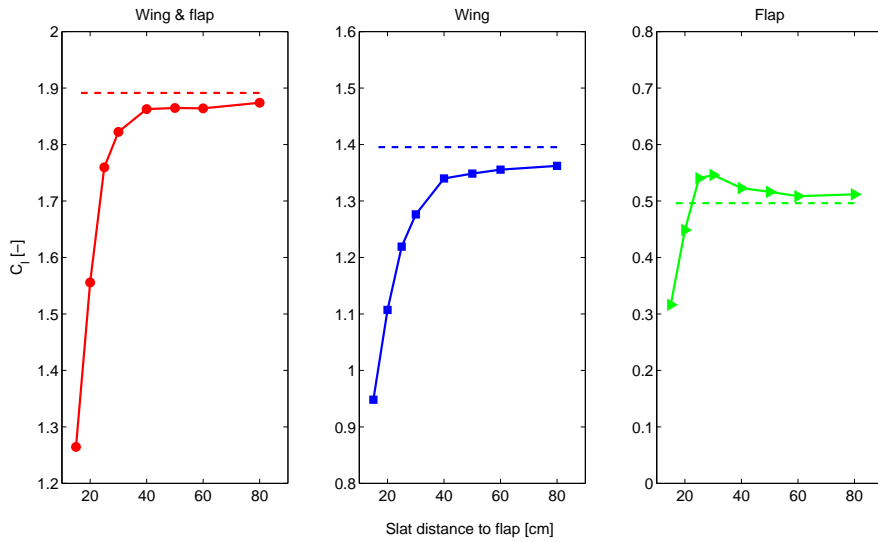
Figure 6.23: C_l breakdown at $42m/s$. Dashed line represents the clean, undisturbed setup.

Hysteresis 2a: slat pushed in, $V = 20m/s$
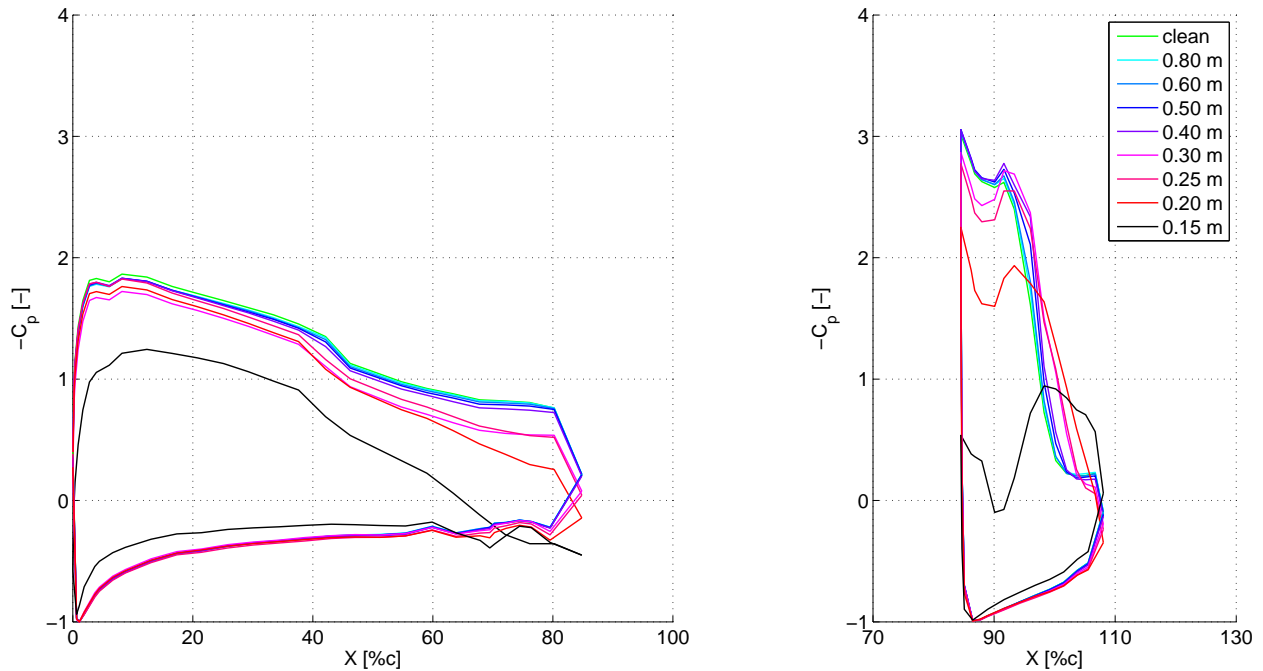
Figure 6.24: C_p distribution of airfoil NLF-MOD22(B) with external slat pushed in at $V = 20m/s$. Distributions shown for different slat distances to flap ($\delta_f = 45°$ and $Re = 0.85 \cdot 10^6$).
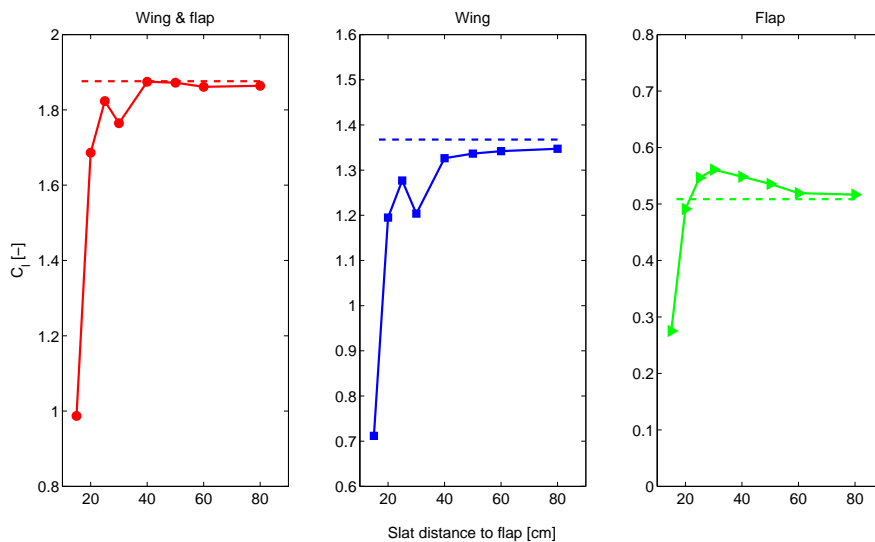
Figure 6.25: C_l breakdown at $20m/s$. Dashed line represents the clean, undisturbed setup.

Hysteresis 2b: slat pulled out, $V = 20m/s$
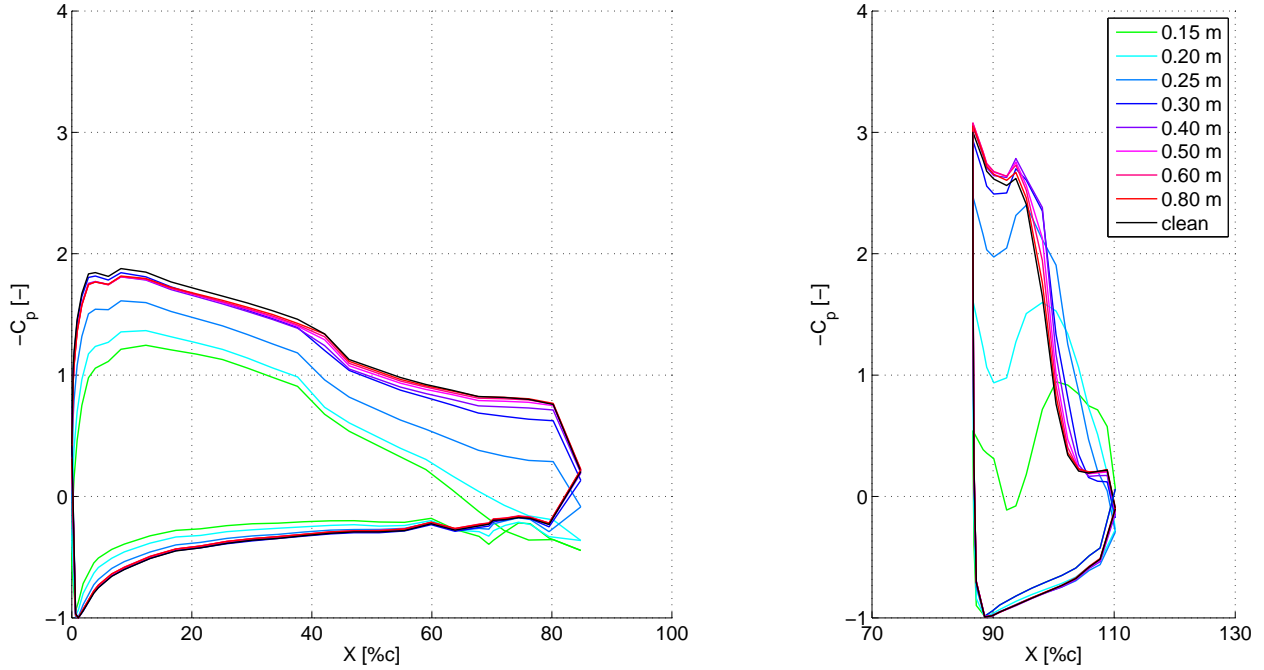
Figure 6.26: C_p distribution of airfoil NLF-MOD22(B) with external slat pulled out at $V = 20m/s$. Distributions shown for different slat distances to flap ($\delta_f = 45°$ and $Re = 0.85 \cdot 10^6$).
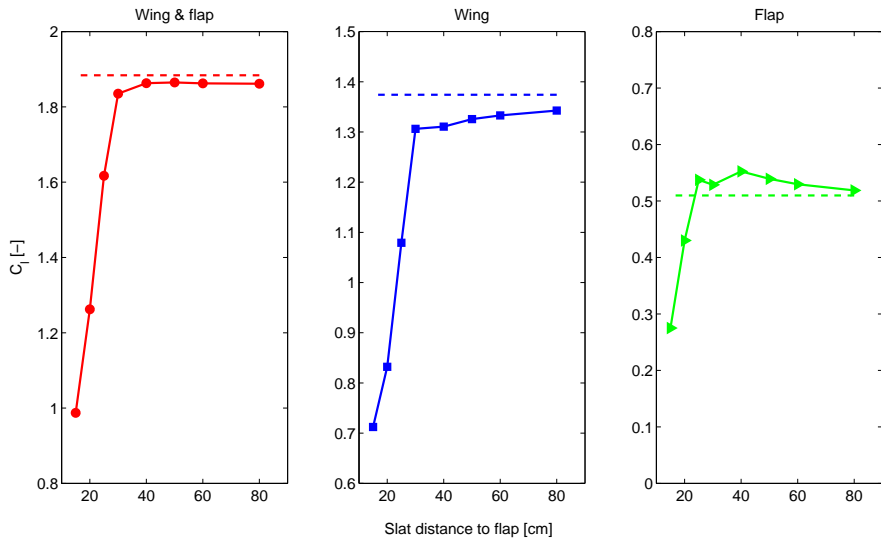
Figure 6.27: C_l breakdown at $20m/s$. Dashed line represents the clean, undisturbed setup.

Chapter 7

Conclusions and Recommendations

7.1 Conclusions

The research on high lift systems showed that multi-element airfoils develop towards a circular arc to attain a maximum lift force. Flow control becomes essential to overcome lift loss due to separation. Within the scope of lift improvement, the effect of flap leading edge applications was investigated for a wing-flap model, the NLF-MOD22(B). The focus was on critical flight conditions, i.e. a high flap deflection angle of $45°$ and $Re = 1.7 \cdot 10^6$.

Clean flap experiments showed that the airfoil is characterized by some favorable features. At low angles of attack the main element deals with largely attached flow, whereas on the flap the flow is partially separated. Increasing the angle of attack towards stalled condition, the flow on the main element separates while due to the displacement effect of the main airfoil wake, the flow around the flap gets fully attached. This observation indicated that flow actuation could only benefit at low angles of attack as at higher angles the flow around the flap is already naturally attached. Furthermore, the hysteresis effect was relatively low since the flow characteristics turn back by decreasing the angle of attack.

Insight into the flow dynamics on the flap was obtained by oil flow visualization which demonstrated the separated flow pattern up to stall. Separation did not occur two-dimensional, but three-dimensional in the form of stall cells. These are independent stationary separated flow regions, in which the flow organizes around multiple counter rotating loci. This effect was not caused due to windtunnel wall interference effects since literature [37] has shown that it also occurs on wall-free, finite wing models.

Separation delay by means of passive tripping was investigated using three different types of roughness: zigzag tape, carborundum grains and V-shaped turbulators. Results showed that these applications deteriorate the total lift performance with approximately 30%. The total drag was even more than doubled. To take account for the effectiveness of active flow control due to limitations of the driving generator and at the same time to prevent that the two-dimensionality of the flow was affected, the effect of the length of an applied roughness was analyzed to determine the minimum actuator length; for correct two-dimensional measurements an actuator should span at least 80% of the total flap span.

Several plasma actuator configurations were analyzed of both the AC DBD as the NS DBD plasma actuator. However, no significant effects could be achieved on flow separation control over the flap. This was partially due to model itself; conductive materials caused local unwanted discharge, deteriorating the overall efficiency. Related to this is the lack of data because of covered pressure taps when attaching the plasma actuator to the surface. More important is the three-dimensional flow characteristics on the flap (stall cells). It is hypothesized that the induced momentum or vortices, by the AC DBD and NS DBD plasma actuator respectively, was just of insufficient magnitude to overcome the strong three-dimensional separated flow.

With the actuation techniques showing no lift improvement, i.e. no noticeable effect on separation delay on the flap, the maximum attainable lift for ideal flow control was calculated using the CFD-software MSES. Maximum attainable lift was obtained with inviscid calculations. Compared with viscous calculations this gave us the lift-loss-progress as function of the flap deflection angle. At low angles of attack, appropriate flow control applications become especially interesting at flap angles higher than $20°$.

Finally, experiments with pressure distribution adaption for attached flow were carried out. It was shown that even though flow separation from the flap could be prevented, the airfoil now has to deal with wake bursting. This phenomenon limits to a great extent the maximum possible lift performance.

We can conclude that the selected configuration for improvement was to extreme. The relatively large model, high flap deflection and large Reynolds number appeared to be to difficult to achieve separation elimination. A lower flap angle is proposed for upcoming experiments. Hence, while preserving a case with partially separated flow on the flap but with less adverse pressure gradients, a switch to a flap deflection angle of $30°$ is recommended. A better understanding for the exact position of the plasma actuator is necessary. Literature has shown that the most effective placement, is on or slightly upstream the separation point for single element airfoils. For two element airfoils the flow is more complicated which requires a different approach, especially when separation occurs on a non-straight line (stall cells). Furthermore, the potential of lift improvement could strongly be limited due to wake bursting.

7.2   Recommendations

Current research presented a good analysis of some flap leading edge applications. To continue the research, especially with respect to plasma actuators, the following approaches are recommended to get a better understanding of its application on multi-element airfoils:

- The most important thing is to take a step back in model size. The size of current model made it difficult to notice any macroscopic improvement. So a scaled wing-flap model is ideal to start with. This will not only give a better controllability over the generated plasma but furthermore a greater convenience to filter out sources of efficiency losses. Another important requirement is that the model is completely manufactured from a dielectric material.

- The intermediate step to a large wing-flap model, is to analyze firstly a large single element model. This will give insight into the limitations of the plasma actuator in terms of size. Preferably again is to use a non-conductive model.

- For subsequent experiments on the NLF-MOD22(B) airfoil model adaptions should be made to the skin. It is hypothesized that stronger discharge (in case of AC DBD plasma actuator)

is required to get it work under critical flow circumstances. Kapton dielectric tape becomes unsuitable, as we need a significantly thicker dielectric. Adding multiple layers Kapton is a backup option, but still this is critical point due to locally burn out. Especially with the intention to get plasma actuation a step closer towards "industrial application", the study on stronger dielectrics to implement it on existing airfoils is crucial. For the NLF-MOD22(B) a new flap model is already made, with an adapted part of the upper skin. This part is made of fiber glass, what makes it a very good start for further research on plasma actuation. Also this new flap model can be deflected more easily in contrast to the flap in this research.

- Related to the NLF model, more attention should be paid to the way data is read from the flow. The old flap model as well as the new one do all pressure readings by means of pressure holes along the surface. This means that part of the tabs are directly covered, uncovering them may create spots of locally discharge and also disturbances because of relief differences. It must be considerd if the pressure tubes can be manufactured of some hard plastic instead of the existing metal ones.

- Investigate in-dept the potentional of DBD VG on flaps. In current research this was not entirely possible because the biggest part of the pressure data went lost as the actuator covered almost 75% of the holes. A PIV setup is more suitable for this experiment to analyze the vortex development in time and space, and to observe the effect on separation delay.

- Currently, other experiments at TU Delft using passive flow control on the flap showed again the occurrence of wake bursting. It could be that the lift limits within this configuration are reached, what limits the effect of any flow control. Therefore, it is strongly recommended to investigate this phenomena and to see if besides separation delay also wake bursting can be prevented.

Bibliography

[1] Nordian Edition 6 EASA ATPL Manual 13. *Principles of Flight.*

[2] J.D. Anderson. *Fundamentals of Aerodynamics.* 2001.

[3] C. Bak, P. Fuglsang, J. Johansen, and I. Antoniou. Wind tunnel tests of the naca 63-415 and a modified naca 63-415 airfoil. *Riso-R-1193(EN)*, 2000.

[4] L.M.M. Boermans and P.B. Rutten. Internal rapport lsw 95-3, two-dimensional aerodynamic characteristics of airfoil nlf-mod22 with fowler flap. *Technical University Delft, Department of Aerodynamics*, 1995.

[5] T.C. Corke, M.L. Post, and D.M. Orlov. Sdbd plasma enhanced aerodynamics: concepts, optimization and applications. *Progress in Aerospace Sciences*, 43:193–217, 2007.

[6] G. Correale. Preliminary investigation on ns-dbd plasma actuator for active flow separation control. *Master's thesis, Delft University of Technology*, 2011.

[7] G. Correale, I.B. Popov, A.E. Rakitin, A.Yu. Starikovskii, S.J. Hulshoff, and L.L.M. Veldhuis. Flow separation control on airfoil with pulsed nanosecond discharge actuator. 49th *AIAA Aerospace Sciences Meeting, Orlando, Florida*, 2011.

[8] Driver D.M and G.G. Mateer. Wake flow in adverse pressure gradient. *International Journal of Heat and Fluid Flow*, 23:564–571, 2002.

[9] M. Drela. *A User's Guide to MSES 3.04.* 2005.

[10] M. Drela and M.B. Giles. A two-dimensional viscous aerodynamic design and analysis code. 25th *AIAA Aerospace Sciences Meeting, Reno Nevada*, 87, 1987.

[11] C.L. Enloe, T.E. McLaughlin, R.D. VanDyken, and K.D. Kachner. Mechanisms and responses of a single dielectric barrier plasma actuator: Geometric effects. *AIAA Journal*, 42, 2004.

[12] M. Forte, J. Jolibois, J. Pons, E. Moreau, G. Touchard, and M. Cazalens. Optimization of a dielectric barrier discharge actuator by stationary and non-stationary measurements of the induced flow velocity: application to airflow control. *Exp. Fluids*, 43:917–928, 2007.

[13] Mohamed Gad-El-Hak. *Flow Control: Passive, Active, and Reactive Flow Management.* 2000.

[14] D. Greenblatt and I.J. Wygnanski. The control of flow separation by periodic excitation. *Progress in Aerospace Sciences, Ramat Aviv, Israel*, 36:487–545, 2000.

[15] C. He, T.C. Corke, and M.P. Patel. Plasma flaps and slats: An application of weakly ionized plasma actuators. *Journal of Aircraft*, 46, 2009.

[16] S.F. Hoerner and H.V. Borst. Fluid-dynamic lift. *Hoerner Fluid Dynamics*, 1975.

[17] R. Hoffenberg and J.P. Sullivan. Simulation of high-lift wake behavior. *Aerospace Sciences Meeting, Reno, Nevada*, 1997.

[18] J. Huang, T.C. Corke, and F.O. Thomas. Plasma actuators for separation control of low-pressure turbine blades. *AIAA Journal*, 44, 2006.

[19] T.N. Jukes and Kwing-So Choi. Dielectric-barrier-discharge vortex generators: characterization and optimization for flow separation control. *Exp. Fluids*, 2011.

[20] S.M. Klausmeyer, M. Papadakis, and J.C. Lin. A flow physics study of vortex generators on a multi-element airfoil. 34th *AIAA Aerospace Sciences Meeting and Exhibit, Reno, Nevada*, 1996.

[21] J. Little, M. Nishihara, I. Adamovich, and M. Samimy. Separation control from the flap of a high-lift airfoil using dbd plasma actuation. 4th *Flow Control Conference, Seattle, Washington*, 2008.

[22] J. Little, M. Nishihara, I. Adamovich, and M. Samimy. Separation control from the flap of a high-lift airfoil using dbd plasma actuators. 47th *AIAA Aerospace Sciences Meeting including The New Horizons Forum and Aerospace Exposition, Orlando Florida*, 2009.

[23] J. Little, K. Takashima, M. Nishihara, I. Adamovich, and M. Samimy. High lift airfoil leading edge separation control with nanosecond pulse driven dbd plasma actuators. 5th *Flow Control Conference, Chicago, Illinois*, 2010.

[24] E. Moreau. Airflow control by non-thermal plasma actuators. *J. Phys. D: Appl. Phys.*, 40:605–636, 2007.

[25] E. Obert and R. Slingerland. Aerodynamic design of transport aircraft. *Delft University of Technology, Faculty of Aerospace Engineering*, 2003.

[26] D.M. Orlov and T.C. Corke. Numerical simulation of aerodynamic plasma actuator effects. 43th *AIAA Aerospace Sciences Meeting and Exhibit, Reno Nevada*, 2005.

[27] R. Petz and W. Nitsche. Active separation control on the flap of a two-dimensional generic high-lift configuration. *Journal of Aircraft*, 44, 2007.

[28] M.L. Post and T.C. Corke. Flow control with single dielectric barrier plasma actuators. 35th *AIAA Fluid Dynamics Conference and Exhibit, Toronto, Ontario Canada*, 2005.

[29] C. Rethmel, J. Little, K. Takashima, A. Sinha, I. Adamovich, and M. Samimy. Flow separation control over an airfoil with nanosecond pulse driven dbd plasma actuators. 49th *AIAA Aerospace Sciences Meeting including the New Horizons Forum and Aerospace Exposition, Orlando, Florida*, 2011.

[30] D. Rodriguez and V. Theofilis. On the birth of stall cells in airfoils. *Theor. Comput. Fluid Dyn.*, 2011.

[31] D.V. Roupassov, A.A. Nikilepov, M.M. Nudnova, and A.Yu. Starikovskii. Flow separation control by plasma actuator with nanosecond pulse periodic discharge. 46th *AIAA Aerospace Sciences Meeting and Exhibit, Reno, Nevada*, 2008.

[32] M. Schatz, F. Thiele, R. Meyer, W. Hage, and D.W. Bechert. Separation control by self-activated movable flaps. 42th *AIAA Aerospace Sciences Meeting and Exhibit, Reno, Nevada*, 2004.

[33] A.M.O. Smith. High-lift aerodynamics. *Journal of Aircraft*, 1975.

[34] A. Yu Starikovskii, A.A. Nikipelov, M.M. Nudnova, and D.V. Roupassov. *Plasma Sources Sci. Technology*, 18.

[35] F.O. Thomas, T.C. Corke, M. Iqbal, A. Kozlov, and D. Schatzman. Optimization of dielectric barrier discharge plasma actuators for active aerodynamic flow control. *AIAA Journal*, 47, 2009.

[36] Frank M. White. *Viscous Fluid Flow, 3nd ed.* 2005.

[37] A.E. Winkelmann. An experimental study of mushroom shaped stall cells. *AIAA, ASME 3rd Joint Thermophysics, FLuids, Plasma and Heat Transfer Conference, St. Louis, Missouri*, 1982.

Appendix A

Experimental background information

This Appendix contains additional information about the experiments and setups; illustrations are presented to give insight into the several aspects. For more information one is also referred to the main chapter to which the illustrations of this appendix belong to.
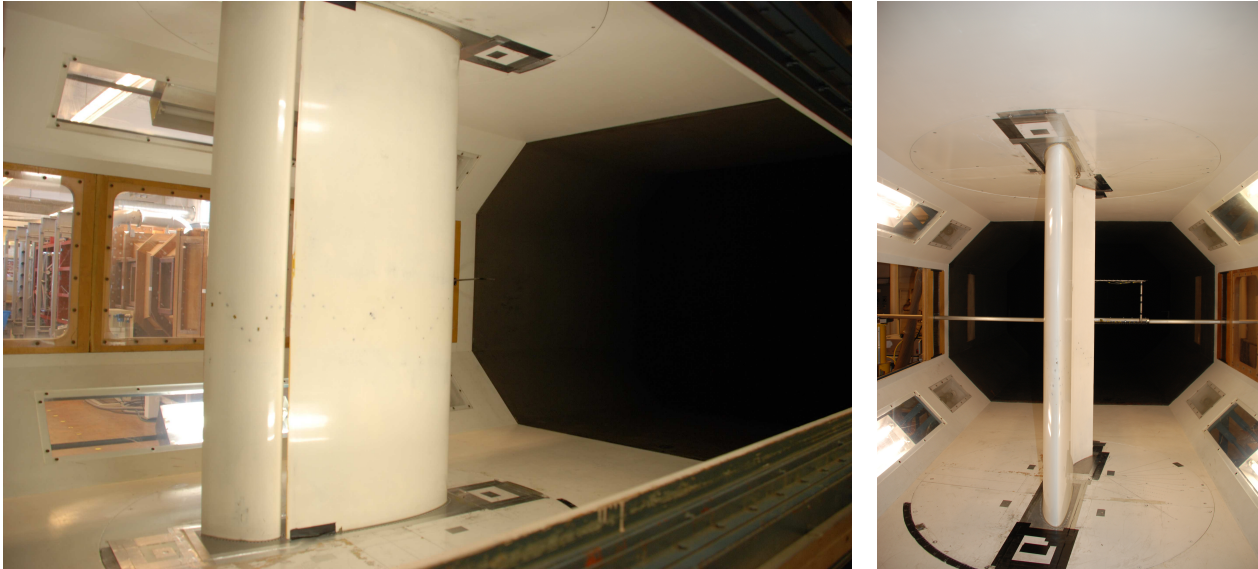
Figure A.1: The NLF-MOD22(B) airfoil model positioned in the LTT. The model was setup vertical to allow α adjustments. On the left, the side view is shown which corresponds to the upper surface of the airfoil i.e. the main element and the deflected flap. On the right, the front view of the airfoil is shown.

Figure A.2: Four metal support elements were attached to the lower surface of the airfoil, left from previous research. The elements were used to attach a cylindrical rod for vortex shedding. Because of possible follow-up studies with this configuration, it was decided to leave those elements attached.

Figure A.3: Different plasma actuator configurations. From left to right and top to bottom: AC DBD plasma actuator, NS DBD plasma actuator, two parallel NS DBD plasma actuator, DBD-VG for counter-rotating vortices and DBD-VG for co-rotating vortices.
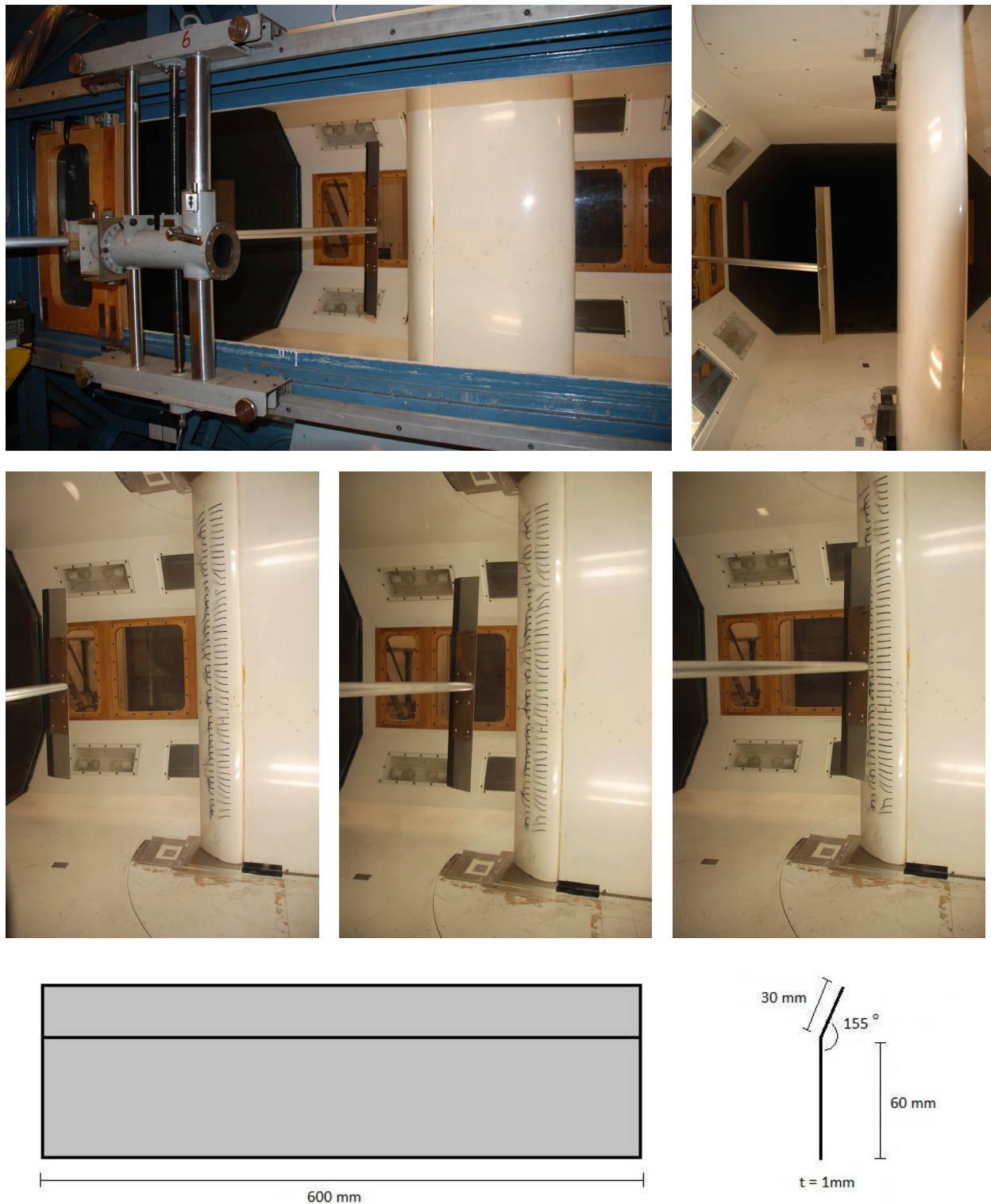
Figure A.4: Top: setup of the external slat to perform adapted pressure distributions measurements for attached flow. Middle: tuft visualization of the flow around the flap. Pushing the slat closer to the flap (picture from left to right) shows that the tufts get gradually attached to the surface. Bottom: slat dimensions.

Cp distributions

This Appendix summarizes the C_p distributions of the conducted experiments. The first section shows the C_p distributions with artificial transition. Section B.2 and Section B.3 show the distributions with active flow control, AC DBD and NS DBD plasma actuator respectively.

B.1   Artificial transition
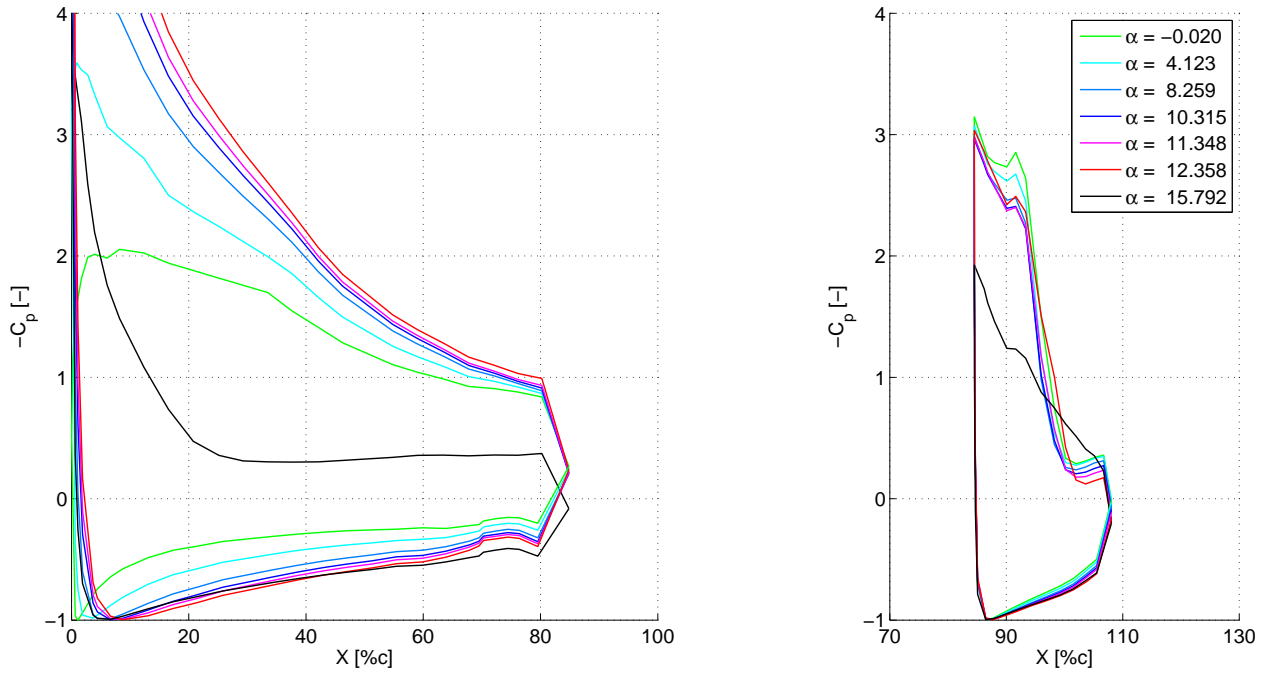
Figure B.1: C_p distribution of NLF-MOD22(B) with clean flap configuration for $\delta_f = 45°$, $x_{overlap} = 0\%c$, $y_{gap} = 3.5\%c$ and $Re = 1.7 \cdot 10^6$.
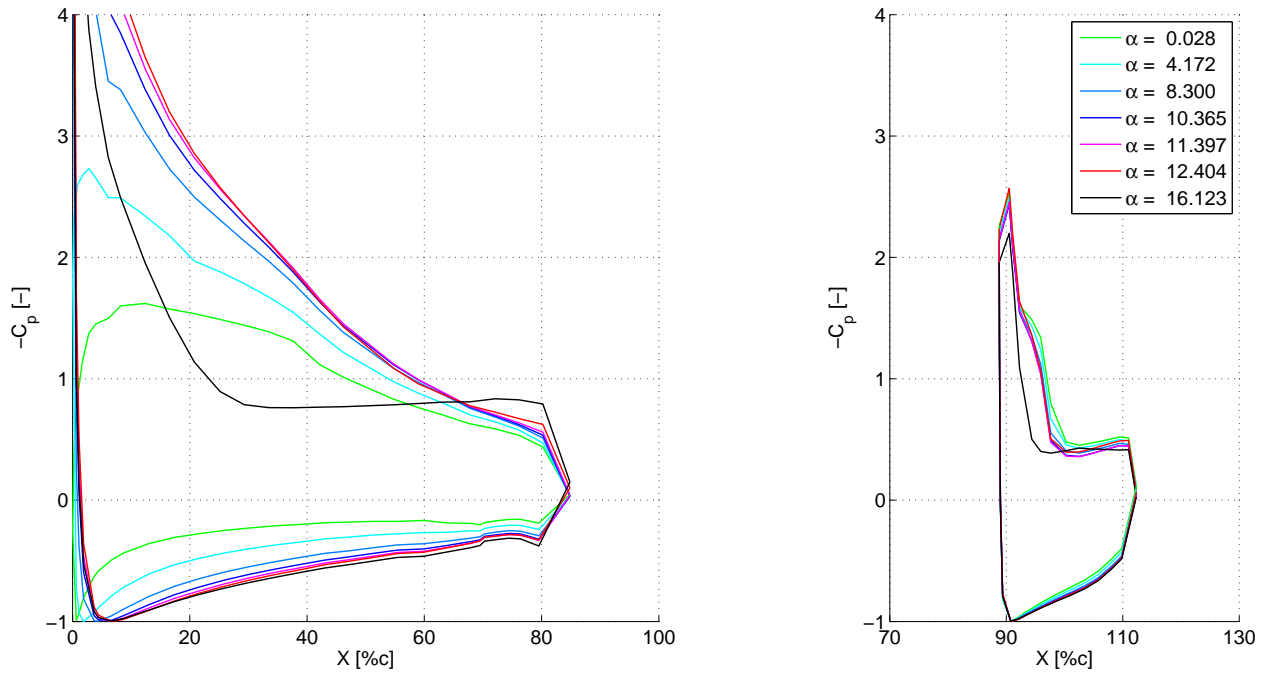
Figure B.2: C_p distribution of NLF-MOD22(B) with LER on flap: zigzag tape, for $\delta_f = 45°$, $x_{overlap} = 0\%c$, $y_{gap} = 3.5\%c$ and $Re = 1.7 \cdot 10^6$.
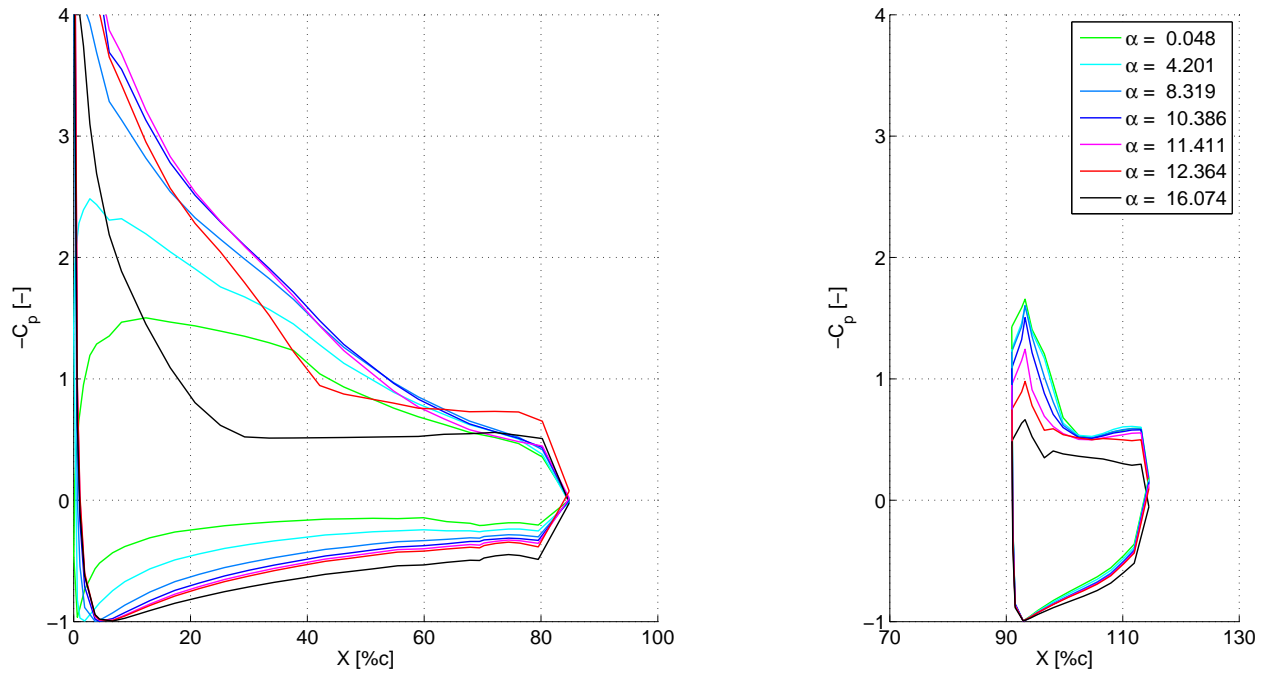
Figure B.3: C_p distribution of NLF-MOD22(B) with LER on flap: carborundum grains, for $\delta_f = 45°$, $x_{overlap} = 0\%c$, $y_{gap} = 3.5\%c$ and $Re = 1.7 \cdot 10^6$.
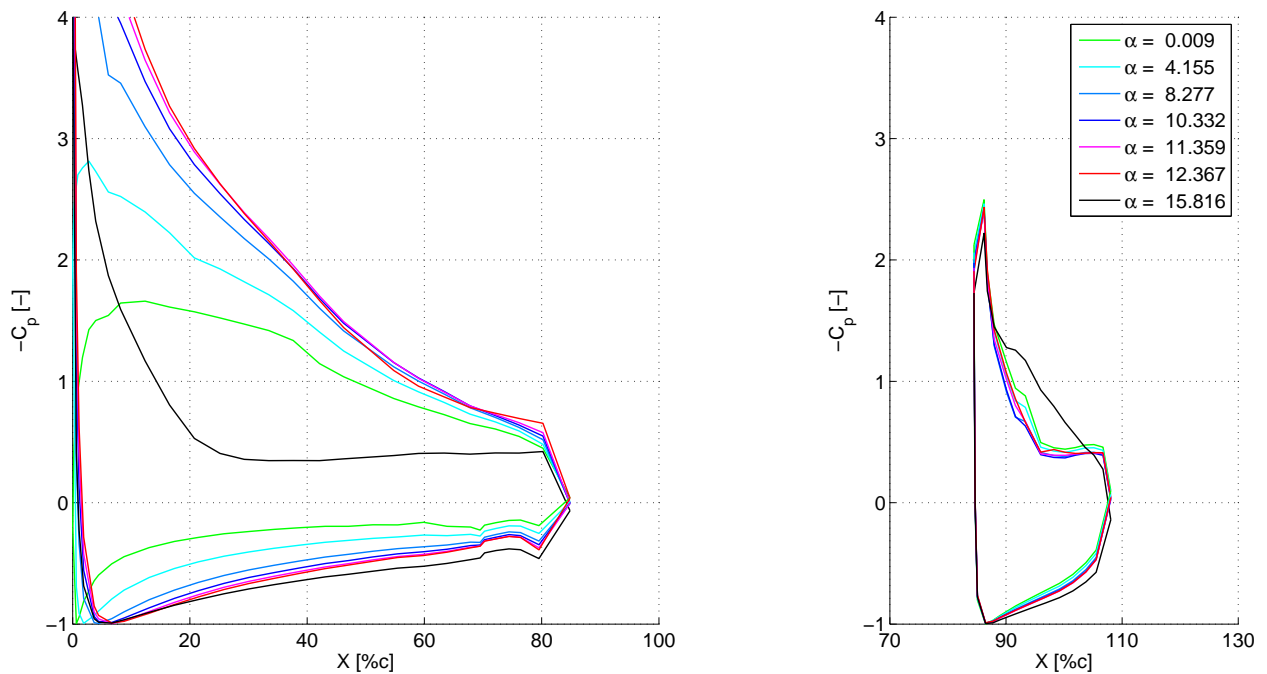
Figure B.4: C_p distribution of NLF-MOD22(B) with LER on flap: V shaped turbulators, for $\delta_f = 45°$, $x_{overlap} = 0\%c$, $y_{gap} = 3.5\%c$ and $Re = 1.7 \cdot 10^6$.

B.2   AC DBD plasma actuator
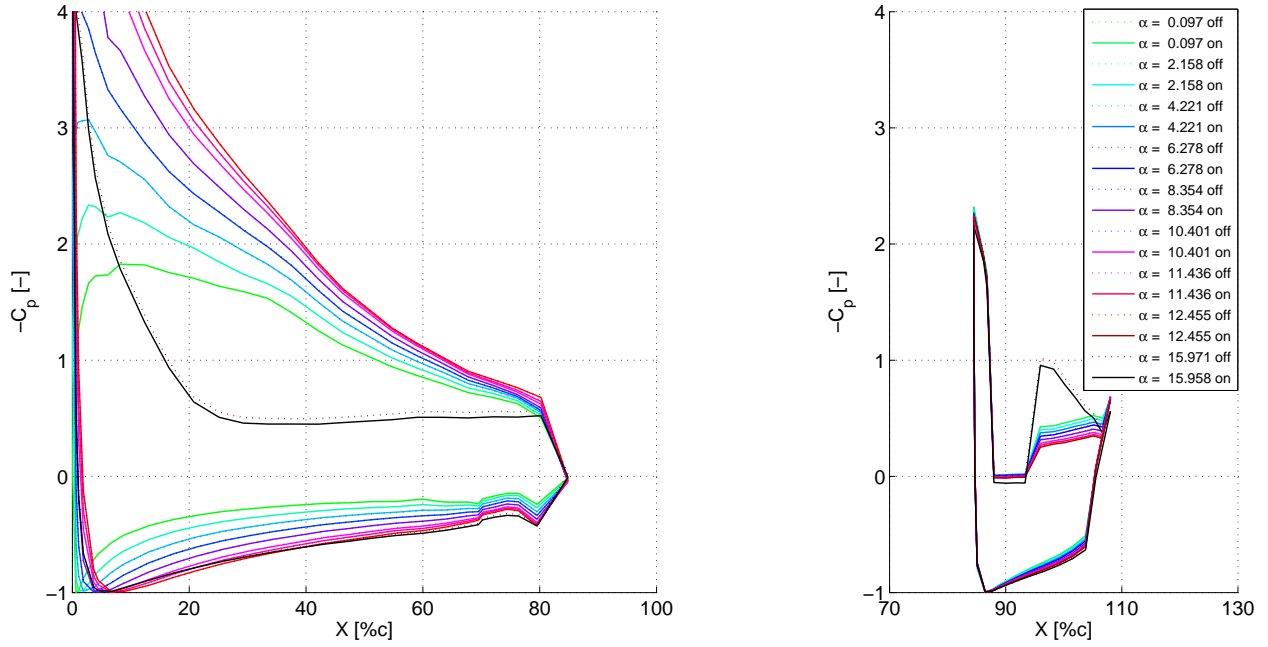
(a) Overview
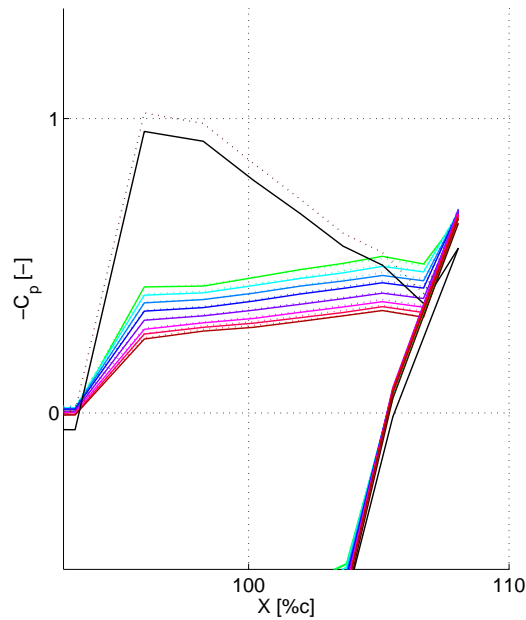
(b) Zoom

Figure B.5: Cp distribution of NLF-MOD22(B) with "case a" AC DBD plasma actuator on LE flap for $\delta_f = 45°$ and $Re = 1.7 \cdot 10^6$.
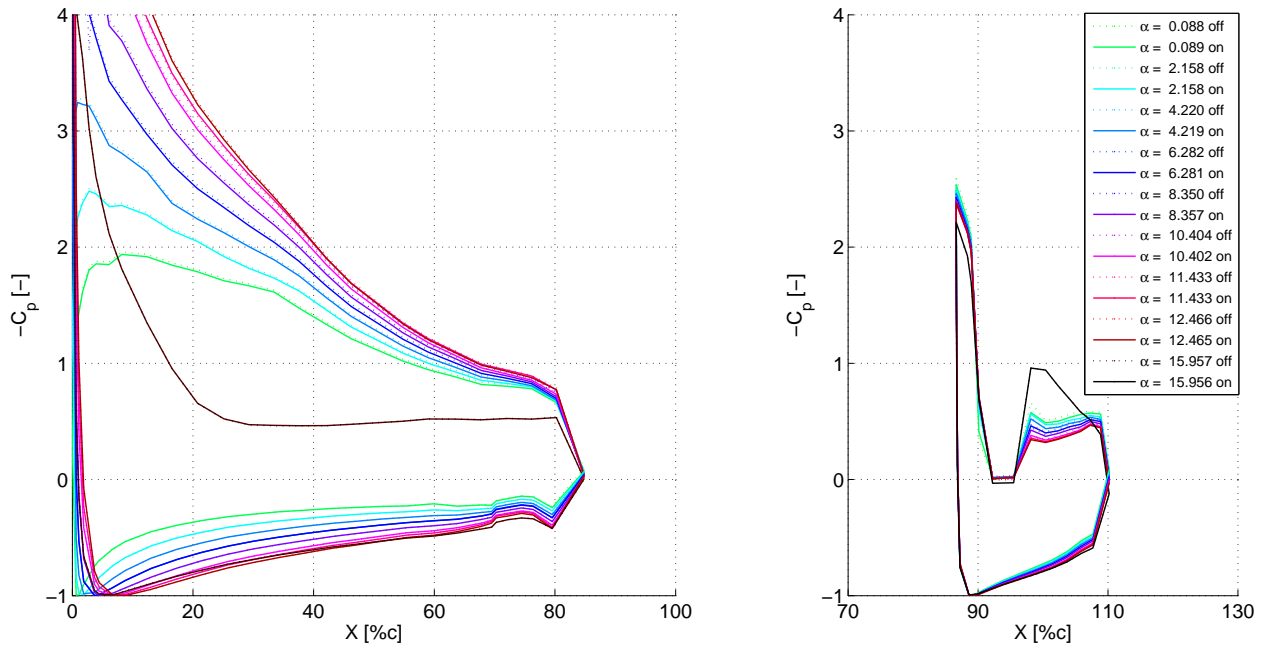
(a) Overview
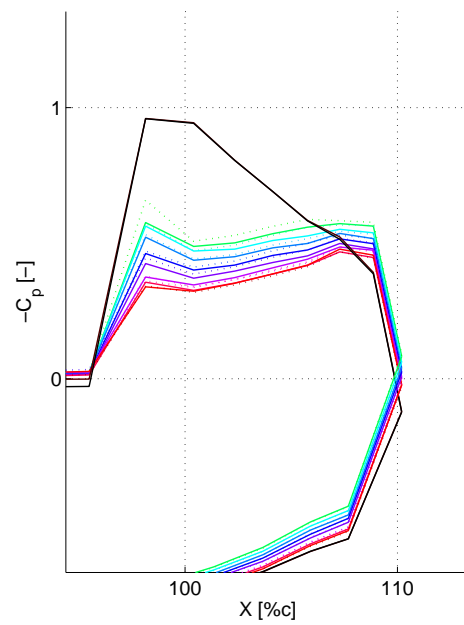
(b) Zoom

Figure B.6: Cp distribution of NLF-MOD22(B) with "case b" AC DBD plasma actuator on LE flap for $\delta_f = 45°$ and $Re = 1.7 \cdot 10^6$.

B.3   NS DBD plasma actuator
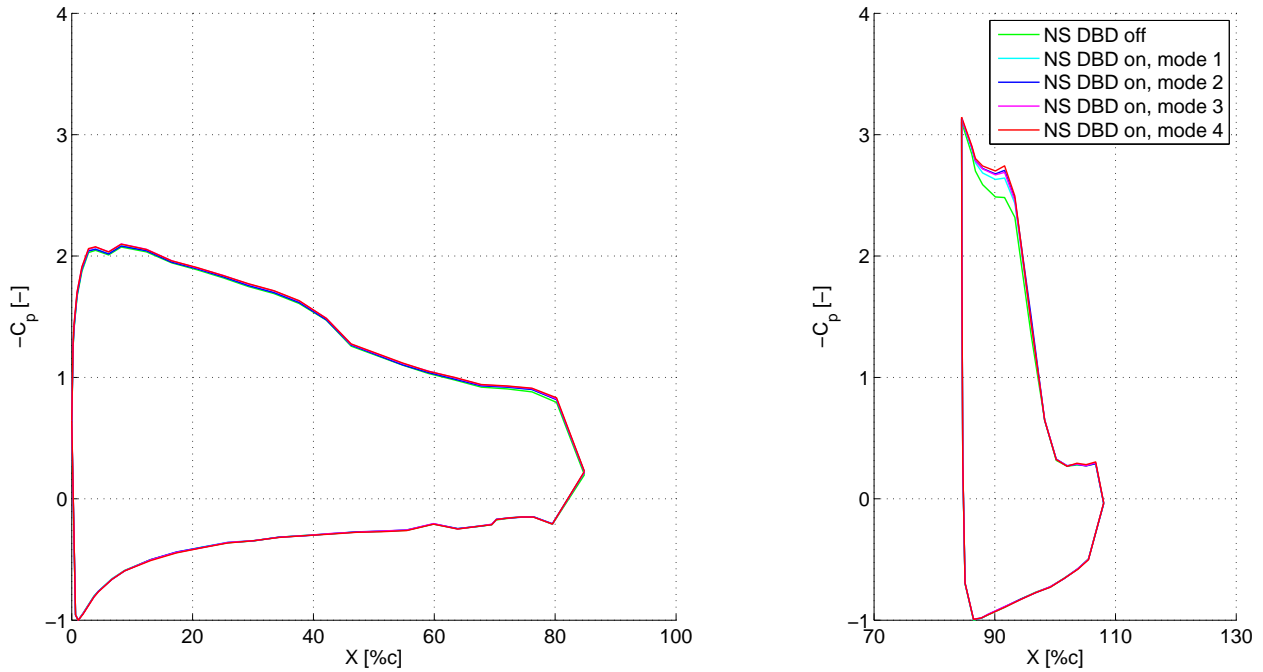
Figure B.7: Cp distribution of NLF-MOD22(B) with NS DBD plasma actuator on TE main wing for $\alpha = 0°$, $\delta_f = 45°$ and $Re = 0.85 \cdot 10^6$ ($V = 20m/s$).
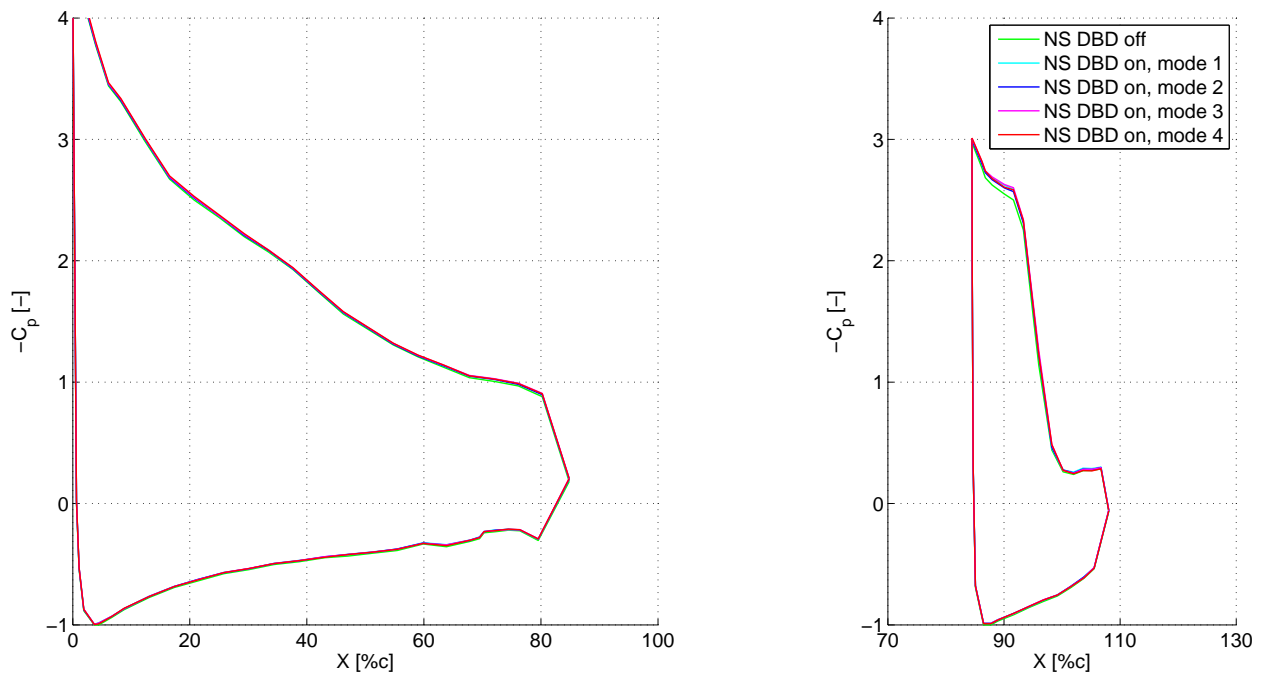
Figure B.8: Cp distribution of NLF-MOD22(B) with NS DBD plasma actuator on TE main wing for $\alpha = 5°$, $\delta_f = 45°$ and $Re = 0.85 \cdot 10^6$ ($V = 20m/s$).
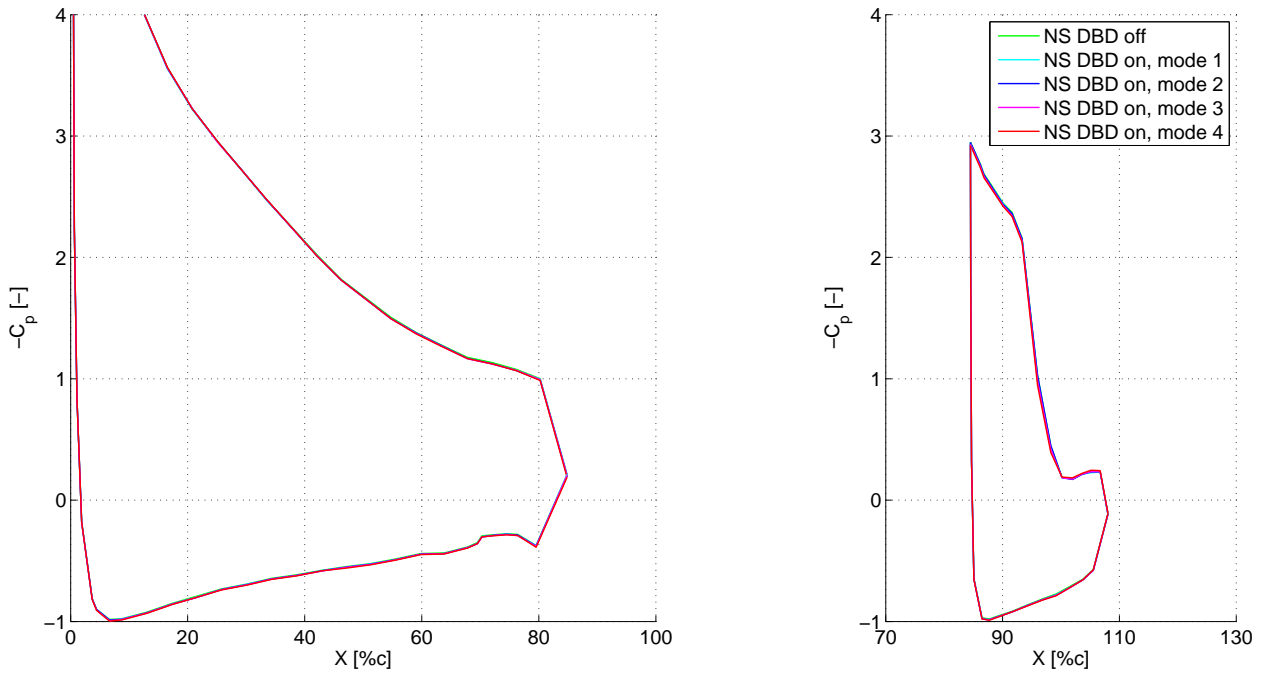
Figure B.9: Cp distribution of NLF-MOD22(B) with NS DBD plasma actuator on TE main wing for $\alpha = 10°$, $\delta_f = 45°$ and $Re = 0.85 \cdot 10^6$ ($V = 20m/s$).
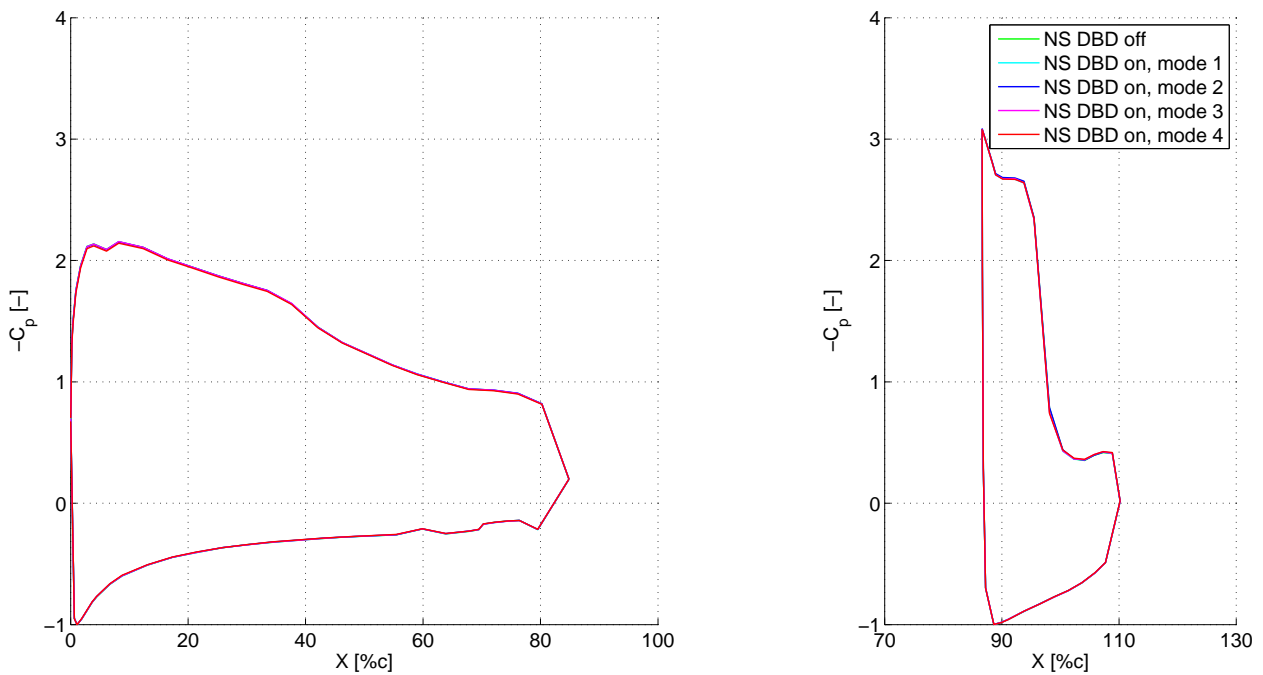
Figure B.10: Cp distribution of NLF-MOD22(B) with NS DBD plasma actuator on TE main wing for $\alpha = 0°$, $\delta_f = 45°$ and $Re = 1.27 \cdot 10^6$ ($V = 30m/s$).
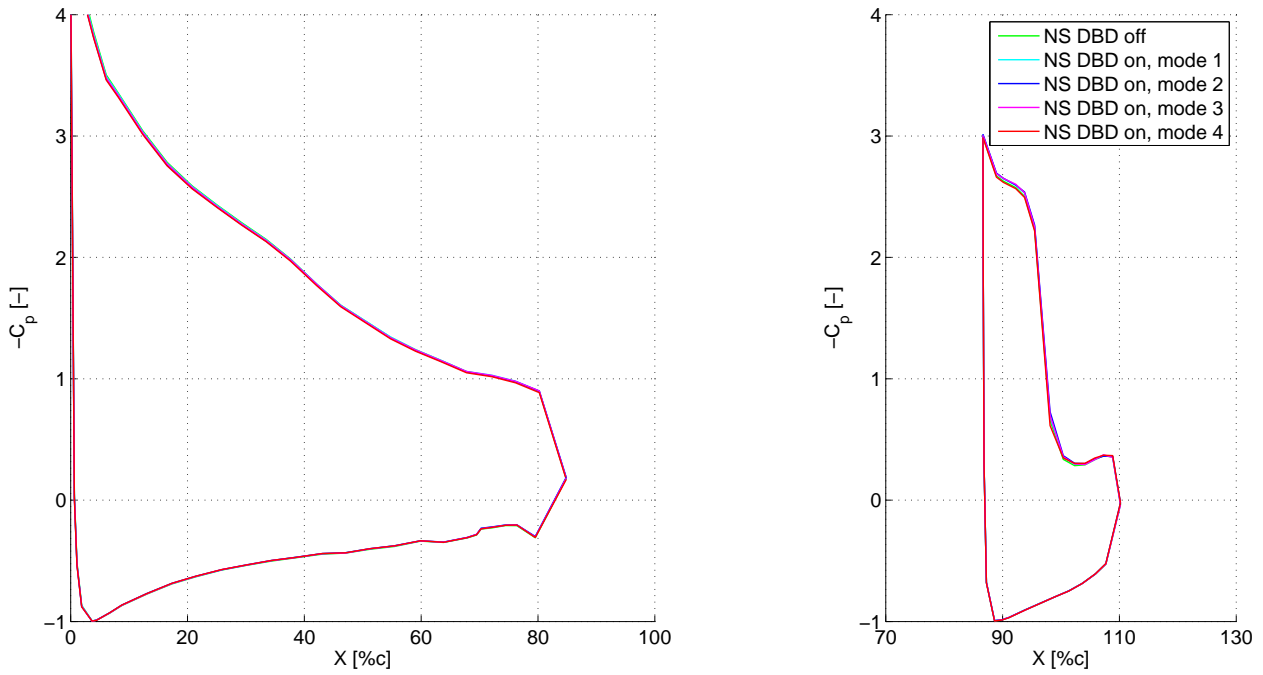
Figure B.11: Cp distribution of NLF-MOD22(B) with NS DBD plasma actuator on TE wing wing for $\alpha = 5°$, $\delta_f = 45°$ and $Re = 1.27 \cdot 10^6$ ($V = 30m/s$).
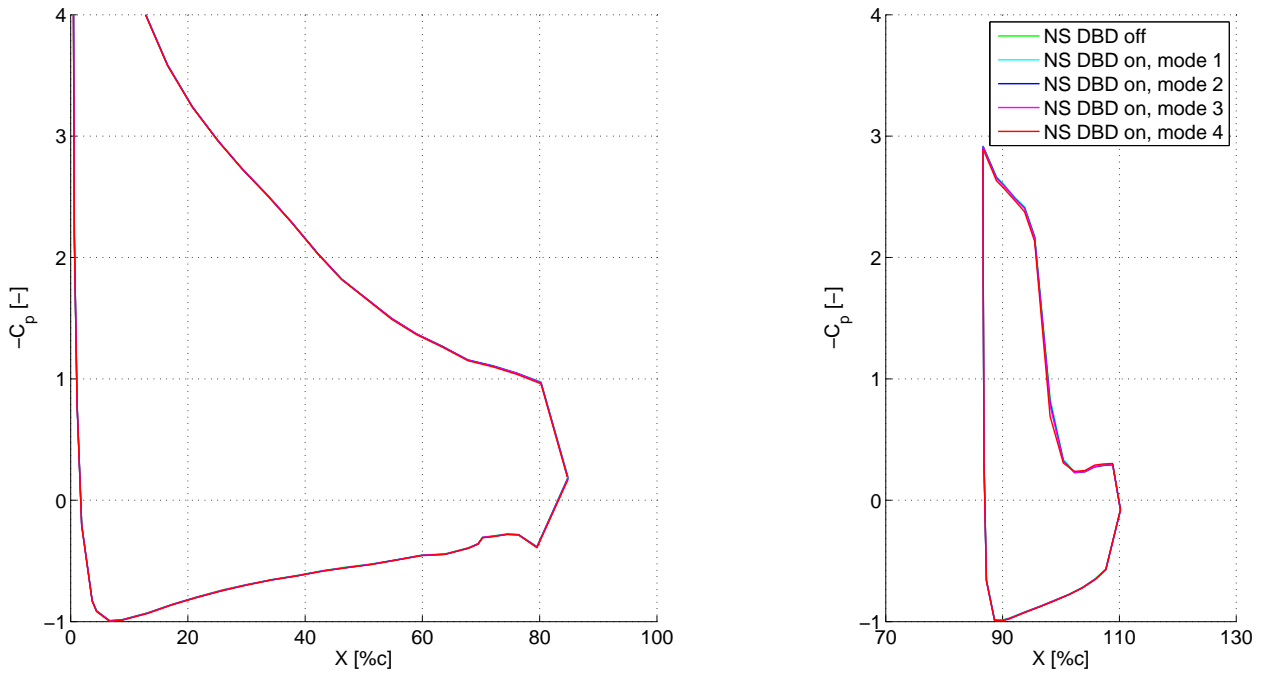
Figure B.12: Cp distribution of NLF-MOD22(B) with NS DBD plasma actuator on TE main wing for $\alpha = 10°$, $\delta_f = 45°$ and $Re = 1.27 \cdot 10^6$ ($V = 30m/s$).
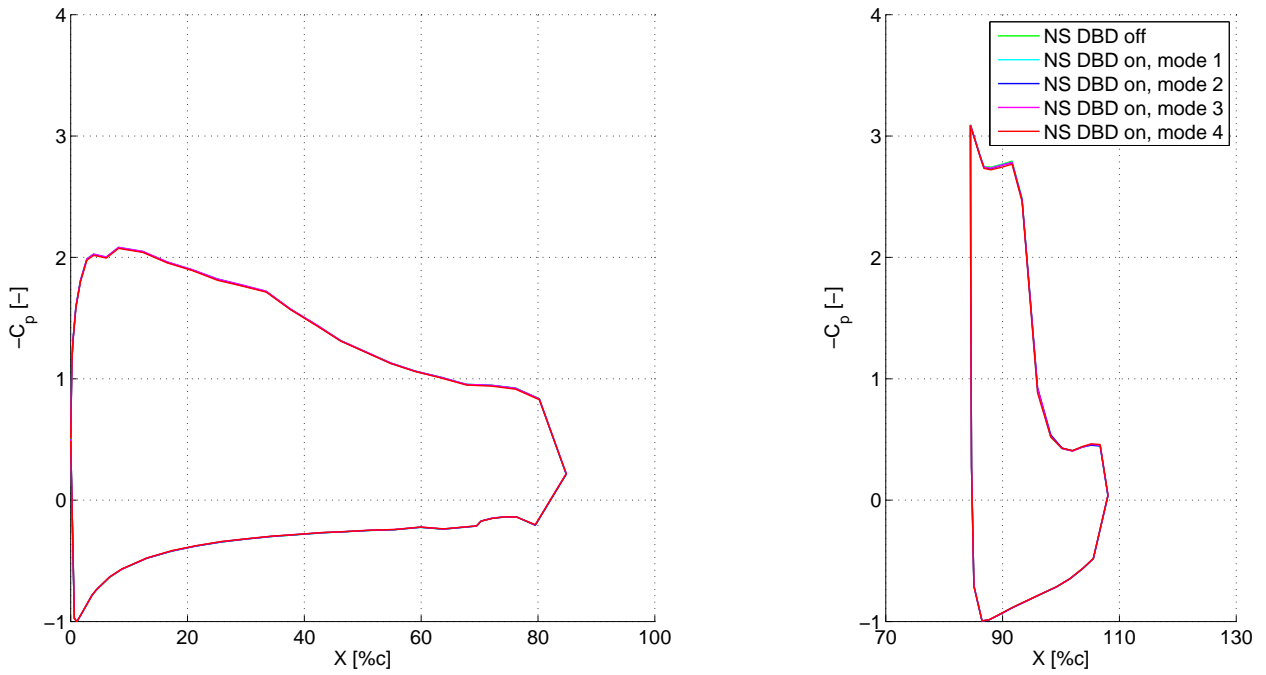
Figure B.13: Cp distribution of NLF-MOD22(B) with NS DBD plasma actuator on TE main wing for $\alpha = 0°$, $\delta_f = 45°$ and $Re = 1.7 \cdot 10^6$ ($V = 42m/s$).
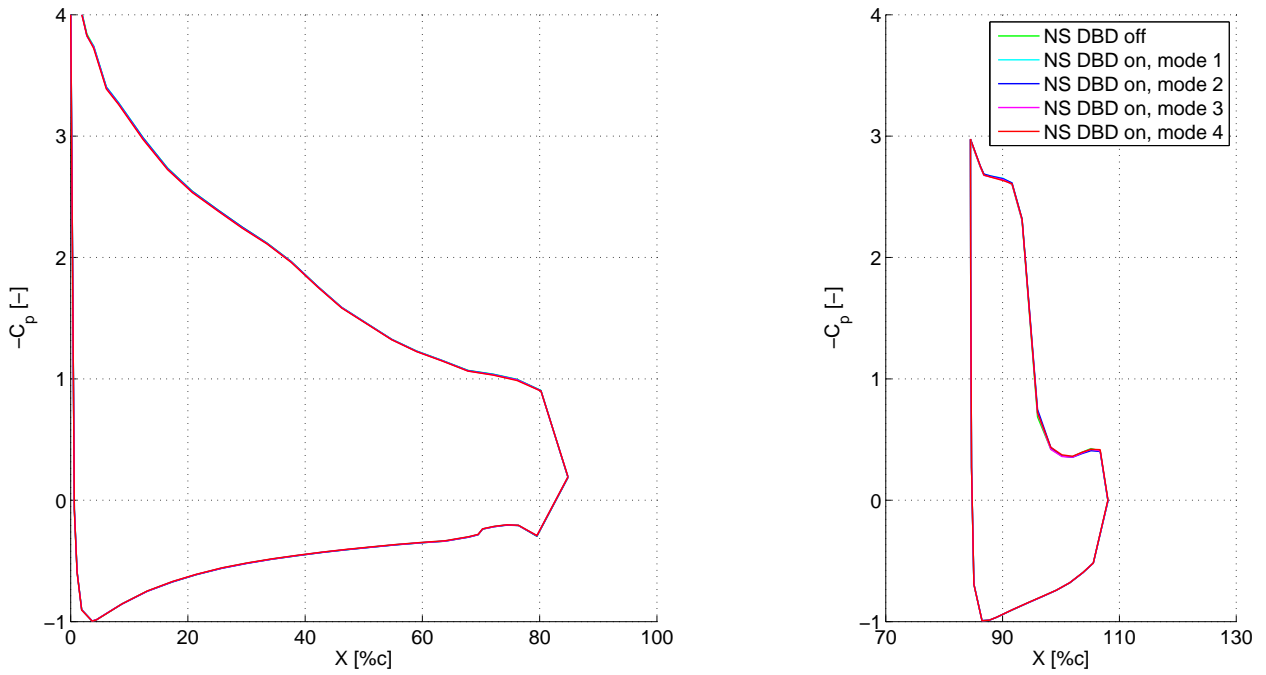
Figure B.14: Cp distribution of NLF-MOD22(B) with NS DBD plasma actuator on TE main wing for $\alpha = 5°$, $\delta_f = 45°$ and $Re = 1.7 \cdot 10^6$ ($V = 42m/s$).
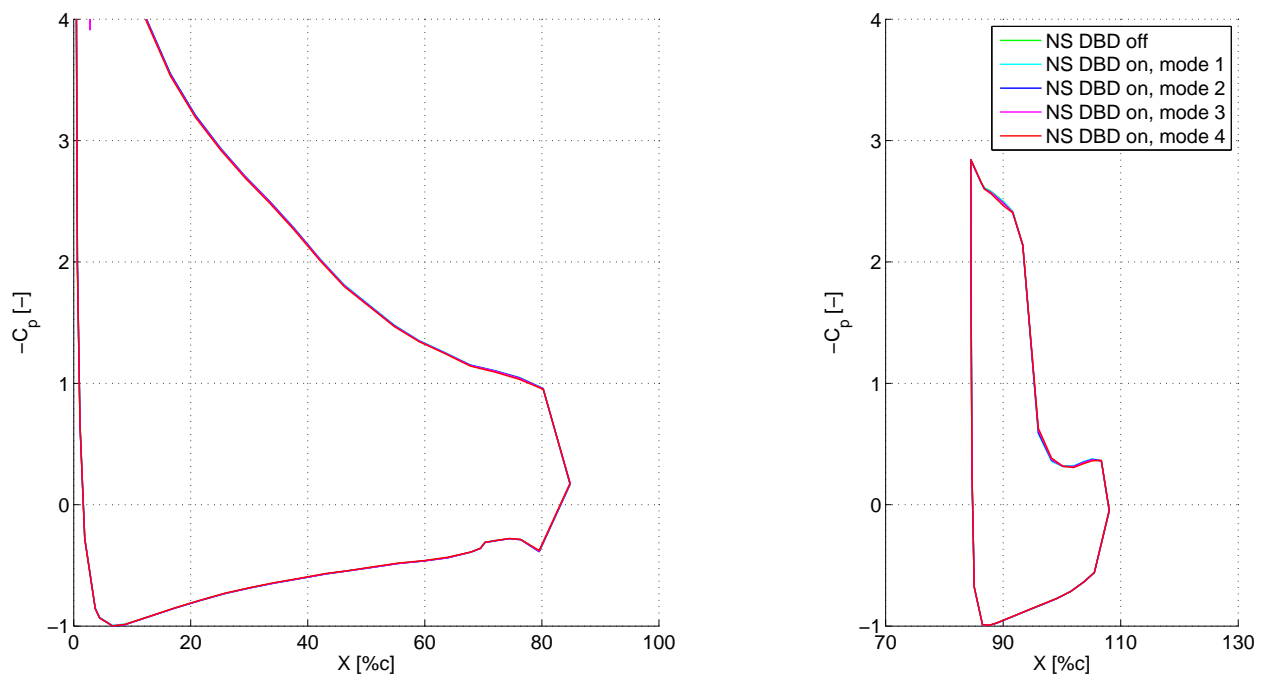
Figure B.15: Cp distribution of NLF-MOD22(B) with NS DBD plasma actuator on TE main wing for $\alpha = 10°$, $\delta_f = 45°$ and $Re = 1.7 \cdot 10^6$ ($V = 42m/s$).
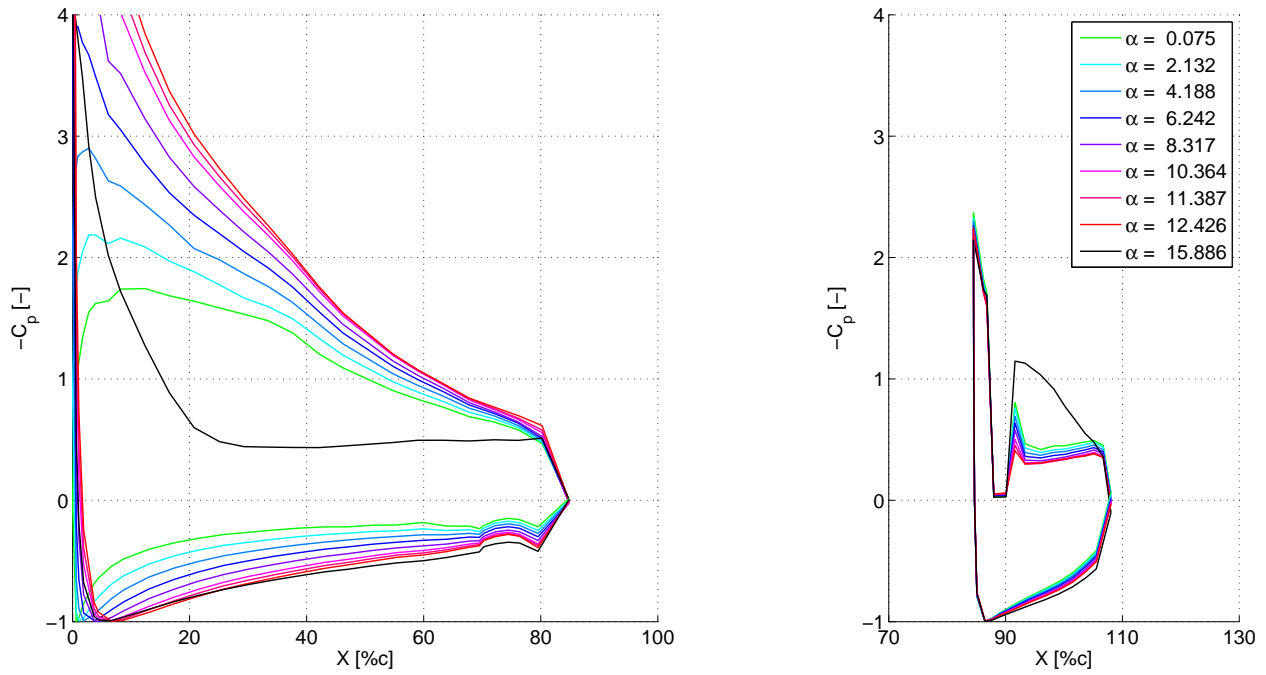
Figure B.16: Cp distribution of NLF-MOD22(B) with NS DBD plasma actuator ("mode 4") along flap's x_{tr} and *no* zigzag tape for $\delta_f = 45°$ and $Re = 1.7 \cdot 10^6$.
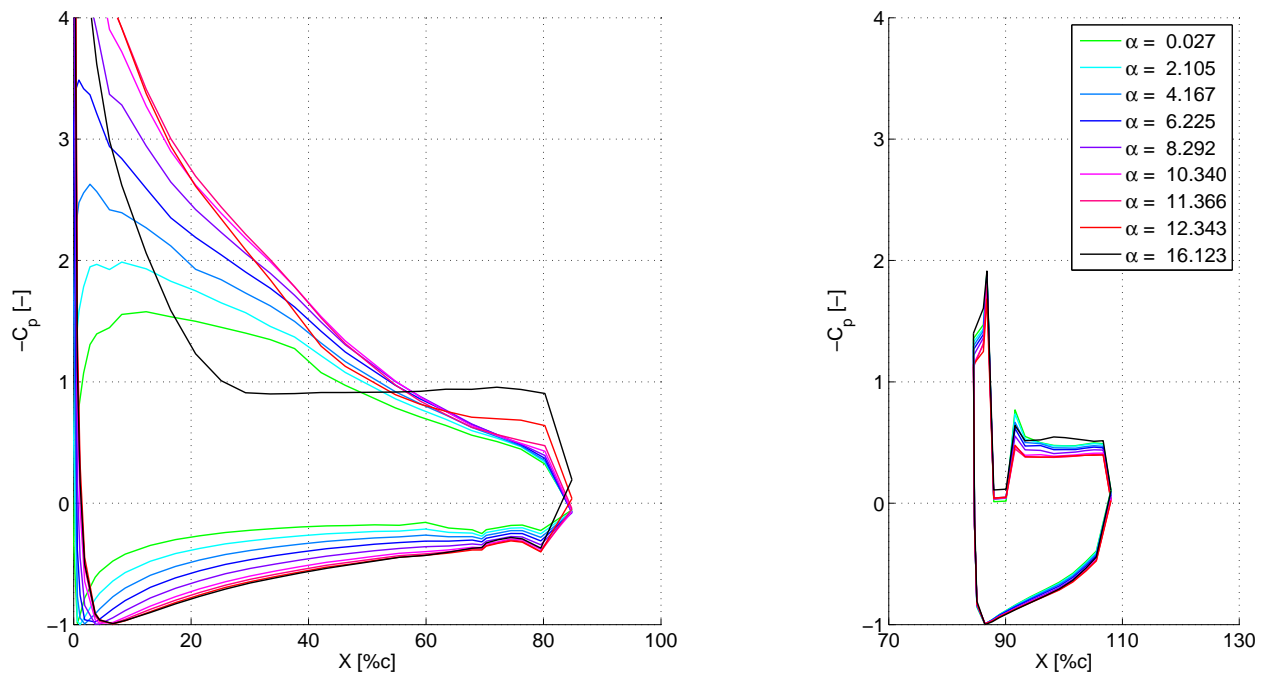
Figure B.17: Cp distribution of NLF-MOD22(B) with NS DBD plasma actuator ("mode 4") along flap's x_{tr} + zigzag tape on LE flap for $\delta_f = 45°$ and $Re = 1.7 \cdot 10^6$.

Appendix C

MSES additional information

C.1   Newton solution procedure

The Newton solution procedure is an important tool for simultaneous solving the nonlinear coupled system of the discrete inviscid Euler equations and the discrete boundary layer equations. The system of nonlinear equations to be solved can be written as,

$$F(Q) = 0 \tag{C.1}$$

where F is the vector of equations and Q the vector of variables. For some iteration level n, the Newton solution procedure can be described as

$$F(Q^{n+1}) \equiv F(Q^n + \delta Q^n) = F(Q^n) + \left[\frac{\partial F}{\partial Q}\right]^n \delta Q^n = 0 \tag{C.2}$$

$$\delta Q^n = -\frac{F(Q^n)}{\left[\frac{\partial F}{\partial Q}\right]^n} \tag{C.3}$$

In here $[\partial F/\partial Q]^n$ is the Jacobian matrix where entry (i,j) is the partial derivative of the i'th equation with respect to the j'th variable in Q. Vector F contains the system of discrete Euler equations, boundary layer equations, boundary conditions and global constraints. The quadratic convergence property of the Newton method is especially attractive for small increments in Q, which means that for a slightly parameter change the additional number of Newton iterations to reconverge the solution is minimal compared to the first convergence when starting from scratch.

C.2   Standard input format

This section discusses and shows the format of the two input files required to run MSES i.e. blade.xxx and mses.xxx. The blade.xxx file is used by the initialization program MSET and by the airfoil manipulating program AIRSET.

```
    NAME
     XINL    XOUT    YBOT    YTOP
     X(1,1)   Y(1,1)
     X(2,1)   Y(2,1)
     X(3,1)   Y(3,1)
        .        .
        .        .
        .        .
     X(I,1)   Y(I,1)
      999.     999.
     X(1,2)   Y(1,2)
     X(2,2)   Y(2,2)
     X(3,2)   Y(3,2)
        .        .
        .        .
        .        .
     X(I,2)   Y(I,2)
      999.     999.
     X(1,3)   Y(1,3)
     X(2,3)   Y(2,3)
     X(3,3)   Y(3,3)
        .        .
        .        .
        .        .
```

The blade.xxx file has the following structure:

where,

XINL is the X-location of the left grid inlet plane, in the same coordinate system as the airfoil coordinates.

XOUT is the X-location of the right grid outlet plane.

YBOT is the Y-location of the lowest grid streamline. It is also the location of the bottom wall in solid-wall cases.

YTOP is the Y-location of the topmost grid streamline. It is also the location of the top wall in solid-wall cases.

For a unit airfoil located between $(x, y) = (0, 0)$ and $(1, 0)$, the recommended minimum values for the four grid-boundary locations are:

```
    XINL   XOUT   YBOT   YTOP  :  -1.75  2.75  -2.0  2.5
```

X(1,1), Y(1,1) through to X(I,L), Y(I,L) are the coordinates of each airfoil element surface, starting at the trailing edge, going round the leading edge in either direction, then going back to the trailing edge. The individual elements are separated by a "999.0 999.0" line as indicated above and are ordered from top to bottom e.g. for a three element airfoil the sequence is slat, main element and flap.

The format of the mses.xxx file which serves as an input file for MSES and MSIS (not discussed in this work but also for MPOLAR and MPOLIS) is shown below. The meaning of the parameters can be found in the MSES User's Guide [9]. Parameters between brackets are optional.

```
GVAR(1)   GVAR(2)   ...              GVAR(N)
GCON(1)   GCON(2)   ...              GCON(N)
MACHIN    CLIFIN    ALFAIN
ISMOM     IFFBC     [DOUXIN   DOUYIN    SRCEIN]
REYIN     ACRIT     [KTRTYP]
XTRS1     XTRP1     XTRS2     XTRP2     XTRS3    XTRP3   ...
MCRIT     MUCON
[ISMOVE   ISPRES]
[NMODN    NPOSN]
[ISDELH   XCDELH    PTRHIN    ETAH]
```

C.3   Input file mses.nlfa

The input file for the MSES calculations performed in Section 6.3 - mses.nlfa - is shown here below. The format of the mses.xxx file can be found in Section C.2. For the exact meaning of the numbers used in the input file, one is referred to the MSES user's guide [9].

```
3         4         5         7
3         4         5         7
0.123     0.0       α
3         2
1.7E6     9.0
1.0       1.0       1.0       1.0
0.99      1.2
0         0
```

Appendix D

Airfoil coordinates of NLF-MOD22(A) and NLF-MOD22(B)

This appendix lists the coordinates of the NLF-MOD22(A) and the NLF-MOD22(B). The difference between both models can be found in the main element, flap coordinates for both models are similar. These coordinates are also used in the blade.xxx file for MSES and MSIS calculations, with the four grid-boundary locations defined as XINL XOUT YBOT YTOP: -2.0 3.5 -3.5 3.0.

NLF-MOD22(A) main		NLF-MOD22(B) main	
x	y	x	y
0.845000	0.038016	0.845000	0.038016
0.836550	0.038516	0.836550	0.038516
0.828101	0.039356	0.828101	0.039356
0.819650	0.040805	0.819650	0.040805
0.811200	0.042342	0.811200	0.042342
0.802750	0.043890	0.802750	0.043890
0.794301	0.045399	0.794301	0.045399
0.785849	0.046883	0.785849	0.046883
0.777400	0.048359	0.777400	0.048359
0.768950	0.049828	0.768950	0.049828
0.760500	0.051287	0.760500	0.051287
0.752050	0.052733	0.752050	0.052733
0.743601	0.054168	0.743601	0.054168
0.735149	0.055593	0.735149	0.055593
0.726700	0.057007	0.726700	0.057007
0.718251	0.058411	0.718251	0.058411
0.709801	0.059807	0.709801	0.059807
0.701350	0.061192	0.701350	0.061192
0.692900	0.062566	0.692900	0.062566

continued		continued	
x	y	x	y
0.684449	0.063931	0.684449	0.063931
0.676000	0.065286	0.676000	0.065286
0.667551	0.066632	0.667551	0.066632
0.659100	0.067967	0.659100	0.067967
0.650651	0.069290	0.650651	0.069290
0.642201	0.070602	0.642201	0.070602
0.633750	0.071904	0.633750	0.071904
0.625300	0.073195	0.625300	0.073195
0.616850	0.074473	0.616850	0.074473
0.608400	0.075741	0.608400	0.075741
0.599951	0.076996	0.599951	0.076996
0.591500	0.078239	0.591500	0.078239
0.583050	0.079468	0.583050	0.079468
0.574600	0.080684	0.574600	0.080684
0.566150	0.081886	0.566150	0.081886
0.557701	0.083072	0.557701	0.083072
0.549250	0.084243	0.549250	0.084243
0.540800	0.085398	0.540800	0.085398
0.532350	0.086536	0.532350	0.086536
0.523899	0.087656	0.523899	0.087656
0.515451	0.088759	0.515451	0.088759
0.507001	0.089842	0.507001	0.089842
0.498551	0.090907	0.498551	0.090907
0.490101	0.091950	0.490101	0.091950
0.481651	0.092971	0.481651	0.092971
0.473200	0.093971	0.473200	0.093971
0.464750	0.094945	0.464750	0.094945
0.456301	0.095892	0.456301	0.095892
0.447851	0.096811	0.447851	0.096811
0.439401	0.097699	0.439401	0.097699
0.430950	0.098554	0.430950	0.098554
0.422501	0.099372	0.422501	0.099372
0.414050	0.100149	0.414050	0.100149
0.405600	0.100879	0.405600	0.100879
0.397150	0.101559	0.397150	0.101559
0.388700	0.102182	0.388700	0.102182
0.380251	0.102744	0.380251	0.102744
0.371800	0.103243	0.371800	0.103243
0.363351	0.103674	0.363351	0.103674
0.354901	0.104030	0.354901	0.104030
0.346450	0.104308	0.346450	0.104308
0.338001	0.104507	0.338001	0.104507
0.329551	0.104625	0.329551	0.104625
0.321100	0.104663	0.321100	0.104663
0.312650	0.104624	0.312650	0.104624

x	y	x	y
0.304200	0.104507	0.304200	0.104507
0.295751	0.104314	0.295751	0.104314
0.287302	0.104045	0.287302	0.104045
0.278851	0.103699	0.278851	0.103699
0.270400	0.103276	0.270400	0.103276
0.261951	0.102774	0.261951	0.102774
0.253500	0.102192	0.253500	0.102192
0.245051	0.101528	0.245051	0.101528
0.236601	0.100781	0.236601	0.100781
0.228151	0.099949	0.228151	0.099949
0.219700	0.099028	0.219700	0.099028
0.211252	0.098017	0.211252	0.098017
0.202800	0.096912	0.202800	0.096912
0.194351	0.095711	0.194351	0.095711
0.185900	0.094408	0.185900	0.094408
0.177450	0.093000	0.177450	0.093000
0.169000	0.091481	0.169000	0.091481
0.160551	0.089846	0.160551	0.089846
0.152102	0.088088	0.152102	0.088088
0.143650	0.086198	0.143650	0.086198
0.135200	0.084171	0.135200	0.084171
0.126750	0.081995	0.126750	0.081995
0.118300	0.079662	0.118300	0.079662
0.109851	0.077161	0.109851	0.077161
0.101400	0.074476	0.101400	0.074476
0.092950	0.071587	0.092950	0.071587
0.084501	0.068470	0.084501	0.068470
0.076051	0.065099	0.076051	0.065099
0.067601	0.061441	0.067601	0.061441
0.059151	0.057457	0.059151	0.057457
0.050701	0.053090	0.050701	0.053090
0.042250	0.048257	0.042250	0.048257
0.041413	0.047749	0.041413	0.047749
0.040568	0.047230	0.040568	0.047230
0.039723	0.046706	0.039723	0.046706
0.038878	0.046174	0.038878	0.046174
0.038033	0.045636	0.038033	0.045636
0.037188	0.045092	0.037188	0.045092
0.036343	0.044540	0.036343	0.044540
0.035498	0.043982	0.035498	0.043982
0.034653	0.043416	0.034653	0.043416
0.033808	0.042843	0.033808	0.042843
0.032963	0.042262	0.032963	0.042262
0.032118	0.041672	0.032118	0.041672
0.031273	0.041075	0.031273	0.041075

	continued		continued
x	y	x	y
0.030428	0.040470	0.030428	0.040470
0.029583	0.039854	0.029583	0.039854
0.028738	0.039230	0.028738	0.039230
0.027893	0.038596	0.027893	0.038596
0.027048	0.037952	0.027048	0.037952
0.026203	0.037299	0.026203	0.037299
0.025358	0.036634	0.025358	0.036634
0.024513	0.035959	0.024513	0.035959
0.023668	0.035272	0.023668	0.035272
0.022823	0.034571	0.022823	0.034571
0.021978	0.033860	0.021978	0.033860
0.021133	0.033135	0.021133	0.033135
0.020288	0.032396	0.020288	0.032396
0.019443	0.031642	0.019443	0.031642
0.018598	0.030871	0.018598	0.030871
0.017753	0.030085	0.017753	0.030085
0.016908	0.029280	0.016908	0.029280
0.016063	0.028457	0.016063	0.028457
0.015218	0.027613	0.015218	0.027613
0.014373	0.026748	0.014373	0.026748
0.013528	0.025858	0.013528	0.025858
0.012683	0.024944	0.012683	0.024944
0.011838	0.024001	0.011838	0.024001
0.010993	0.023027	0.010993	0.023027
0.010148	0.022022	0.010148	0.022022
0.009300	0.020981	0.009300	0.020981
0.008460	0.019899	0.008460	0.019899
0.007610	0.018770	0.007610	0.018770
0.006770	0.017589	0.006770	0.017589
0.005920	0.016344	0.005920	0.016344
0.005080	0.015031	0.005080	0.015031
0.004230	0.013626	0.004230	0.013626
0.003390	0.012100	0.003390	0.012100
0.002540	0.010411	0.002540	0.010411
0.001700	0.008470	0.001700	0.008470
0.000853	0.006070	0.000853	0.006070
0.000008	0.001470	0.000008	0.001470
0.000845	-0.004050	0.000845	-0.004050
0.001690	-0.005770	0.001690	-0.005770
0.002540	-0.007040	0.002540	-0.007040
0.003380	-0.008090	0.003380	-0.008090
0.004230	-0.009010	0.004230	-0.009010
0.005070	-0.009850	0.005070	-0.009850
0.005920	-0.010639	0.005920	-0.010639
0.006760	-0.011378	0.006760	-0.011378

	continued			continued	
x	y	x	y
0.007610	-0.012078	0.007610	-0.012078
0.008450	-0.012749	0.008450	-0.012749
0.009300	-0.013390	0.009300	-0.013390
0.010140	-0.014003	0.010140	-0.014003
0.010985	-0.014588	0.010985	-0.014588
0.011829	-0.015146	0.011829	-0.015146
0.012676	-0.015677	0.012676	-0.015677
0.013520	-0.016182	0.013520	-0.016182
0.014365	-0.016664	0.014365	-0.016664
0.015211	-0.017125	0.015211	-0.017125
0.016056	-0.017567	0.016056	-0.017567
0.016900	-0.017991	0.016900	-0.017991
0.017746	-0.018400	0.017746	-0.018400
0.018590	-0.018794	0.018590	-0.018794
0.019435	-0.019177	0.019435	-0.019177
0.020280	-0.019548	0.020280	-0.019548
0.021125	-0.019908	0.021125	-0.019908
0.021969	-0.020258	0.021969	-0.020258
0.022814	-0.020599	0.022814	-0.020599
0.023660	-0.020933	0.023660	-0.020933
0.024506	-0.021259	0.024506	-0.021259
0.025351	-0.021579	0.025351	-0.021579
0.026195	-0.021892	0.026195	-0.021892
0.027040	-0.022201	0.027040	-0.022201
0.027885	-0.022504	0.027885	-0.022504
0.028731	-0.022804	0.028731	-0.022804
0.029576	-0.023098	0.029576	-0.023098
0.030421	-0.023389	0.030421	-0.023389
0.031266	-0.023674	0.031266	-0.023674
0.032110	-0.023956	0.032110	-0.023956
0.032956	-0.024234	0.032956	-0.024234
0.033801	-0.024508	0.033801	-0.024508
0.034646	-0.024776	0.034646	-0.024776
0.035490	-0.025042	0.035490	-0.025042
0.036334	-0.025303	0.036334	-0.025303
0.037179	-0.025560	0.037179	-0.025560
0.038025	-0.025814	0.038025	-0.025814
0.038870	-0.026064	0.038870	-0.026064
0.039714	-0.026310	0.039714	-0.026310
0.040560	-0.026553	0.040560	-0.026553
0.041404	-0.026792	0.041404	-0.026792
0.042251	-0.027028	0.042251	-0.027028
0.050700	-0.029226	0.050700	-0.029226
0.059150	-0.031190	0.059150	-0.031190
0.067600	-0.032974	0.067600	-0.032974

	continued		continued
x	y	x	y
0.076050	-0.034614	0.076050	-0.034614
0.084499	-0.036136	0.084499	-0.036136
0.092950	-0.037561	0.092950	-0.037561
0.101400	-0.038903	0.101400	-0.038903
0.109850	-0.040175	0.109850	-0.040175
0.118300	-0.041386	0.118300	-0.041386
0.126750	-0.042540	0.126750	-0.042540
0.135200	-0.043641	0.135200	-0.043641
0.143650	-0.044694	0.143650	-0.044694
0.152099	-0.045702	0.152099	-0.045702
0.160550	-0.046663	0.160550	-0.046663
0.168999	-0.047579	0.168999	-0.047579
0.177451	-0.048455	0.177451	-0.048455
0.185900	-0.049302	0.185900	-0.049302
0.194350	-0.050127	0.194350	-0.050127
0.202800	-0.050929	0.202800	-0.050929
0.211250	-0.051703	0.211250	-0.051703
0.219700	-0.052447	0.219700	-0.052447
0.228151	-0.053161	0.228151	-0.053161
0.236600	-0.053845	0.236600	-0.053845
0.245050	-0.054501	0.245050	-0.054501
0.253500	-0.055130	0.253500	-0.055130
0.261950	-0.055735	0.261950	-0.055735
0.270400	-0.056313	0.270400	-0.056313
0.278850	-0.056869	0.278850	-0.056869
0.287300	-0.057404	0.287300	-0.057404
0.295750	-0.057919	0.295750	-0.057919
0.304200	-0.058411	0.304200	-0.058411
0.312651	-0.058884	0.312651	-0.058884
0.321099	-0.059334	0.321099	-0.059334
0.329550	-0.059762	0.329550	-0.059762
0.337999	-0.060165	0.337999	-0.060165
0.346451	-0.060543	0.346451	-0.060543
0.354900	-0.060896	0.354900	-0.060896
0.363350	-0.061223	0.363350	-0.061223
0.371800	-0.061525	0.371800	-0.061525
0.380250	-0.061804	0.380250	-0.061804
0.388700	-0.062057	0.388700	-0.062057
0.397149	-0.062286	0.397149	-0.062286
0.405600	-0.062490	0.405600	-0.062490
0.414050	-0.062671	0.414050	-0.062671
0.422500	-0.062828	0.422500	-0.062828
0.430950	-0.062962	0.430950	-0.062962
0.439401	-0.063071	0.439401	-0.063071
0.447850	-0.063156	0.447850	-0.063156
0.456300	-0.063217	0.456300	-0.063217

	continued			continued	
x	y	x	y
0.464749	-0.063252	0.464749	-0.063252
0.473199	-0.063263	0.473199	-0.063263
0.481650	-0.063247	0.481650	-0.063247
0.490100	-0.063203	0.490100	-0.063203
0.498549	-0.063132	0.498549	-0.063132
0.506999	-0.063031	0.506999	-0.063031
0.515450	-0.062900	0.515450	-0.062900
0.523900	-0.062735	0.523900	-0.062735
0.532350	-0.062536	0.532350	-0.062536
0.540799	-0.062298	0.540799	-0.062298
0.549250	-0.062022	0.549250	-0.062022
0.557700	-0.061703	0.557700	-0.061703
0.566150	-0.061332	0.566150	-0.061332
0.574599	-0.060902	0.574599	-0.060902
0.583049	-0.060416	0.583049	-0.060416
0.591499	-0.059882	0.591499	-0.059882
0.599949	-0.059292	0.599949	-0.059292
0.608400	-0.058614	0.608400	-0.058614
0.616849	-0.057849	0.616849	-0.057849
0.625300	-0.057077	0.625300	-0.057077
0.633749	-0.056337	0.633749	-0.056337
0.642200	-0.055335	0.642200	-0.055335
0.650650	-0.053654	0.698000	-0.047500
0.659100	-0.050846	0.691000	-0.029000
0.667550	-0.046267	0.692900	-0.022922
0.675999	-0.039743	0.701349	-0.010801
0.684450	-0.031813	0.709799	0.000634
0.692900	-0.022922	0.718249	0.008900
0.701349	-0.010801	0.726699	0.015458
0.709799	0.000634	0.735150	0.020828
0.718249	0.008900	0.743599	0.025212
0.726699	0.015458	0.752050	0.028749
0.735150	0.020828	0.760499	0.031547
0.743599	0.025212	0.768949	0.033754
0.752050	0.028749	0.777400	0.035466
0.760499	0.031547	0.785849	0.036741
0.768949	0.033754	0.794300	0.037619
0.777400	0.035466	0.802748	0.038133
0.785849	0.036741	0.811199	0.038335
0.794300	0.037619	0.819649	0.038269
0.802748	0.038133	0.828099	0.037968
0.811199	0.038335	0.836549	0.037455
0.819649	0.038269	0.845000	0.036732
0.828099	0.037968		
0.836549	0.037455		
0.845000	0.036732		

NLF-MOD22(A) & NLF-MOD22(B) flap

x	y
1.000000	0.000277
0.996573	0.001276
0.992556	0.002469
0.987893	0.003910
0.982527	0.005618
0.976529	0.007504
0.970047	0.009448
0.963191	0.011391
0.956041	0.013294
0.948623	0.015151
0.940973	0.016969
0.933122	0.018752
0.925113	0.020508
0.917020	0.022233
0.908928	0.023914
0.900916	0.025532
0.893092	0.027055
0.885493	0.028426
0.877970	0.029642
0.870511	0.030739
0.863159	0.031687
0.855874	0.032486
0.848641	0.033134
0.841462	0.033635
0.834345	0.033985
0.827310	0.034186
0.820389	0.034233
0.813610	0.034123
0.806999	0.033847
0.800561	0.033397
0.794292	0.032766
0.788180	0.031949
0.782219	0.030950
0.776422	0.029773
0.770800	0.028422
0.765365	0.026901
0.760132	0.025215
0.755108	0.023357
0.750276	0.021315
0.745619	0.019092
0.741137	0.016700
0.736842	0.014157
0.732748	0.011479
0.728874	0.008703
0.725253	0.005870
0.721912	0.003015

	continued
x	y
0.718864	0.000170
0.716111	-0.002620
0.713657	-0.005318
0.711493	-0.007894
0.709604	-0.010335
0.707970	-0.012638
0.706567	-0.014807
0.705371	-0.016850
0.704366	-0.018778
0.703534	-0.020605
0.702865	-0.022343
0.702353	-0.024002
0.701988	-0.025591
0.701763	-0.027112
0.701669	-0.028568
0.701700	-0.029956
0.701851	-0.031292
0.702123	-0.032602
0.702507	-0.033886
0.703001	-0.035132
0.703596	-0.036332
0.704331	-0.037451
0.705204	-0.038476
0.706196	-0.039402
0.707290	-0.040231
0.708503	-0.040903
0.709864	-0.041335
0.711300	-0.041733
0.712860	-0.041921
0.714556	-0.041894
0.716410	-0.041716
0.718462	-0.041416
0.720765	-0.041003
0.723390	-0.040470
0.726424	-0.039803
0.729977	-0.038976
0.734177	-0.037954
0.739157	-0.036704
0.745007	-0.035202
0.751716	-0.033460
0.759130	-0.031541
0.767018	-0.029512
0.775156	-0.027446
0.783387	-0.025401
0.791606	-0.023410
0.799715	-0.021503

	continued	
x	y
0.807667	-0.019692
0.815512	-0.017965
0.823306	-0.016311
0.831112	-0.014718
0.838995	-0.013175
0.846956	-0.011687
0.854981	-0.010259
0.863015	-0.008906
0.871011	-0.007635
0.878971	-0.006449
0.886911	-0.005346
0.894844	-0.004325
0.902770	-0.003390
0.910689	-0.002542
0.918581	-0.001787
0.926431	-0.001128
0.934212	-0.000571
0.941887	-0.000119
0.949421	0.000221
0.956755	0.000446
0.963827	0.000549
0.970555	0.000527
0.976857	0.000378
0.982636	0.000103
0.987827	-0.000274
0.992430	-0.000700
0.996482	-0.001139
1.000000	-0.001550